Department of Physics and Astronomy

University of Heidelberg

Master thesis

in Physics

submitted by

Timo Pascal Steinsberger

born in Esslingen am Neckar, Germany

2018

Microwave injection for the ALPHATRAP experiment and developments of the multi-reflection time-of-flight technique of the ISOLTRAP experiment

This Master thesis has been carried out by Timo Pascal Steinsberger

at the

Max Planck Institute for Nuclear Physics (MPIK)

and the

Conseil Européen pour la Recherche Nucléaire (CERN)

under the supervision of

Prof. Dr. rer. nat. Klaus Blaum

Dr. Vladimir Manea

and

Dr. Sven Sturm

Abstract

This thesis presents work done at the ALPHATRAP g-factor experiment at the MPIK in Heidelberg and at the mass spectrometry experiment ISOLTRAP at ISOLDE/CERN. At ALPHATRAP a system for microwave transmission from the room temperature environment to the cryogenic trap tower was designed. Microwave horns were used for contact free power transfer in a first step to a 77 K temperature shield and in a second step to the trap tower cooled to 4.2 K. Additional devices for the alignment of a laser beam with the microwaves and a mode filter were designed. At ISOLTRAP, studies for multi-reflection time-of-flight mass measurements (MR-ToF MS) were performed. A distortion of the peaks in the time-of-flight spectrum due to the radiofrequency field in the RFQ used for beam preparation was investigated and reduced. In order to improve the ion optics, a new Einzel lens was designed and a new quadrupole bender was commissioned. The stability of mass measurements using the ISOLTRAP MR-ToF MS with ions from an off-line reference ion source were investigated. For measurements with a total recording time of more than one minute, a systematic error on the order of 100 keV was determined. It was reduced for shorter measurement cycles, where the uncertainty due to low statistics dominates.

Zusammenfassung

Diese Arbeit beschreibt Beiträge zum ALPHATRAP g-Faktor Experiment am MPIK in Heidelberg und für das Massenspektroskopie-Experiment ISOLTRAP an ISOLDE/CERN. Für ALPHATRAP wurde ein System zum Transport von Mikrowellen von der Raumtemperaturumgebung zum kryogenen Fallenturm entwickelt. Mikrowellenhörner werden genutzt, um die Leistung kontaktfrei in einem ersten Schritt zu einem 77 K-Temperaturschild und in einem zweiten Schritt zum 4.2 K kalten Fallenturm zu transportieren. Zusätzlich wurden Bauteile zur koaxialen Ausrichtung eines Laserstrahls mit dem Mikrowellensignal, sowie ein Modenfilter für transmittierte Mikrowellen konstruiert. An ISOLTRAP wurden Studien zu multi-reflection time-of-flight Massenmessungen (MR-ToF MS) durchgeführt. Eine Verzerrung der Linienform in Flugzeitspektren, ausgelöst durch das Radiofrequenzfeld der zur Strahlpräparation genutzten linearen Paulfalle, wurde untersucht und reduziert. Für eine Verbesserung der Ionenoptik wurden eine neue Einzellinse konstruiert und ein Quadrupolumlenker in Betrieb genommen. Die Stabilität von Massenmessungen mit dem ISOLTRAP MR-ToF MS wurde für Fälle untersucht, in denen nur Referenzionen von einer Off-Line Ionenquelle zur Verfügung stehen. Für Messungen mit einer Messdauer von mehr als einer Minute wurde ein systematischer Fehler von 100 keV gemessen. Dieser minimiert sich für Messungen mit kürzerer Dauer, für welche dann die statistischen Unsicherheiten dominieren.

Contents

0.1 List of Figures

0.2 List of Tables

1 Introduction

Physics describes the nature and behaviour of matter in the universe on all scales. On cosmic scales, the theory of General Relativity is used to describe the nature of space and time and to explain gravity. On microscopic scales, quantum field theories are used to describe the fundamental interactions of particles and their substructure. The experimentally well established quantum field theories form the so called Standard Model of Particle Physics (SM). It contains all known kinds of matter particles, denoted as fermions, and three interactions transmitted field quanta called bosons. In addition, the Higgs Boson explains the existence of the mass of the other particles. The Standard Model is presented in Fig. 1.1. The 12 fermions are organised

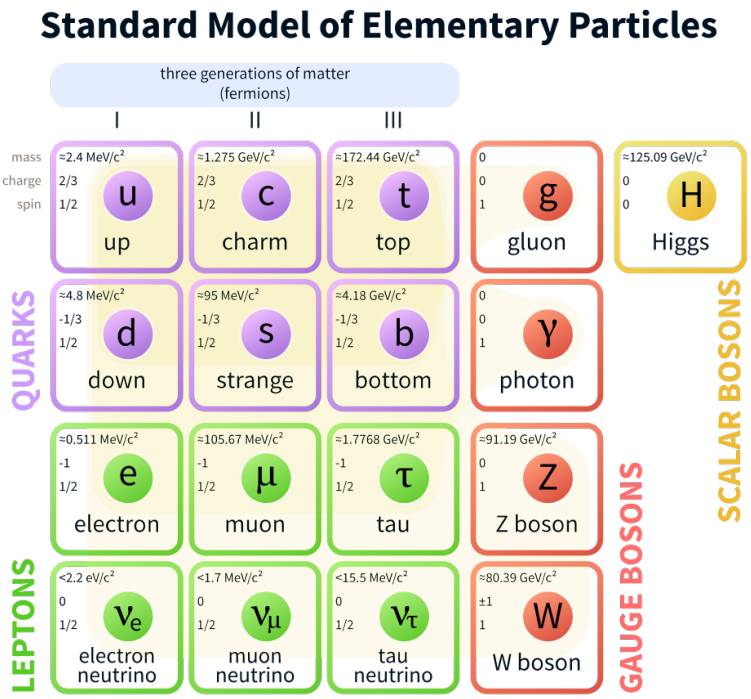

Figure 1.1: The Standard Model of Particle Physics (taken from [1]).

in two families with three generations each:
Quarks appear only in bound states, the only stable ones are protons (2 up-quarks and 1 down-quark). Also neutrons (2 down-quarks and 1 up-quark) are stable, when they are combined together with protons to form the nuclei of atoms and ions.
There are two kind of leptons, the electrically charged leptons and three corresponding neutrinos. The only stable charged lepton is the electron. The three neutrinos are electrically neutral and very light. Only upper limits of their masses are known.
Three fundamental interactions between these particles are described with quantum field theories. Fundamental forces are transmitted by so called gauge bosons.

1. The strong force describes the interaction between quarks and nucleons in the nuclei of atoms and ions. The corresponding bosons are called gluons. It is the strongest of the four fundamental forces, but its range is restricted to a few femtometers. It is described by a theory called Quantum Chromodynamics (QCD) [2]. Due to the strength and manifold of QCD interactions, theoretical calculations are complicated and strongly rely on experimental constraints.
2. The weak force describes the radioactive decay of nuclei.
3. The electromagnetic force describes all magnetic and electric interactions between charged particles, including the binding of electrons in the shells of an atom. It is described by a theory called Quantum Electrodynamics (QED), which can be unified with the weak force to the electroweak theory.

The Standard Model of Particle Physics has proven to be very successful, being tested with high precision, but it is not able to predict phenomena like dark matter, the masses of the neutrinos or the expansion of the universe. On the search to find physics beyond the standard model, there are two main strategies: Particle accelerators like the Large Hadron Collider (LHC) at CERN work on the energy frontier, trying to observe new particles at high energies. The second strategy works on the precision frontier, trying to find small deviations from Standard Model predictions in low energy observables, for example ground state properties of atoms and ions. Thanks to storage times in principle only limited by the lifetime of the investigated system and efficient manipulation techniques, Penning traps became a well established tool for measurements with charged particles [3].

One observable is the magnetic moment of the bound electron in highly charged ions. It is predicted by QED and calculated using perturbation theory in powers of $(Z\alpha)$ with the nuclear charge number Z and the fine-structure constant $\alpha \approx 1/137$ to highest precision [4]. Due to the strong electric fields inside highly charged ions, higher-order interaction prediceted by QED can be tested under extreme conditions. Until now, the magnetic moment of the electron was measured in highly charged ions up to $^{40}Ca^{17+}$ [5]. As a scaled up successor of an experiment at the University of Mainz [6], the ALPHATRAP experiment will enlarge the range of available ions up to hydrogen-like $^{208}Pb^{81+}$ with $Z\alpha \approx 1$ and therefore allow stringent tests of the theory. The magnetic moment is measured inside a cryogenic Penning trap, where the electron g-factor is deduced from the ratio of Larmor and cyclotron frequency. To do so, the resonant interaction of the electron magnetic moment with a microwave at the Larmor frequency is detected. In chapter 3 of this work, the design of a transmission system for the microwave signal from room temperature to the cryogenic trap without metallic connection of the different temperature sections is described.

Another observable are nuclear binding energies and therefore nuclear masses. They are measured for radioactive nuclei at the ISOLTRAP experiment (see chapter 4) at CERN in Geneva, Switzerland, using Penning-trap techniques as well as with time-of-flight mass spectrometry. Measured masses of exotic nuclei constrain nuclear structure calculations based on QCD under extreme conditions [7, 8] and are also used as input parameters for the simulation in nuclear astrophysics [9, 10]. Differences of nuclear masses involved in β-decays are needed for tests of the electroweak theory [11]. The required relative precision for these fields is on the order of $10^{-7} - 10^{-8}$[12].

To improve the precision of the ISOLTRAP experiment, an uncertainty in mass measurement

with a Multi-Reflection Time-of-Flight Mass Spectrometer/Separator (MR-ToF MS) due to the ion preparation in a linear RFQ trap was investigated in chapter 5. The efficiency of the ion transport was tackled in the chapters 6 and 8, uncertainties due to beam preparation and stability of measurements using a Multi-Reflection Time-of-Flight Mass Spectrometer/Separator were investigated. In chapter 7, the stability of the MR-ToF mass measurements is investigated for cases, when no isobaric contaminant is available as reference.

2 Storage of charged particles and ion transport

In order to resolve both observables, the magnetic and moment of elementary particles and nuclei with high precision, well-defined state of the considered particles are required. This can be reached with ion traps, which allow cooling and manipulation and characterization of ions. In this chapter three kinds of ion traps are presented, Paul traps, Penning traps and Multi-Reflection Time-of-Flight Mass Spectrometer, as well as einzel lenses for efficient ion transport and electromagnetic waveguides for the transport of microwaves used for the manipulation of ions.

2.1 Paul traps

2.1.1 Working principle

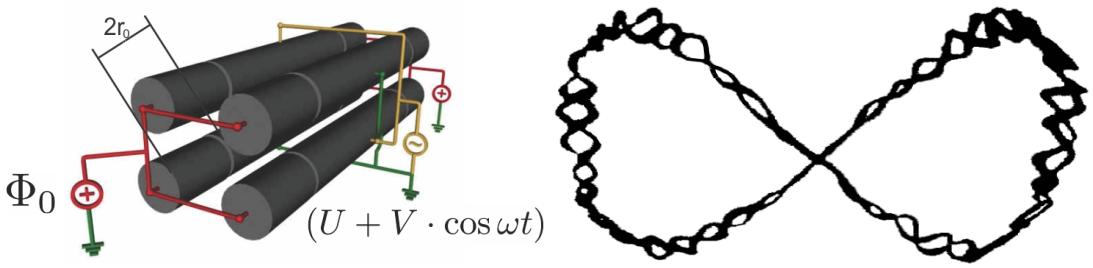

(a) Linear Paul trap (b) Ion motion in a Paul trap

Figure 2.1: (a) Structure of a linear Paul trap taken from [13]. (b) Lissajous trajectory of an ion stored in a Paul trap (taken from [14], colors inverted),

Due to the Laplace equation of electrostatics

$$\Delta\Phi = 0, \tag{2.1}$$

electric potentials cannot have a minimum in three dimensions, in which ions can be confined. In the so called Paul or radio frequency quadrupole (RFQ) traps, the ions are trapped in one dimension with an axis-symmetric electrostatic quadrupole field and radially with an oscillating RF field. Paul traps exist in a variety of shapes. In the following, the equation of motions for a linear Paul trap as depicted in Fig. 2.1a are discussed. A similar discussion is found in [15]. The linear Paul trap consists of four segmented rods with an inner distance of $2r_0$. A static DC voltage Φ_0 is applied to all rods in the outer segments and create potential minimum along the longitudinal x-axis, in which ions are stored in this dimension. Following the Laplace equation (2.1), this creates a potential close to the minimum of the form

$$\Phi_l(x, y, z, t) = \frac{\Phi_0}{2x_0^2} \cdot (2x^2 - y^2 - z^2). \tag{2.2}$$

with x_0 being a typical length. Radial confinement can be achieved with an oscillating quadrupole field. In addition the already mentioned potential, a sum of a DC potential U and an RF voltage V with frequency $\omega = 2\pi\nu_{RF}$ is applied as $\pm(U + V \cdot \cos\omega t)$ with same sign for opposite rods is applied (see Fig. 2.1a). They add a transversal potential given by

$$\Phi_t(x, y, z, t) = (U + V \cdot \cos\omega t) \cdot \frac{y^2 - z^2}{r_0^2}. \tag{2.3}$$

Therefore, the overall potential Φ is given by

$$\Phi(x, y, z, t) = \Phi_l(x, y, z, t) + \Phi_t(x, y, z, t) \tag{2.4}$$

$$= \frac{\Phi_0}{2x_0^2} \cdot (2x^2 - y^2 - z^2) + (U + V \cdot \cos\omega t) \cdot \frac{y^2 - z^2}{r_0^2}. \tag{2.5}$$

In the longitudinal x-dimension, the ions perform a harmonic oscillation. In the transversal directions, the equation of motion are given by

$$\ddot{y} - \frac{Q\Phi_0}{mx_0^2} \cdot y + \frac{2Q}{mr_0^2} \cdot (U + V\cos\omega t) \cdot y = 0, \tag{2.6}$$

$$\ddot{z} - \frac{Q\Phi_0}{mx_0^2} \cdot z - \frac{2Q}{mr_0^2} \cdot (U + V\cos\omega t) \cdot z = 0. \tag{2.7}$$

$$\tag{2.8}$$

Here, Q and m denote the ion charge and mass [16]. With the dimensionless parameters a, q and ξ defined as

$$\xi = \omega t/2, \tag{2.9}$$

$$a_{y,z} = \pm\frac{8QU}{mr_0^2\omega^2} - \frac{4Q\Phi_0}{mx_0^2}, \tag{2.10}$$

$$q_{y,z} = \mp\frac{4QV}{mr_0^2\omega^2}, \tag{2.11}$$

$$\tag{2.12}$$

this can be written as the Mathieu equation [17]

$$\frac{\partial^2 u}{\partial\xi^2} + (a_u - 2q_u \cdot \cos 2\xi) \cdot y = 0. \tag{2.13}$$

with $u = x, y$. Depending on the parameters a_u and q_u, solutions are stable or diverge. While the latter case corresponds to an ion loss. For successful ion storage, the solution has to be stable in y and z. Solving the Mathieu equations (2.6) and (2.7) simultaneously reveals stable regions for the parameters a and u. This is shown for the linear Paul Trap in 2.2a. For quadrupole mass filters, no longitudinal trapping voltage is applied: $\Phi_0 = 0$. Then the transversal stability diagram reduces to the one displayed in 2.2b. Since a and q are both mass dependent, the ion storage is mass selective.

As discussed in [19] even for the case of small pertubations of Eq. eq:Mathieu, stable solutions in $u = \{y, z\}$ are given by a superposition of oscillations with the frequencies

$$\omega_{n,u} = |2n + \beta_u|, \quad n = 0, \pm1, \pm2, .. \tag{2.14}$$

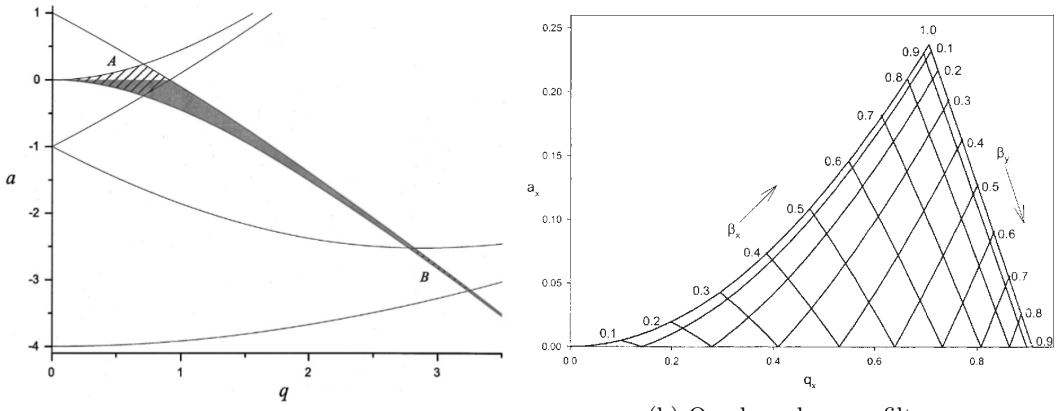

(a) Linear Paul trap

(b) Quadrupole mass filter

Figure 2.2: Stability regions (a) of a linear Paul trap with $U = 0$ (taken from [15]). The stable region (grey) includes the two stable regions A and B of the quadrupole mass filter. (b) Zoom on region A for a quadrupole mass filter (taken from [18]).

with the parameter

$$\beta_u^2 = a_u + \frac{q_u^2}{(2+\beta_u)^2 - a_u - \frac{q_u^2}{(4+\beta_u)^2 - a_u - \frac{q_u^2}{(6+\beta_u)^2 - a_u - \ldots}}} + \frac{q_u^2}{(2-\beta_u)^2 - a_u - \frac{q_u^2}{(4-\beta_u)^2 - a_u - \frac{q_u^2}{(6-\beta_u)^2 - a_u - \ldots}}} \tag{2.15}$$

$$\approx \left[a - \frac{(a-1)q^2}{2(a-1)^2 - q^2} - \frac{(5a+7)q^4}{32(a-1)^3(a-4)} - \frac{(9a^2+58a+29)q^6}{64(a-1)^5(a-4)(a-9)} \right]^{1/2} \tag{2.16}$$

[20] Equations with $\beta_u \in \mathbb{N}$ are called Mathieu equation and form the border of stability. The amplitudes of these oscillations decrease quickly [19]. For $|a_u| \ll 1$ and $q_u < 0.4$, β is well appoximated by $\beta_u^2 = a_u + q_u^2/2$ as demonstrated experimentally in [14]. In this case the motion reduces to a slow macro-motion with the frequency

$$\omega_{macro} = \frac{\beta_u}{2}\omega. \tag{2.17}$$

and a micro-motion with the frequency of the radiofrequency (RF) field ω. A trajectory of a particle in Paul trap is depicted in Fig. 2.1b The macro-motion can be used to define a radial pseudopotential

$$\Phi_{pseudo}(u) = \frac{m\omega_{macro,u}^2}{2Q} \cdot u^2 = \left(\frac{QV^2}{mr_0^2\omega^2} \pm \frac{U}{2} \right) \cdot \frac{u^2}{r_0^2} \tag{2.18}$$

with $u \in \{y, z\}$ and the sign depending on the polarity of the DC voltage U applied to the rods. Two criteria for successful storage in RF only mode ($U = 0$) can be derived:
The overall effective potential

$$\Phi_{eff}(x,,y,z) = \Phi_l + \Phi_{pseudo} = \frac{\Phi_0}{2x_0^2} \cdot (2x^2 - y^2 - z^2) + \frac{QV^2}{mr_0^4\omega^2} \cdot (x^2 + y^2) \tag{2.19}$$

must have a minimum in the centre of the trap at $(x = y = z = 0)$ and therefore

$$V_{min} = r_0^2 \omega \sqrt{\frac{m\Phi_0}{2Qx_0^2}}. \tag{2.20}$$

This corresponds to a minimal q:

$$q_{min} = \sqrt{\frac{8Q\phi_0}{m\omega^2 x_0^2}}. \tag{2.21}$$

For higher RF amplitudes V, $q \gg a$ (see equations (2.10) and (2.11)) and regions close to the q axis in the stability diagram 2.2b have to be considered. Here an upper cut-off of the stability region is given at $q_{max} = 0.908$. This yields

$$V_{max} \approx \frac{mr_0^2\omega^2}{4Q} \cdot q_{max}. \tag{2.22}$$

2.1.2 RFQs used as ion cooler and buncher

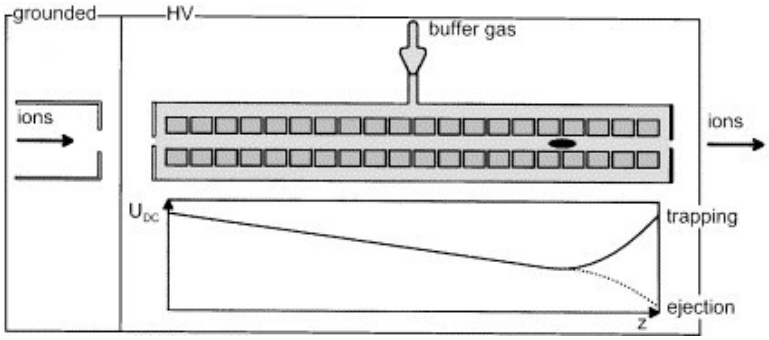

Figure 2.3: Schematic design of and electric potential in an RFQ buncher and cooler at as used at ISOLTRAP (taken from [21]). The axial potential is displayed for ion trapping and ejection.

Linear Paul traps as depicted in Fig. 2.3 are used as devices to cool and bunch ion beams. The trap rods are segmented to create an axial potential with a minimum close to the exit. For extraction, the last segments are switched down and release an ion bunch. The trap is filled with a noble gas much lighter than the mass of the stored ion species. Therefore, mainly helium is used. The arriving ion beam is slowed down to a kinetic energy of a few eV. This can be realized by placing the RFQ inside a high voltage cage. At these low kinetic energies, the ions mainly interact with the gas atoms via dipole interactions. They experience the averaged force $\vec{F}$

$$\vec{F} = -\delta \cdot m \cdot \vec{v} \tag{2.23}$$

where m and $\vec{v}$ are the ion mass and velocity and δ the damping constant

$$\delta = \frac{Q}{m} \frac{p/p_N}{M_{ion} T/T_N}. \tag{2.24}$$

Here, Q is the ion charge and M_{ion} denotes the reduced mobility of the ion/buffer gas pair, p/p_N and T/T_N the pressure and temperature in units of the normal pressure or temperature, respectively [22]. The ion motion is damped in axial and transversal direction as depicted in

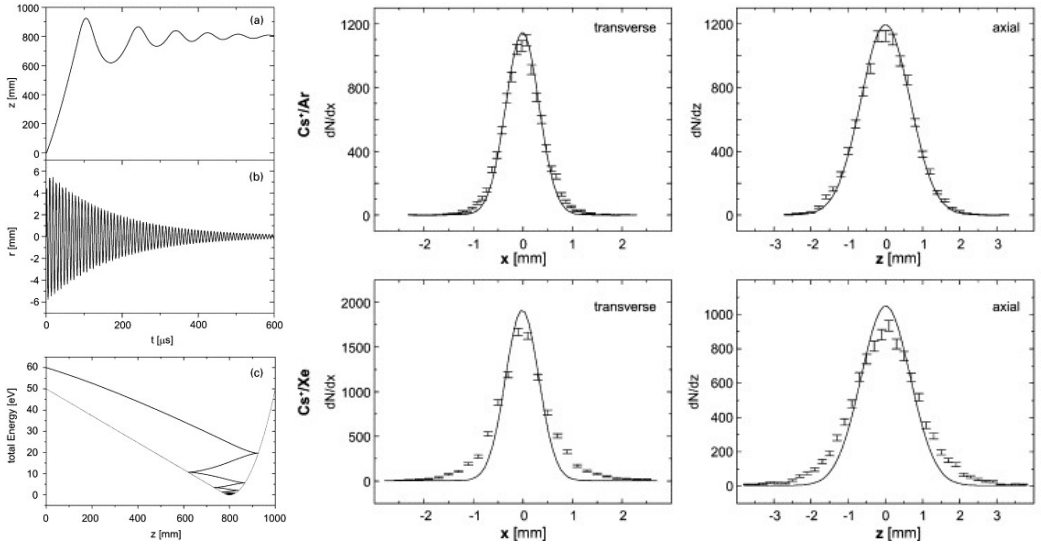

(a) Damping of ion motion

(b) Thermalized ion distribution

Figure 2.4: (a) Simulated damping of the ion motion in an RFQ cooler buncher and cooler due to interaction with the buffer gas simulated with a damping force as in equation (2.23) from top to bottom: axial position depending on time, radial position depending on time, energy depending on position. (b) spatial spread of thermalized $^{133}Cs^{+}$ cloud in an RFQ filled with argon (top) and xenon (bottom). The points are simulated taking with a Monte Carlo simulation taking into account realistic scattering potentials. The solid line represents a perfectly thermalized distribution at a temperature of 300 K. Both pictures were taken from [21].

Fig. 2.4a until an equilibrium with the driving electric field and with the buffer gas temperature is reached. The damping has to be that strong, that the injected ion cannot leave the trap. If the buffer gas is light enough, the ions thermalize perfectly, as was shown in Monte Carlo simulations of the interactions with the buffer gas using realistic scattering potentials as was done by Stephan Schwartz [22]. The resulting ion distribtution is displayed in Fig. 2.4b. If the gas is too massive, collisions lead to a phase jump of the ion motion with respect to the radiofrequency field and consequently to an increase in energy. This process is call RF heating [21]. RFQs can be used to bunch continuous ion beams. The number of trapped ions is controlled by the time ions are accumulated in the buncher. This time is called beam gate. Then, the ions are stored until they are cooled. During this time, the segmented rods form an axial potential as shown in Fig. 2.4. The ions are accumulated in the minimum of the potential and the extracted by switching the last RFQ segments to create a potential ramp and the ions are extracted as a bunch.

2.2 Penning traps

In Penning traps, ion storage is achieved by a superposition of an electric quadrupole field (axial confinement) and a strong magnetic field (radial confinement). They are used for high precision experiments with non-destructive (stable nuclei, ALPHATRAP) and destructive (short lived nuclei, ISOLTRAP) detection methods. In a Penning trap, the ions are confined radially by an electric quadrupole-field, which can be created either by hyperbolic electrodes (hyperbolic

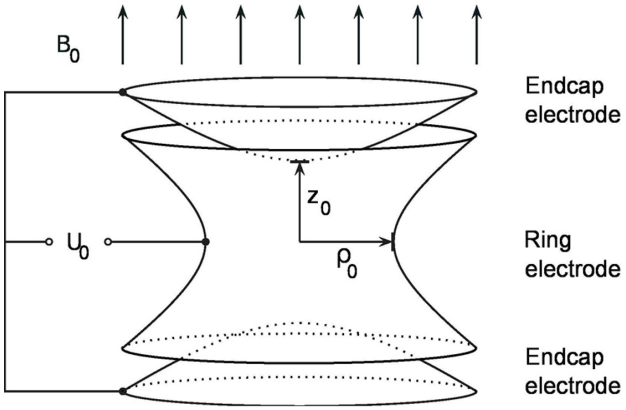

(a) Hyperbolical Penning trap

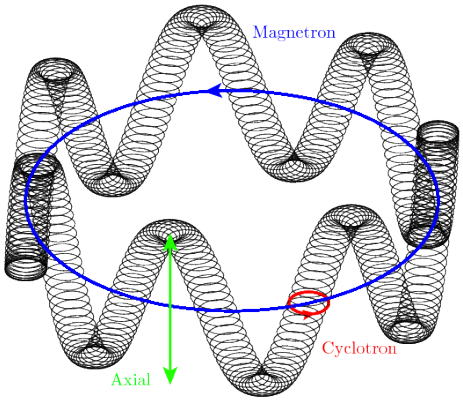

(b) Ion motion

Figure 2.5: (a) Schematic of a hyperbolical Penning trap (taken from [23]) and (b) ion motion in a Penning trap as a superposition of an axial oscillation (green), the slow magnetron motion (blue) and the fast cyclotron motion (red) (see Text, figure taken from [24]).

Penning trap, see Fig. 2.5a) or by a series of cylindrical electrodes (cylindrical Penning trap). The electric potential in cylindrical coordinates ρ and z is given by

$$\Phi(\rho, z) = \frac{U_0}{2d^2}\left(z^2 - \frac{\rho^2}{2}\right), \quad d^2 = \frac{1}{2}\left(z_0^2 + \frac{\rho_0^2}{2}\right) \tag{2.25}$$

with the inner radius of the trap electrode ρ_0 and the end cap distance $2z_0$ defined as in Fig. 2.5a. Radial confinement is achieved by a strong magnetic field along the trap axis, which is produced by a superconducting magnet. The ion motion (see Fig. 2.5b) consists of three decoupled motions, a harmonic longitudinal oscillation with frequency ω_z, a fast circular motion with the reduced cyclotron frequency ω_+ and a slow circular motion with the magnetron frequency ω_-. The superposition of these three motions is shown in Fig. 2.5b. Using the ion mass m, the ion charge Q and the magnetic field density B the free cyclotron frequency is given by

$$\omega_c = \frac{Q \cdot |B|}{m}. \tag{2.26}$$

The eigenfrequencies [12] of the ion are then given by

$$\omega_z = \sqrt{\left|\frac{Q \cdot U_0}{m \cdot d^2}\right|}, \tag{2.27}$$

$$\omega_\pm = \frac{\omega_c}{2} \pm \sqrt{\frac{\omega_c^2}{4} - \frac{\omega_z^2}{2}}. \tag{2.28}$$

The frequency ω_+ is called modified cyclotron frequency, ω_- is denoted as magnetron frequency. Note the relations

$$\omega_+ \gg \omega_z \gg \omega_-, \tag{2.29}$$

$$\omega_c = \omega_+ + \omega_-, \tag{2.30}$$

$$\omega_c^2 = \omega_+^2 + \omega_-^2 + \omega_z^2. \tag{2.31}$$

As demonstrated in [25] by Brown and Gabrielse, equation (2.31) is invariant under misalignments between electric potential and magnetic field, as well as under misalignments of the trap electrodes with respect to each other and in the case of a harmonic distortion of the quadrupole field. In [26], Gabrielse demonstrated, that also equation (2.30) allows mass measurement of the order of 10^{-7} to 10^{-9}.
In a quantum description, the three eigenmotions correspond to three decoupled harmonic oscillators with the frequencies ω_+, ω_z and ω_- and the corresponding quantum numbers n_+, n_z and n_-. The total energy of an ion in a Penning trap is given by

$$E(n_+, n_z, n_-) = \hbar\omega_+ \cdot (n_+ + 1/2) + \hbar\omega_z \cdot (n_z + 1/2) - \hbar\omega_- \cdot (n_- + 1/2) \tag{2.32}$$

Note the negative contribution of the magnetron motion. This is due to the fact, that a higher quantum number n_- corresponds to a bigger radius r_- and therefore a lower potential energy in the quadrupole potential (see equation (2.25)). This is not compensated by the increase in kinetic energy $E_{kin,-} = \frac{m\omega_-^2 r_-^2}{2}$. Fortunately, the coupling energy loss of the magnetron motion due to cyclotron radiation is that weak, that it can be considered as metastable [25] for an unperturbed ion. In contrast, interactions with a buffer gas enlarge the magnetron radius.
The motion of ions in a Penning trap can be resonantly excited using electric dipole fields oscillating with the eigenfrequencies stated in equation (2.27) and (2.28). Quadrupole excitations, instead can be used to couple frequencies with each other and transfer action between them. Opposite electrodes are on the same potential, neighbouring electrodes have the opposite sign. The needed frequencies are the sums or differences between two frequencies. Note especially the frequency $\omega_c = \omega_+ + \omega_-$, which can be used to couple cyclotron and magnetron motion. Applied with exactly the correct frequency a π-pulse can convert a magnetron motion into a cyclotron motion with the same radius and vice versa. A quantum mechanical description of ion motions and excitations in a Penning trap is given in [27].
As the cyclotron frequency in Eq. eq:cyclotronfrequency links mass and magnetic field, it can be either used for high-precision mass measurements in Penning Trap mass spectrometry if the magnetic field is well known, or for B-field measurements as in g-factor experiments. A non-destructive method to measure the eigenfrequencies ω_+, ω_- and ω_z or linear combinations of them with image current induced by their periodic motion in the trap [28, 29]. For short-lived nuclei, destructive methods using resonant excitation techniques are used [30–33].

2.2.1 The magnetic moment of the electron in a Penning trap

A classical particle with charge Q and mass m on a circular motion creates a magnetic moment μ, that is proportional to its magnetic moment $\vec{L}$:

$$\vec{\mu} = \frac{Q \cdot \hbar}{2m} \cdot \frac{\vec{L}}{\hbar} \tag{2.33}$$

with the reduced Planck constant $\hbar$. The spin $\vec{S}$ of a particle is an intrinsic angular momentum. It is a quantum physical quantity with the corresponding quantum number s. Its norm $|\vec{S}|$ is given by

$$|\vec{S}|^2 = s \cdot (s+1)\hbar^2 \tag{2.34}$$

with the reduced Planck constant $\hbar$. The fermions in the standard model, (see Fig. 1.1), for example the electron with mass m_e and charge $Q = -e$, have $s = 1/2$, bosons have integer spin. Like for charged particle circulating with an orbital angular momentum $\vec{L}$ (azimuthal quantum number l), also the spin is associated with a magnetic moment $\vec{\mu_s}$, which is given by

$$\vec{\mu}_s = g_s \cdot \frac{Q\hbar}{2m} \cdot \frac{\vec{S}}{\hbar}. \tag{2.35}$$

with the Landé-factor g_s, also called g-factor. From the relativistic Dirac equation, the g-factor of the free electron can be calculated to be $g_s = 2$. Additional corrections appear, that are described by the theory of quantum electrodynamics (QED)[34]. In the frame of Heisenberg's uncertainty principle, the electron can emit and reabsorb photons and create electromagnetic fields in the vacuum. The g-factor is also modified by interactions with an external electric field. The amplitudes of these interactions increase with higher orders of the electric field strength. In bound systems, they scale with powers of $(Z \cdot \alpha)$ with the electric charge of the nucleus and the fine structure constant $\alpha \approx 1/137$. Consequently, they are most pronounced for electrons bound to highly-charged ions. For a calculation for electron g-factors bound to hydrogen-like ions, see [4]. Electrons in hydrogen-like ions have no orbital angular momentum (in the ground state). Their magnetic moment can take two orientations in the magnetic field, denoted as spin up $|\uparrow>$ and spin down $|\downarrow>$. The corresponding potential energy in the magnetic field is given by

$$E_{mag,\pm} = -\vec{\mu} \cdot \vec{B} = \pm\frac{1}{2} \cdot g_s \frac{e\hbar}{2m_e} \cdot B. \tag{2.36}$$

Transitions between the two spin states can be induced by a magnetic field oscillating with the Larmor frequency

$$\omega_L = \frac{E_{mag,+} - E_{mag-}}{\hbar} = g_s \frac{e\hbar}{2m_e} \cdot B. \tag{2.37}$$

Experimentally, such a field can be provided with a microwave. In an inhomogeneous magnetic field of the form

$$B_z(z) = B_0 + B_2 \cdot (z^2 - \rho^2/2), \tag{2.38}$$

the sum of electric potential (see equation (2.25)) and magnetic potential energy of a stored particle is given by

$$E_{pot}(\rho, z) = Q\Phi(\rho, z) - \mu_z B_z(\rho, z) = -\mu_z B_0 + \left(\frac{QU_0}{2d^2} \pm \frac{1}{2} \cdot g_s \frac{e\hbar}{2m_e} B_2\right)(z^2 - \rho^2/2). \tag{2.39}$$

This results in a shift of the axial frequency given in equation (2.27), by

$$\delta\omega_z \approx \pm\frac{g_s}{2}\frac{\mu_B B_2}{M\omega_z} \tag{2.40}$$

with the sign given by the orientation of the spin in the magnetic field, the Bohr magnetron $\mu_B = \frac{e\hbar}{2m_e}$ and the ion mass M. (see [35]). This effect is called continuous Stern-Gerlach Effect [36].

2.3 Multi-reflection time-of-flight mass spectrometer/separator

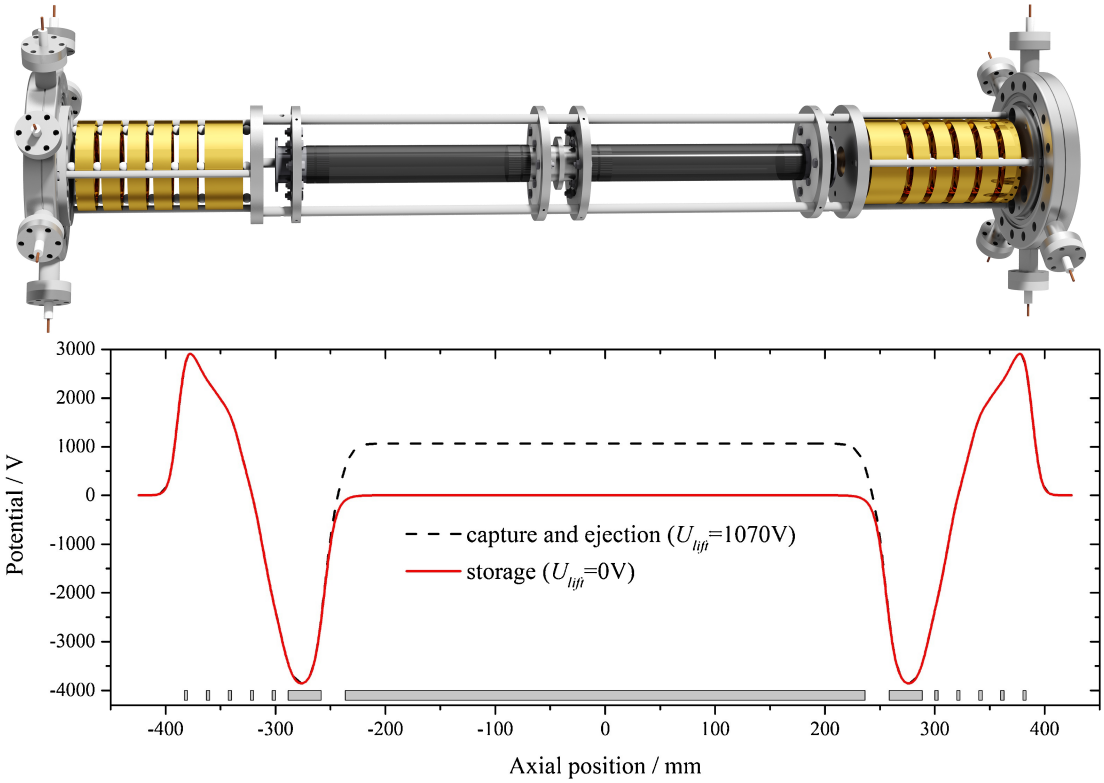

Figure 2.6: Top: Drawing of the ISOLTRAP MR-ToF MS [37]. Bottom: Axial electric potential distribution of the ISOLTRAP MR-ToF MS (taken from [38]).

A Multi-reflection Time-of-Flight Mass Spectrometer/Separator as the one at ISOLTRAP (see Fig. 2.6) is a compact device for high-precision time-of-flight mass spectrometry and separation of isobaric nuclei. It consists of two symmetric electrostatic mirrors and a pulsed drift tube in between. Each mirror is formed by a set of electrodes, creating a potential distribution as shown in Fig. 2.6. Inner electrodes on negative potential act as lenses to keep the ion beam focussed. Stable ion trajectories are obtained by ensuring point-to-parallel/parallel to point symmetry [39]. The outer electrodes are on positive potential. Ions with an energy lower than the highest mirror potential on the beam axis are reflected back and forth and therefore can travel long distances up to several kilometres inside a compact set-up. The mirror potentials are used to cancel the dispersion of the time-of-flight t with respect to the ion energy E. This

is described in the following.

2.3.1 Time-of-flight focussing

The ion beam is focussed in time-of-flight from an ion source to a detector by an MR-ToF MS as depicted in figure 2.7,

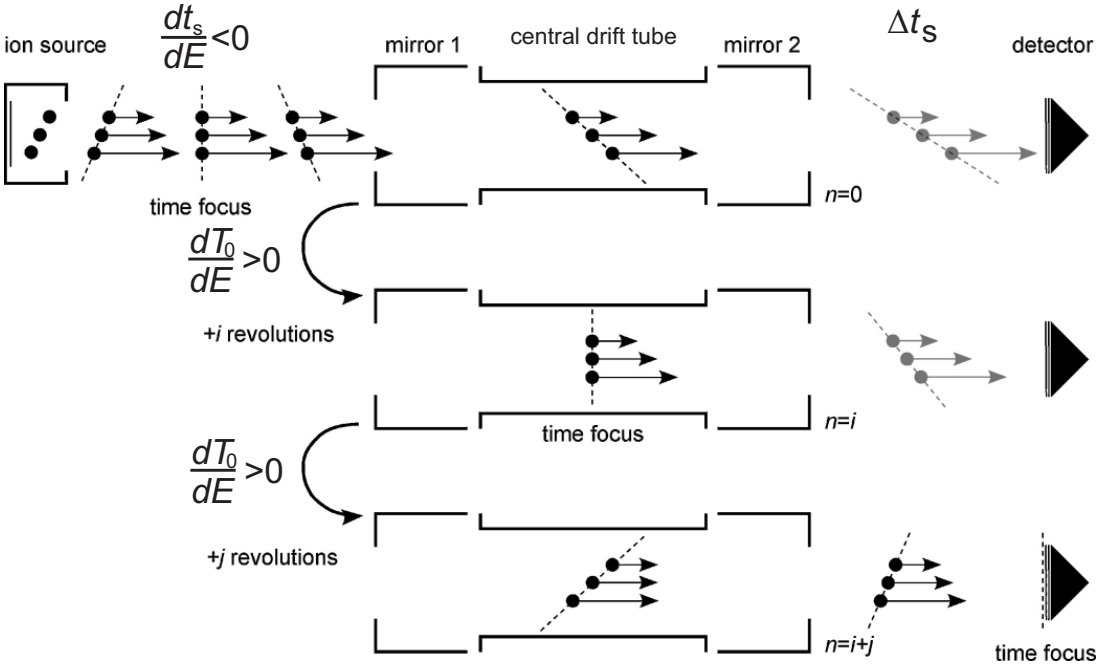

Figure 2.7: Working principle of an MR-ToF MS (modified from [40]). For details see text.

Row 1: The ions are stored inside an ion source with an initial longitudinal spread. They are extracted by switching electric potential, so that they are on a ramp. Ions in the back start on a higher potential. As the ions fly to the detector, the high energy ions overtake the low energy ions in a first time-of-flight focus and arrive earlier on the detector.

Row 2: The ions are trapped inside the MR-ToF MS. High energetic ions penetrate the potential further than low energetic ions before they are reflected. The mirror potentials are less steep than a quadratic potential, so that this additional flight path overcompensates the higher ion velocity inside the central drift tube of the MR-ToF MS. Therefore the low energy ions catch up and a second time-of-flight focus is reached.

Row 3: The ions are stored further inside the MR-ToF MS until they are enough in advance, that, after ejection, they are overtaken by the high energetic ions on the detector.

The width of the peak in a time-of-flight spectrum measured in a detector behind a not perfectly tuned MR-ToF MS (as in row 2 of Fig. 2.7) is composed by three parts.

1. The thermal turn-around time Δt_{therm}: ions, with the same potential energy and same position at the moment of extraction, but different direction of thermal motion need a different time-of-flight to the detector. The difference is given by the time, that ions with

an initial velocity antiparallel to the electric field of the extraction ramp E_x first need to turn around while ions with a velocity parallel to the electric field are directly extracted. The thermal turn-around time is given by

$$\Delta t_{therm} = \frac{\Delta p_{x,therm}}{e \cdot E_x} = \frac{\sqrt{m k_B T}}{e \cdot E_x} \tag{2.41}$$

and therefore by the ion temperature T. Here $\Delta p_{x,therm}$ is the thermal width in the longitudinal momentum distribution, e the elementary charge, m the ion mass and k_B the Boltzmann constant. The thermal width can by reduced by cooling.

2. A spread due to aberrations by different potentials the ions pass on their way to the detector Δt_{abb}. These differences are caused by field imperfections and unstable power supplies. If the flight distance is dominated by the distance inside the MR-ToF MS, contributions from outside can be neglected and this contribution is proportional to the number revolutions n inside the MR-ToF MS and the mean round trip time T_0 for this ion species.

$$\Delta t_{abb} = n \cdot \delta_{abb} \cdot T_0. \tag{2.42}$$

3. Time-of-flight differences emerging from the position of the ion in the source at the moment of extraction Δt_E. The total time-of-flight can be split into two parts:

$$t_E = t_{MR-ToF\ MS} + t_s. \tag{2.43}$$

Here, $t_{MR-ToF\ MS}$ is the time, the ions are trapped inside the MR-ToF MS, while t_s is the time, the ions need on their direct way to the detector, as shown in row 1. Downstream of the first focus point between the RFQ and the MR-ToF MS, the dispersion

$$\Delta t_s = -\frac{\partial t_s}{\partial E} \cdot \Delta E > 0. \tag{2.44}$$

holds. The sign was chosen to have a positive width Δt_s. Inside the MR-ToF MS, high energetic ions have a longer round-trip time T_0. Here, the dispersion

$$\frac{\partial t_{MR-ToF\ MS}}{\partial E} = n \cdot \frac{\partial T_0}{\partial E} > 0 \tag{2.45}$$

holds. If all ions would start simultaneously inside the MR-ToF, this would give rise to an energy dependent spread in time $\Delta t_{MR-ToF\ MS}$, which is proportional to the number of revolutions before ejection n and the dispersion of the time round-trip time T_0. So in total

$$\Delta t_E = \frac{\partial t_E}{\partial E} \cdot \Delta E = n \cdot \frac{\partial T_0}{\partial E} \cdot \Delta E - \Delta t_s. \tag{2.46}$$

As all three components can be considered as independent random distributions, the central limit theorem applies, so that they are added in quadrature to obtain the total time-of-flight width

$$\Delta t = \sqrt{\Delta t_{therm}^2 + \Delta t_{abb}^2 + \Delta t_E^2} \tag{2.47}$$

$$= \sqrt{\Delta t_{therm}^2 + (N \cdot \delta_{abb} \cdot T_0)^2 + (\Delta t_s - n \cdot \frac{\partial T_0}{\partial E} \cdot \Delta E)^2}. \tag{2.48}$$

For a proper choice of n and $\frac{\partial T_0}{\partial E}$, Δt_E vanishes.

$$\Delta t_E = \frac{\partial t_E}{\partial E} \cdot \Delta E = n \cdot \frac{\partial T_0}{\partial E} \cdot \Delta E - \Delta t_s = 0 \tag{2.49}$$

as depicted in row 3 of Fig. 2.7 and a time focus on the detector is achieved. The mass resolving power is given by

$$R = \frac{t}{2\Delta t} = \frac{t_s + n \cdot T_0}{2\sqrt{\Delta t_{therm}^2 + (n \cdot T_0 \cdot \delta_{abb})^2}}. \tag{2.50}$$

At ISOLTRAP, typical mass resolving power of $R \approx 10^5$ is obtained for $n = 1000$ revolutions in the MR-ToF MS.

2.3.2 MR-ToF mass spectrometry and separation

The time-of-flight t of an ion with charge q, energy (kinetic plus potential) E and mass m from its trajectory C from its position at the moment of extraction to the detector is given by the path integral of the inverse ion velocity along its trajectory

$$t = \int_C \frac{ds}{v(s)} + b = \int_C \sqrt{\frac{m}{2(E - q \cdot \Phi(s))}} ds + b =: a \cdot \sqrt{m} + b \tag{2.51}$$

with b being a constant due to not instantaneous triggers and detection, $v(x)$ the velocity and $\phi(x)$ the electric potential at position x. The factor a consists of a contribution linear to the number of revolutions n coming from the path the ions travel while being trapped in the MR-ToF MS. There is a constant contribution, too, coming from the direct path from the ion source/buncher to the detector, which the ion passes only once. In an MR-ToF mass measurement, two reference ions with well-known masses m_1 and m_2 are used to calibrate the factors a and b, so that the mass of the ion of interest (IoI) can be deduced. This is done by calculating the observable

$$C_{ToF} = \frac{2t - t_1 - t_2}{2(t_1 - t_2)} \tag{2.52}$$

as described in [7]. The mass of the ion of interest is then given by

$$m = C_{ToF} \cdot (\sqrt{m_1} - \sqrt{m_2}) + (\sqrt{m_1} + \sqrt{m_2})/2 \tag{2.53}$$

and can be reevaluated anytime the literature values of the reference masses change. The reference ions can be either ions from the on-line or an off-line ion source. On-line references are isobaric ions that are delivered with the same beam as the ion of interest and therefore appear in the same recorded spectrum as contamination. They are affected by the same systematic drifts like voltage instabilities, and therefore can be used to compensate for them [41] and to monitor the time-of-flight and count rate stability. A disadvantage is that the count rate has to be adapted for the more abundant contaminant to avoid a saturation of the detector and space charge effects in the MR-ToF MS. In contrast, off-line references are produced from a reference ion source and are measured before and after the ion of interest. Consequently, also less abundant ions are accessible, but with the price of a higher susceptibility for systematic errors.

Once the peak of the ion of interest was identified, the MR-ToF MS can be used as mass separator. Selective extraction timings can be used to separate the ion of interest from the

isobaric contamination and to prepare it for Penning-trap measurements.

2.4 Einzel lenses

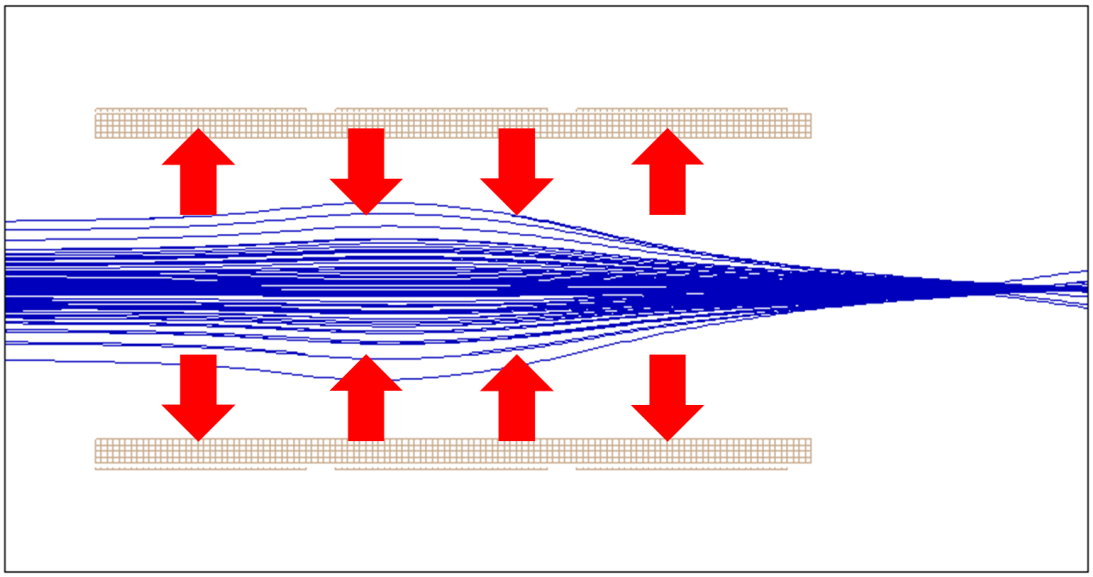

Figure 2.8: Ion trajectories in an Einzel lens with positive voltage on the central electrode with positive ions. The focussing and defocussing effect in different sections (see text) is illustrated with red arrows.

To transport the ions, it is necessary to focus the diverging ion beam. This is done by Einzel lenses. They consist of three subsequent and cylindrical electrodes coaxial with the ion beam. The outer electrodes are grounded (or on a global potential offset for the whole lens) while the central one is on positive or negative potential. The focussing effect is achieved by the fringe fields at the borders of the electrodes. The working mechanism for a positive potential is illusted in Fig. 2.8 and can be understood by tracking the influence on the ion motion in four sections.

1. Leaving electrode 1: The potential close to the electrode is forced to be close to ground, while the positive potential of electrode 2 penetrates electrode 1 in the centre. Therefore, the ions are slowed down and defocussed.

2. Entering electrode 2: The potential close to the electrode is forced to be positive, while it is closer to ground near the beam axis, where it increases more slowly. Consequently, the ions are slowed down and pushed towards the center.

3. Leaving electrode 2: While the potential is forced to be on the electrode potential for radii close to the electrode radius, it is smaller on the beam axis, where it starts to decrease already inside the electrode. Consequently, the ions are pushed towards the central axis while being accelerated.

4. Entering electrode 3: As the positive potential of electrode 2 penetrates electrode 3 in the centre, the ions are pushed outside while being accelerated.

While the focussing forces in steps 2 and 3 are of comparable size as the defocussing in step 1 and 4, the time they are acting is longer since the ions move more slowly in the positive potential. Therefore, a net focussing effect is achieved. In addition, this explains why the positive potential must be of the order of the kinetic energy of the ions, but not too high, to avoid a reflection of the ion beam, if a considerable effect should be achieved. A focussing effect can also be achieved by applying a negative potential on the central electrode. In this case, the same steps apply, but in the order 3-4-1-2 (focussing and accelerating - defocussing and accelerating - defocussing and decelerating - focussing and decelerating). Since the ion velocity is again smaller in the two focussing sections, the net effect is again focussing. For negative voltages, there is no risk of reflecting ions, but since the velocity of the ions scales with $\propto \sqrt{E_{kin}}$, the applied voltages have to be much higher than for positive polarity. On the other hand, since the ions are first focussed, the maximal beam diameter and the dispersion $\frac{\partial t}{\partial E}$ are smaller.

2.5 Electromagnetic waveguides

The dynamic of electric fields $\vec{E}$ and magnetic fields $\vec{B}$ is described by the four Maxwell equations

$$\vec{\nabla} \cdot \vec{E} = \frac{\rho}{\epsilon_0}, \tag{2.54}$$

$$\vec{\nabla} \cdot \vec{B} = 0, \tag{2.55}$$

$$\vec{\nabla} \times \vec{E} = -\frac{\partial \vec{B}}{\partial t}, \tag{2.56}$$

$$\vec{\nabla} \times \vec{B} = \mu_0 \cdot \vec{j} + \epsilon_0 \mu_0 \frac{\partial \vec{E}}{\partial t}. \tag{2.57}$$

Here, ρ is the electric charge density, ϵ_0 the electric field constant, $\vec{j}$ the charge current density and μ_0 the magnetic field constant. In free space, $\rho = \vec{j} = 0$. Equations (2.54)-(2.57) are solved by plain waves travelling with the speed of light $c = \frac{1}{\sqrt{\epsilon_0 \mu_0}}$. Electric and magnetic field are both transversal to the direction of motion and perpendicular to each other. On the surface of an electric conductor, the electric and magnetic field components orthogonal and parallel to the surface, marked with $\perp$ and $\parallel$ have to fulfill the conditions

$$E_\parallel = 0, \quad , E_\perp = \rho_s/\epsilon_0, \quad B_\parallel = j_s/\mu_0, \quad B_\perp = 0 \tag{2.58}$$

with the surface charge and current densities ρ_s and j_s. Waveguides [42] are hollow pipes made of an electric conductor which are used to guide microwaves and exist with rectangular and circular shape. In both cases, the equations eqs. (2.54)–(2.58) are solved with two types of waves: Transverse Electric (TE) waves, also called M-waves have a longitudinal B-field component and a purely transversal electric field. Transverse Magnetic (TM) or E-waves have a longitudinal E-field component and a purely transversal electric field. The solutions are categorized for rectangular waveguides by the number of points with zero longitudinal field between the conductor surfaces in both transversal directions. For circular waveguides, their are ordered buy the number of zeros in radial direction and by their rotational symmetry. In

both cases, the fields travel along the longitudinal z-axis as

$$\vec{E}(x,y,z,t) = \vec{E_0}(x,y)\cos(2\pi\nu t - (k-k_c)z) \tag{2.59}$$

with a mode dependent cut-off wave number

$$k_c = \frac{2\pi}{\lambda_c} = \frac{2\pi}{c}\nu_{cut-off}. \tag{2.60}$$

Here, c is the speed of light in the medium inside the waveguide, λ_c und $\nu_{cut-off}$ are the cut-off wavelength and frequency. For a rectangular waveguide with along the z-axis with surfaces at $x = 0$, $x = a$, $y = 0$ and $y = b$ and $a \geq b$, the solutions are summarized in Tab. 2.1. E_0 and B_0 are the field amplitudes, m and n are natural numbers. The dominant mode with the lowest $\nu_{cut-off}$ is the TE10 mode. For circular waveguides, the Maxwell equations have to be solved

Table 2.1: Electromagnetic waves in a rectangular waveguide

wave type	longitudinal field amplitude	cut-off frequency	first mode
TM	$E_z^0(x,y) = E_0 \sin\left(\frac{m\pi}{a}x\right)\sin\left(\frac{n\pi}{b}y\right)$	$\nu_{cut-off} = \frac{c}{2}\sqrt{\left(\frac{m}{a}\right)^2 + \left(\frac{n}{b}\right)^2}$	TM11
TE	$B_z^0(x,y) = B_0 \cos\left(\frac{m\pi}{a}x\right)\cos\left(\frac{n\pi}{b}y\right)$	$\nu_{cut-off} = \frac{c}{2}\sqrt{\left(\frac{m}{a}\right)^2 + \left(\frac{n}{b}\right)^2}$	TE10

in the cylindrical coordinates ρ, ϕ, z. Here, the solutions for a waveguide with radius a along the z-axis are given in Tab. 2.2 Here, $J_\nu(x)$ is the Bessel function of first kind of order ν and

Table 2.2: Electromagnetic waves in a circular waveguide

wave type	longitudinal field amplitude	cut-off frequency	first mode
TM	$E_z^0(\rho,\phi) = E_0 \sin(\nu(\phi-\phi_0)J_\nu(\frac{p_{\nu n}}{a}\rho)$	$\nu_{cut-off} = \frac{c}{2\pi}\frac{p_{\nu n}}{a}$	TM01
TE	$B_z^0(\rho,\phi) = B_0 \sin(\nu(\phi-\phi_0)J_\nu(\frac{p'_{\nu n}}{a}\rho)$	$\nu_{cut-off} = \frac{c}{2\pi}\frac{p'_{\nu n}}{a}$	TE11

$p_{\nu n}$ its n'th zero. $p'_{\nu n}$ is the n'th zero of the first derivative of $J'_\nu(x) = \frac{\partial}{\partial x}J_\nu(x)$. ϕ_0 is an angle with respect to the x-axis, which defines the polarity of the wave. In Fig. 2.9, the transversal electric and magnetic field for the modes TM01, TE01, TE11 and TM11 in a circular waveguide are displayed. The dominant mode is the TE11 mode with

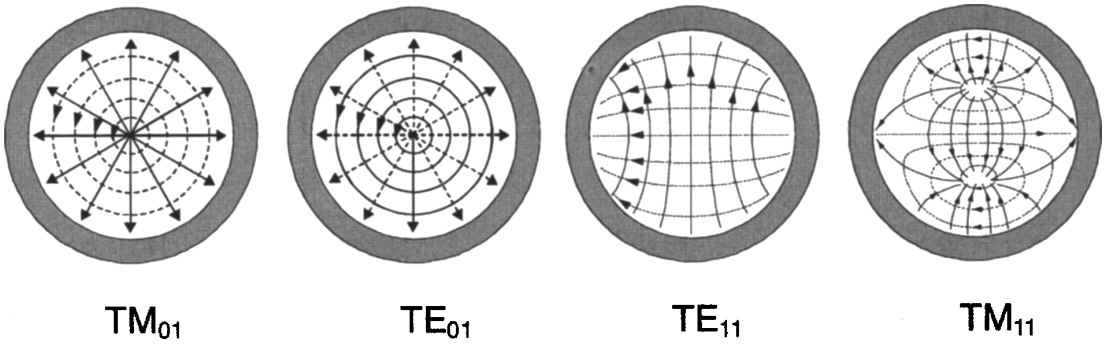

Figure 2.9: Transversal electric (solid lines) and magnetic fields (dotted lines, for TE11 horizontal lines) in a circular waveguide made (taken from [43]).

$$\nu_{cut-off,\ TE11} = \frac{c}{2\pi}\frac{1.8412}{a}. \tag{2.61}$$

The second mode is the TM01 mode with

$$\nu_{cut-off,\ TM01} = \frac{c}{2\pi}\frac{2.4048}{a}. \tag{2.62}$$

For a frequency range between the cut-off frequencies of the first two modes, a waveguide is called to be single mode since only the ground mode can pass. Independent of the waveguide form, the wave impedance for TE waves is frequency dependent and given by

$$Z(\nu) = \sqrt{\frac{\mu_0\mu_r}{\epsilon_0\epsilon_r}} \cdot \left(1 - \left(\frac{\nu}{\nu_{cut-off}}\right)^2\right)^{-1/2} \tag{2.63}$$

with the electric and magnetic permeabilities ϵ_r and μ_r of the medium. For TM waves, the impedance is given by

$$Z(\nu) = \sqrt{\frac{\mu_0\mu_r}{\epsilon_0\epsilon_r}} \cdot \left(1 - \left(\frac{\nu}{\nu_{cut-off}}\right)^2\right)^{1/2}. \tag{2.64}$$

3 Microwave injection for the ALPHATRAP experiment

The ALPHATRAP experiment is a new cryogenic Penning-trap experiment at the Max Planck Institute for Nuclear Physics (MPIK) in Heidelberg, Germany. It is supposed to measure the magnetic moments of electrons bound to highly-charged ions delivered by the Heidelberg EBIT [44] and to perform laser spectroscopy. The ALPHATRAP experiment is described for example by Sandro Kraemer in [45]. A review giving a detailed description of the experiment will be published in autumn 2018. The ALPHATRAP experiment is similar to an existing experiment in Mainz, that measured the g-factor of an electron bound in to hydrogen-like ions as e.g. $^{12}C^{5+}$ [35], $^{28}Si^{13+}$ and lithium-like $^{40}Ca^{17+}$[6]. In this chapter, the design of a transport system for microwaves to the ALPHATRAP trap tower needed to measure the Larmor (spin-flip) resonance is described.

3.1 The ALPHATRAP setup

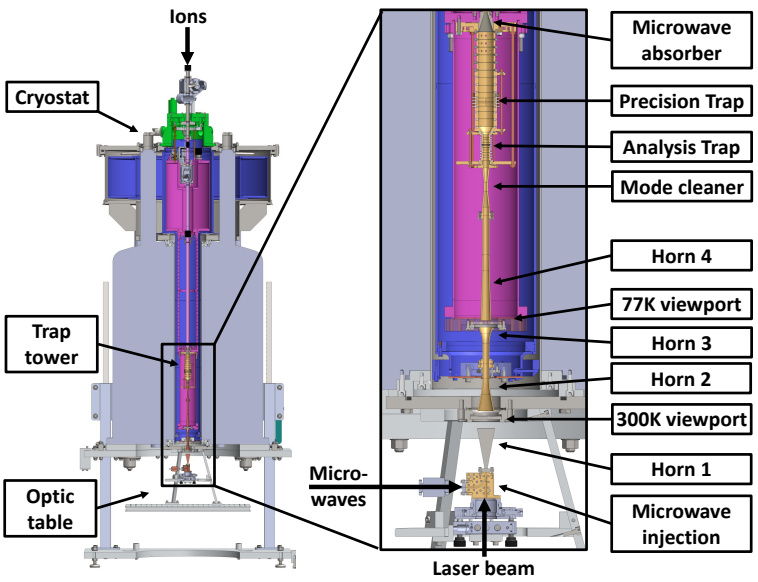

Figure 3.1: The ALPHATRAP magnet with cryostat on top and optic table for the laser setup below. Ion are transferred to the setup and injected from above. In the in-set, a zoom on the microwave injection and the trap tower is shown. The trap and regions in purple are cooled with liquid helium, blue regions are cooled with liquid nitrogen. Figure courtesy by Tim Sailer.

A cross section of the ALPHATRAP magnet is displayed in Fig. 3.1. It contains a trap tower with two cylindrical Penning traps. In the Precision Trap (PT) with a homogeneous magnetic

field of strength $B \approx 4.023\,\mathrm{T}$ [1], the cyclotron frequency ν_c (see eq. (2.26)) of a stored ion is measured using an image current detection technique described in [29]. The Larmor frequency ν_L (see chapter 2.2.1) is measured by resonant irradiation with a microwave at this frequency. The observed quantity is the spin flip probability depending on the microwave frequency. Spin flips are identified in the Analysis Trap (AT) with $B \approx 3.867\,\mathrm{T}$[1] using the continuous Stern-Gerlach effect (see chapter 2.2.1) in an inhomogeneous magnetic field. To identify the spin state, spin flips are induced with a microwave and the sign of the shift of the axial frequency (see eq. (2.40)) is detected. The g-factor of the electron with charge e and mass m_e bound to an ion with charge Q and mass M can be deduced using the frequency ratio $\Gamma := \frac{\nu_L}{\nu_c}$ as

$$g = \Gamma \cdot \frac{Q}{e} \cdot \frac{2m_e}{M} \tag{3.1}$$

as it was done for example in [35]. Also spin-flips induced by resonant excitation of the stored ions with a spectroscopy laser can be detected this way. To reach the needed sensitivity, the axial motion of the stored ions is is resistively cooled using electronic negative feedback [46] and sympathetically with laser cooled $^9Be^+$ ions [45]. The highly-charged ions are produced by the Heidelberg EBIT [44] or other ion sources [47] and are transported through a beamline to the trap tower and inserted from above. The trap tower is cooled down to 4.2 K with liquid helium (see pink coloured area). The trap is surrounded by a heat shield cooled with liquid nitrogen to a temperature of 77 K (see blue area).
The microwaves, the cooling laser beam and the spectroscopy laser beam all need to be injected axially into the trap tower to have full intensity in both traps. To maintain the temperature of the cryogenic trap and the heat shield, metallic connection between the different temperature sections have to be avoided. In this chapter, the design of the transport system for microwave power from room temperature to the trap region using four microwave horns and of a device to align the microwaves with the cooling and spectroscopy lasers is described. The system was designed for measurements with electrons bound to hydrogen-like ions with g-factors close to the one of $^{28}Si^{13+}$ of $g = 1.9953489580(18)$ (from [35]), but was also designed to allow a switching to boron-like ions with minimal modifications. The described components are the ones labelled as laser injection, horn 1-4 and mode cleaner in Fig. 3.1.

3.2 Laser injection

The microwaves are produced by a frequency generator and the frequency multiplier S08MS by OML. The datasheet can be found in [48]. They are transported to the optical table displayed in Fig. 3.1 with rectangular waveguides (see section 2.5), that only allow the dominant mode TE10 to pass. The lasers for cooling the $^9Be^+$ ions and for spectroscopy experiments have to enter the trap the same way as the microwaves do. In the case of hydrogen-like ions, the waveguide size is similar to the laser beams. Therefore, a special device to align the microwaves with the laser beams with low power loss had to be designed. In the following, first the requirements for such a device are listed, and then simulations using the RF module of COMSOL Multiphysics® [49] and the design of the device are presented.

[1] Measured by Martin Höcker.

3.2.1 Requirements

The laser injection has several requirements to fullfil:

1. The laser must have to pass straight through the device.

2. The laser beam and the microwaves should enter from different input ports and exit through the same output port aligned with each other.

3. The diameter of the beam path should be as high as possible to maintain the full laser power and beam quality.

4. The microwave transmittance should be as big as possible. Resonances in the transmission spectrum with respect to the microwave frequency have to be much broader than a Larmor resonance, which has a relative width on the order of 10^{-8} [50].

Commercial solutions like directional couplers as described in Fig. 3.2 (using port 3 as microwave input, port 2 as laser input and port 1 as common output) were discarded due to the intrinsic loss of at least 50 % of the microwave power and an unnecessary long narrow section for the laser path. Therefore, a custom laser injection displayed in Fig 3.3a was designed.

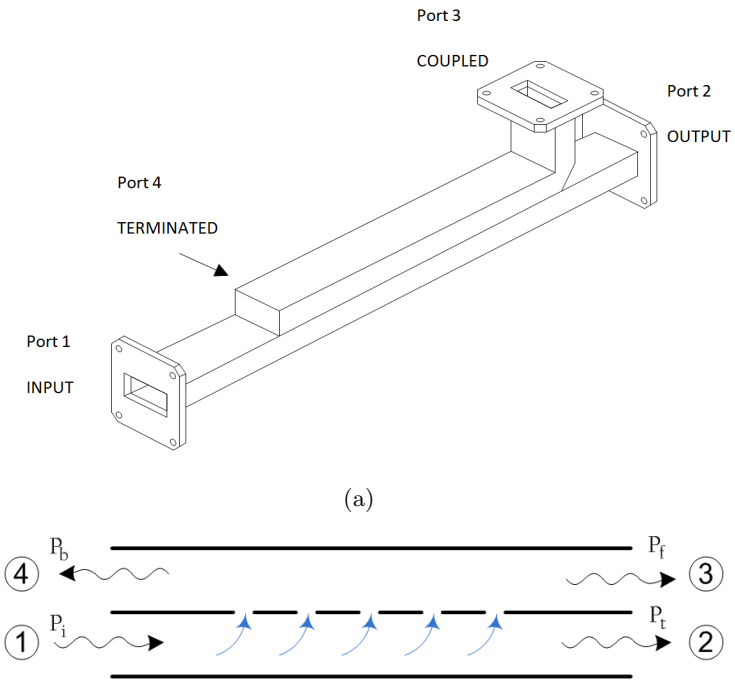

Figure 3.2: (a) Typical design and (b) working principle of a monodirectional coupler. The distance between two slits is one fourth of a wavelength. P_i denotes the input power, P_t is the power transmitted straight while P_f was coupled into the another output in forward direction. P_b is the coupled power in backwards direction. Destructive interference yields $P_b = 0$. For ideal coupling, $P_f = P_t = P_i/2$. Both figures were taken from [51].

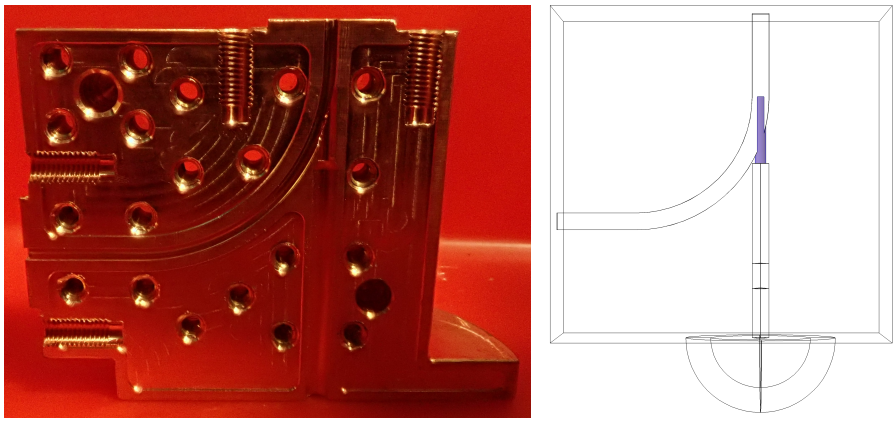

(a) Manufactured laser injection (b) COMSOL drawing

Figure 3.3: (a) Photo of one half of the laser injection, (b) COMSOL drawing with laser opening highlighted. The lower half circle is an air filled domain also included in the simulations. The microwaves enter from the left, the laser from below.

3.2.2 Custom laser injection

The custom laser injection consists of a rectangular waveguide, which is bent by 90°. This waveguide has dimensions, that only allow the dominant rectangular TE01 mode to pass. (For circular waveguides, the TE11 mode is dominant, see chap. 2.5). The laser beam enters tangentially through a circular opening (the blue domain in Fig 3.3b), which is smaller then the long side of the waveguide. This makes it non-transparent for the microwaves. Like this, power losses through the laser input and reflections due to change of impedance at the junction are minimized.

Simulations

The transmission of microwaves with the needed frequencies of around 113 GHz was simulated with COMSOL Multiphysics® RF module [49] for rectangular and circular shapes of the laser opening with different sizes. For this, the dimensions of the domain marked in blue in the COMSOL drawing in Fig.3.3b was changed. For rectangular openings, one dimension was chosen to be the same as the short dimension of the rectangular waveguide and the size of the second dimension b was varied. For circular openings, the diameter d of the opening was varied. The results are shown in Fig. 3.4. A circular shape with a diameter of 1.3 mm was chosen, since it is the best compromise between transmission of the microwave signal and the size for the laser beam. Experimentally, frequencies close to or below the $^{28}Si^{13+}$ Larmor frequency at $\nu_L = g \cdot \mu_B B \approx 112.35\,\text{GHz}$ (see Eq. 2.37 with the Bohr magnetron $\mu_B = \frac{e\hbar}{2m_e}$) will be needed in the Precision Trap. In this range, the transmission is higher than 80 %. The simulated time-averaged electric field strength for the chosen geometry and a microwave frequency of 112 GHz is depicted in Fig. 3.5a and for 115 GHz in Fig. 3.5b with identical color range. The voltage standing wave ratio

$$VSWR = \frac{E_{in} + E_R}{E_{in} - E_R} \tag{3.2}$$

with the electric field amplitudes E_{in} for the incoming wave and E_R for the reflected wave increases between these two frequencies from 1.99 to 3.01. Therefore, the interference pattern

in the part where incoming and outgoing wave overlap is more pronounced for 115 GHz. A larger diameter and a rectangular shape with similar size lead to a much lower transmission. On the other hand, the transmission for smaller diameters did not increase a lot. The hole for the laser is designed to be that narrow only for a short section at the junction with the waveguide. The remainder is designed with a larger diameter of 2 mm to make the assembly less sensitive to misalignments (see Fig. 3.3b).

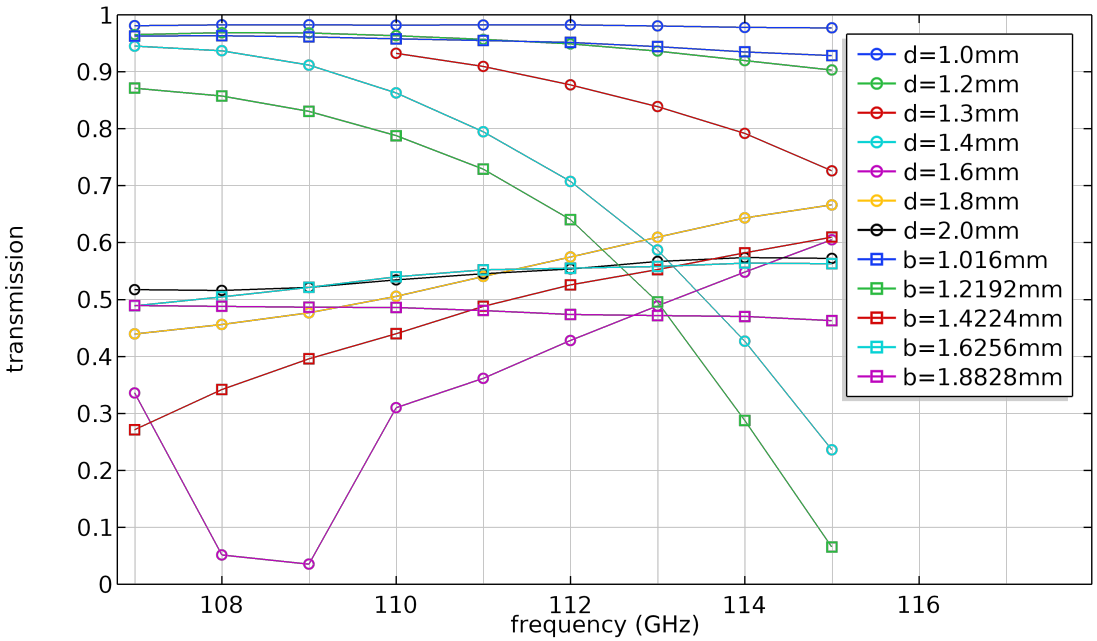

Figure 3.4: Microwave power transmission of the laser injection depending on the microwave frequency and the diameter d (circles) or rectangular base b (squares, second dimension is equal to the size of the waveguide of 1.016 mm or 0.04 inch) of the laser input port (high-lighted domain in Fig. 3.3b). The needed frequencies are below 112.6 GHz.

Design

The laser injection was designed in cooperation with the design office of the Max Planck Institute for Nuclear Physics (MPIK) and manufactured by the mechanical workshop. It consists of two halfs made of gold-plated copper. A drawing of one of them is displayed in Fig. 3.3a. Into each half, the waveguide structures are milled with 50% depth. The blocks are pressed together by a large number of screws, especially around the waveguide. Then, the round input for the laser is drilled into the copper block. At the connection point of laser input and waveguide, the diameter is 1.3 mm. A second drilling with a diameter of 2 mm ending close to the connection makes the hole wider with the aim of making alignment easier. In the end, everything is gold-plated with a 15 µm thick layer to improve the quality of the electric contact between the plates. The faces of the copper blocks, except for a strip along the waveguide structures and the outer edge, is recessed by 0.2 mm, so that only this strips are touching each other. This increases the contact pressure on the relevant points. On the bottom side of the two halfs, a mounting plate is machined to fix it on the 6 axis mount K6XS by Thorlabs. This is used to adjust angle

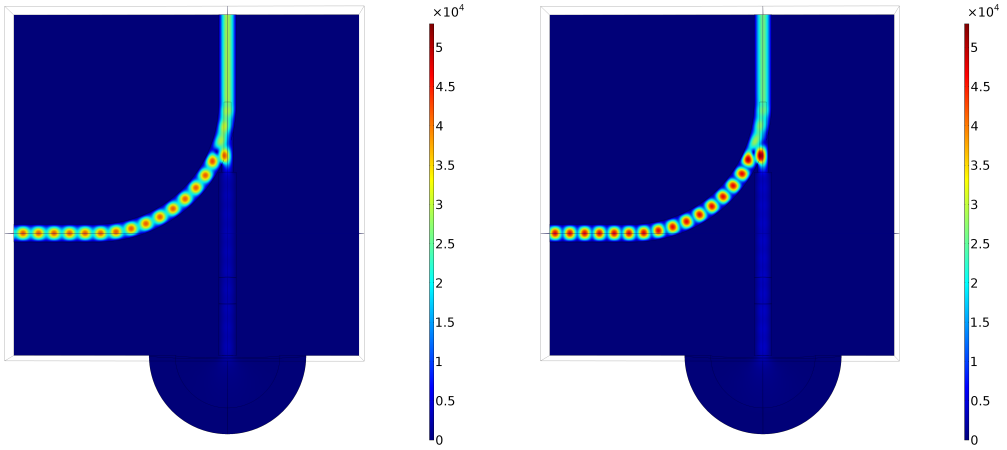

(a) 112 GHz (b) 115 GHz

Figure 3.5: (a) Electric field norm for the chosen geometry of the laser injection with 112 GHz, (b) electric field norm in the laser injection for a microwave frequency of 115 GHz. The color legend is in $\mathrm{V\,m^{-1}}$ for an input power of 1 W. The microwaves enter from the left, the laser from below. The half circle in (b) to (b) is filled with air.

and position with high accuracy. On the microwave input port on the left and on the output port on the top, WR08 flanges to connect to a waveguide and to a horn antenna, respectively. Boron-like $^{40}Ar^{13+}$ has a g-factor in the ground state of $g = 0.6636477(7)$ [52]. Therefore, the Larmor frequency in the Precision Trap is only $\nu_L \approx 37.36\,\mathrm{GHz}$ and therefore below the cut-off frequency of the waveguide in the laser injection. Therefore, the laser injection has to be replaced in case these systems get studied. Since the wavelength is also 3 times larger, it suffices to bore a hole for the laser of similar size into a bent waveguide and one still obtains good microwave transmission.

3.3 Transfer horns and mode cleaner

To transport the microwaves from the room temperature section to the cryogenic trap, four microwave horns are needed (see Fig. 3.1), two sending horns (horn 1 and 3) and two receiving horns (horn 2 and 4). In the centre of the rotationally symmetric Penning traps, a microwave field as homogeneous as possible is required for the spin flip probability being independent from the ion position. The traps also form a circular waveguide. For an ideal field distribution, only the transverse electric TE11 mode, which is the dominant mode for circular waveguides, should be transmitted. For the room temperature horn 1, the commercial rectangular standard gain horn 261F-25/387 by miwave (datasheet see [53]) was ordered. It has a rectangular input WR08 flange, with which it is mounted on the laser injection. Due to this flange, it can only be used for the hydrogen-like systems. The other three horns were chosen to be conical, to prevent any issues from a possible tilt between the three separated sections. The inner diameter of the horns and connecting straight section was chosen to define a cut-off frequency $\nu_{cut-off,\ TE11}$ of 27.5 GHz. Consequently, they are single mode for the frequencies needed for boron-like systems and multi-mode for hydrogen-like systems. The design of the horns 2, 3 and 4 and of a mode cleaner to filter out unwanted modes for hydrogen-like systems, as well as simulations of the transmission are described in this section.

3.3.1 General design of a horn antenna

Horn antennas are built to guarantee a smooth, adiabatic transition between the impedance in a waveguide and in the vacuum. As can be seen from equations (2.63) and (2.64), the impedance for both, TE and TM waves converges to the vacuum impedance as the radius of a waveguide is going to infinity, but is different from it for any finite radius. Therefore, reflections at the opening of a horn are unavoidable, but can be reduced by a big horn radius. On the other hand, space is limited and a big radius also yields a big spatial spread of the power. An edge also causes power transfer between different modes, especially from the desired circular TE11 mode to the unwanted TM11 mode. To minimize this, the designed horns consist of three sections.

1. A straight section connected to the waveguide with a flange.
2. A transition section. The walls of the horn dynamically change from a pipe to a cone. The horns are revolved from a plane. In this plane, the transition element consists of a sector of a circle, that is tangential to the pipe and the following conical section.
3. A conical section.

Due to issues in the manufacturing process, the transition section is constrained to be shorter than 2.5 cm. Bending radii and lengths had to be optimized with simulations. As an example, horn 3 is depicted in Fig. 3.6.

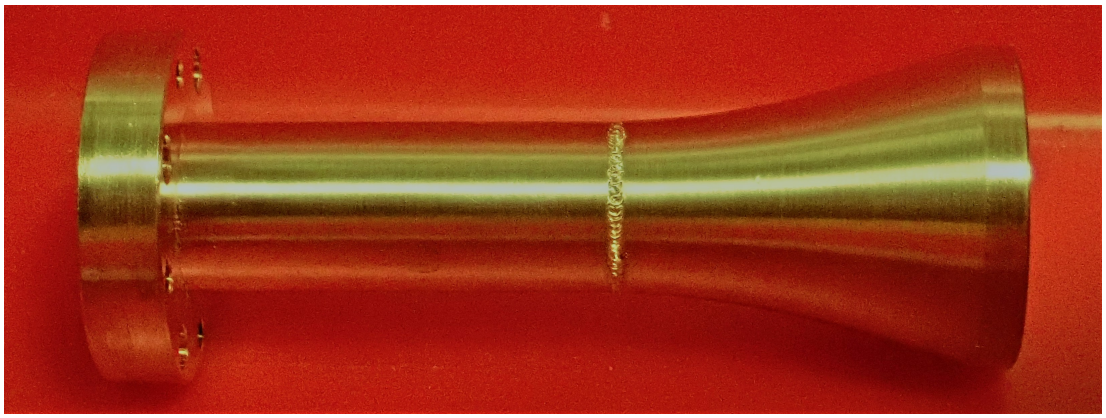

Figure 3.6: Horn 3. The total length of the horn is 46.138 mm including flange (4.5 mm), circular waveguide (22.5 mm, on the left of the welding), transition section (12.138 mm, on the right of the welding) and conical section (7 mm).

3.3.2 Mode cleaner

For experiments with hydrogen-like ions, an additional device to filter out higher modes than the dominant mode, in the following called mode cleaner, had to be designed. For the circular geometry from horn 2 on, this is the circular TE11 mode (see chap. 2.5). The mode cleaner is a tapering of the circular waveguide just before the connection to the trap chamber (see Fig. 3.1) with a minimal diameter of 1.9 mm and a subsequent widening to the diameter of the trap of the opening of the trap chamber of 6 mm. A picture of the mode cleaner is depicted in Fig. 3.7a. When changing from hydrogen-like ions to boron-like ions, this component will have to be exchanged, as well as the room temperature components.

3.3.3 Simulations of transfer horns and mode cleaner

In a first step, the transmission of the first mode TE11 and the second mode TM01 through the mode cleaner was simulated with a microwave frequency of 113 MHz. First in 2D making use of the rotational symmetry. Then, the results were confirmed using simulations in 3D. The simulated electric field distributions are presented in Fig. 3.7b for an input signal in the TE11 mode and in Fig. 3.7c for an incoming TM01 wave. The transmission is 97 % for the TE11 mode while the TM01 mode is blocked completely (transmission 4×10^{-9}), reflections cause an interference pattern. However, an incoming TE11 wave passes the tapering. 2D axis-symmetric simulations of the transmission through all four horns and the mode cleaner where performed. All lengths of the conical sections, the transitions and the opening angles of the horns where varied in the limits given by the available space to obtain maximal transmission. For these simulations, also horn 1 was assumed to be conical to conserve the symmetry. This was necessary to reduce the needed computation time. Around the regions of unbound wave propagation between the horns, spherical domains of free space were included to account. An overview over such a simulation is given in Fig. 3.8a. In Fig. 3.8b, a zoom on the region around the two first horns is shown. In the waveguide on the left, the superposition of incoming and reflected wave is visible. On the right of horn 1 the microwaves with the incoming TE11 mode first transform to plane waves in the free space and are then recaptured by horn 2. In the subsequent circular waveguide, as well as in the one behind horn 4, the superposition of several modes and of incoming and reflected waves is visible. These modes are successfully filtered out by the mode cleaner. The frequency dependence of the transmission was scanned close to the expected Larmor frequency of hydrogen-like $^{28}Si^{13+}$ of 112.27 GHz in the precision trap ($B = 4.02\,\mathrm{T}$) and 107.4 GHz in the analysis trap ($B = 3.846(17)\,\mathrm{T}$, g-factor from [4]). Both spectra are depicted in Fig. 3.9. Clear resonances are visible. Since the distances between the horns in the experiment might deviate from the simulated ones, the position of the resonances might change. The resonance peaks have a relative width of $\Delta_\nu/\nu \approx 0.2\,\mathrm{V}/112\,\mathrm{GHz} \approx 2 \cdot 10^{-3}$ and are therefore much broader than a typical Larmor resonance. All components were manufactured by the mechanical workshop of the MPIK.

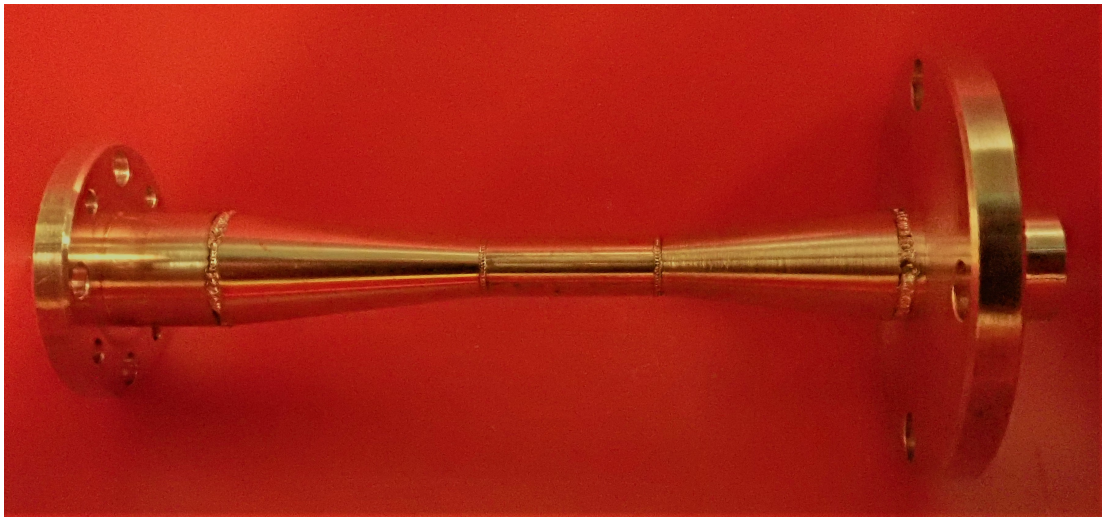

(a) Mode cleaner (see text)

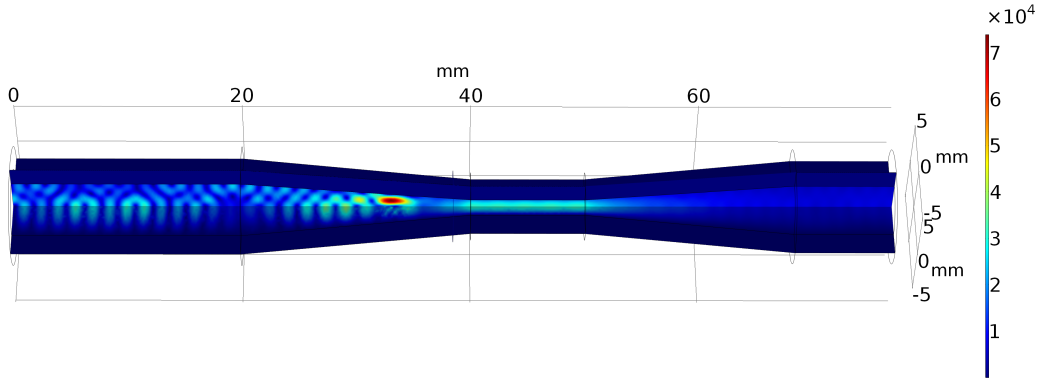

(b) TE11 mode

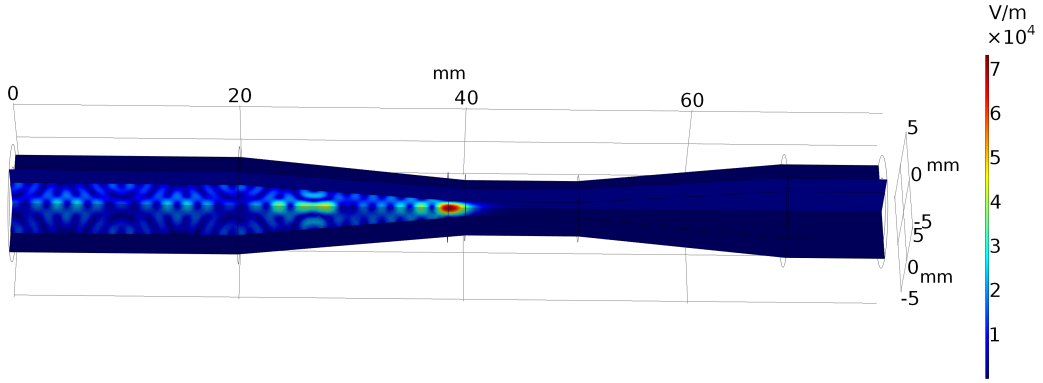

(c) TM01 mode

Figure 3.7: (a) Photo of the mode cleaner and 3D simulation of the time averaged electric field amplitude in the mode cleaner at a frequency of 113 GHz with a TE11 mode (b) and a TM01 mode (c) as input signal. The microwaves enter from the left with an input power of 1 W.

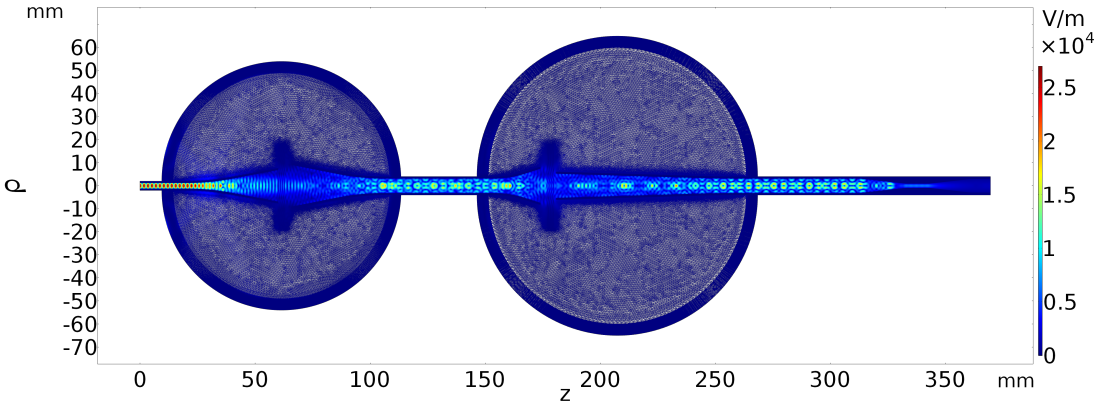

(a) Overview

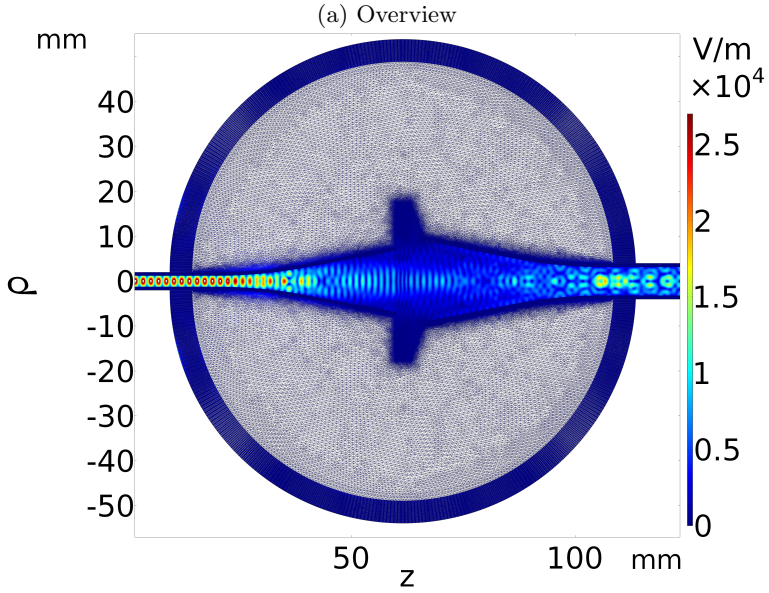

(b) Zoom on horn 1 and 2

Figure 3.8: Electric field norm in the microwave injection at a frequency of 112 GHz with an input power of 1 W. In (a), an overview over the simulation is given. The microwaves enter from the left. And travel along the z-axis, ρ denotes the position in the radial direction of polarization. Horn 1 and 2 are contained in the first circle, horn 3 and 4 in the second. Only the TE11 mode passes through the mode cleaner at the right end. (b) shows a zoom on the region containing the horns 1 and 2.

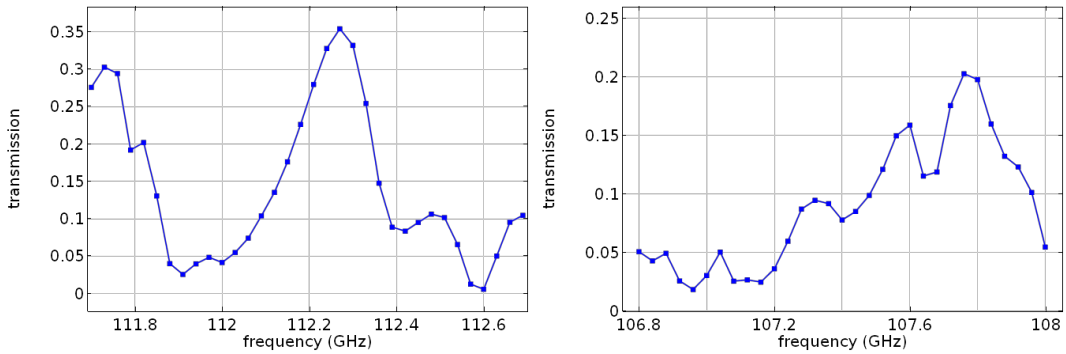

(a) Precision Trap

(b) Analysis Trap

Figure 3.9: Detailed scan of the power transmission at the expected larmor frequency (a) in the Precision Trap and (b) in the Analyis Trap.

4 The ISOLTRAP experiment

The ISOLTRAP experiment is located at the radioactive ion beam facility ISOLDE (Isotope Separation On-Line Device) at the European Organization for Nuclear Research CERN (French: Conseil Européen pour la Recherche Nucléaire) in Geneva, Switzerland. Its aim is to measure the mass of radioactive isotopes with high precision. In this chapter, first the ISOLDE facility is described, then an overview over the ISOLTRAP setup is given. Finally, the goals and steps of the work done for this thesis at ISOLTRAP are defined.

4.1 The ISOLDE facility

To produce radioactive ion beams, the ISOLDE facility [54–56] is supplied with a proton beam delivered by CERN's accelerator system. A bunched proton beam is produced at the Linear accelerator 2 (LINAC 2) and accelerated to an energy of 50 MeV. Then, the protons are transferred to the Proton Synchrotron Booster (BOOSTER), which accelerates them to an energy of 1.4 GeV. From their, the proton bunches are either transported to the Proton Synchrotron (PS) for further acceleration or the ISOLDE facility.
ISOLDE hosts experiments for nuclear masses, nuclear spectroscopy, solid state physics, medical physics and surface studies. An overview over the ISOLDE hall and the experiments located in there is given in Fig. 4.1. The proton beam is guided to one of the two target stations connected to the magnetic separators, the High-Resolution Separator (HRS) with a designed mass resolving power of up to $m/\Delta m \approx 15000$ [54] and the General-Purpose Separator (GPS) with a designed mass resolving power of $m/\Delta m \approx 2400$ [54]. Here, the protons hit a hot target made of heavy nuclei, e.g. UC_x. By fission, spallation or fragmentation, the target nuclei are converted into lighter nuclei and diffuse to an ion source. Here, the atoms are ionised via surface ionisation, in a plasma source or via resonant laser ionisation (RILIS [57, 58]) and accelerated to an energy of 30 keV to 60 keV and delivered to the experiments.

4.2 The ISOLTRAP experiment

At the ISOLTRAP experiment, high-precision mass measurements are performed for more than 30 years [31]. They are needed among others to validate nuclear models, for tests of the Standard Model of Particle Physics, for measurements of the neutrino masses and for nuclear astrophysics [12]. The mass measurements are performed using two Penning traps (see chapter 2.2) and multi-reflection time-of-flight mass spectrometer (MR-ToF MS, see chapter 2.3).

4.3 The ISOLTRAP setup

A schematic overview over the ISOLTRAP setup is depicted in Fig. 4.2. The setup consists of a horizontal section used for beam preparation in a radiofrequency quadrupole trap (RFQ)

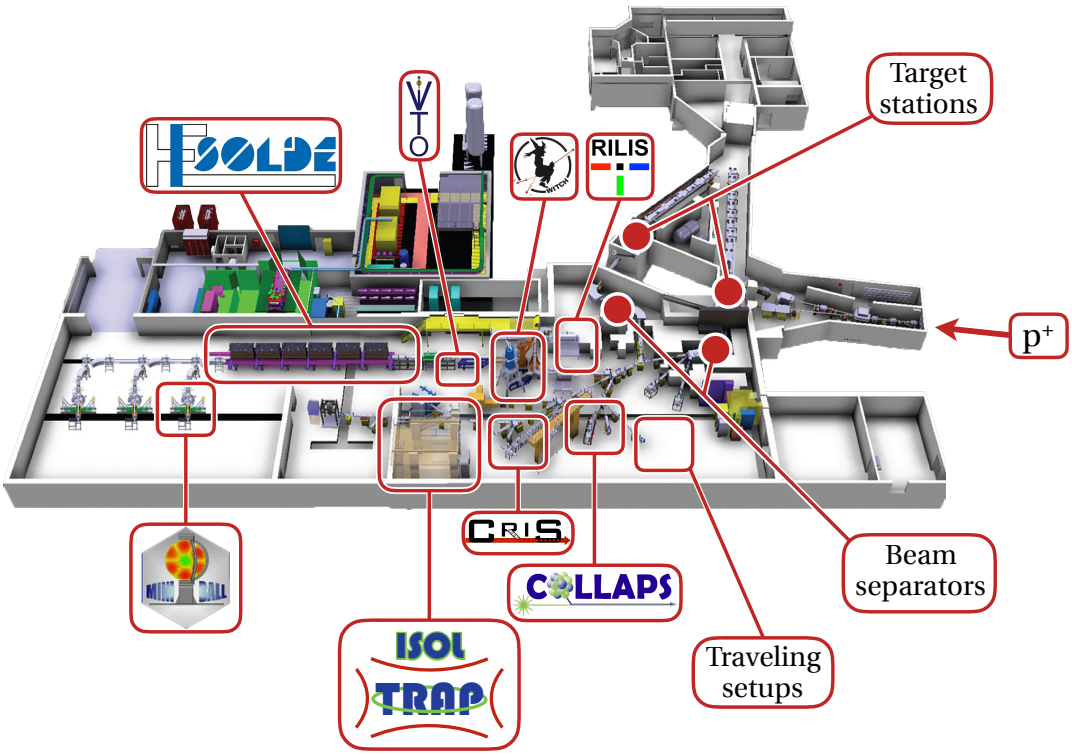

Figure 4.1: Drawing of the ISOLDE experimental hall including the permanently installed experiments. The two beam separators are High-Resolution Separator (HRS, left) and the General-Purpose Separator (GPS, right). Figure courtesy of Jonas Karthein.

and high-precision mass measurements with a Multi-Reflection Time-of-Flight Mass Spectrometer/Separator (MR-ToF MS) [59], and a vertical section containing two Penning traps. This work focusses on the components of the horizontal section emphasized in Fig. 4.2. Components of the ISOLTRAP setup used within this thesis are described in the following.

4.3.1 The reference ion source

Radioactive nuclei are delivered from the ISOLDE target to the ISOLTRAP experiment by a beamline. To allow for calibrations with well-known off-line masses as well as for systematic studies and the optimization of the settings, an off-line alkali ion source is installed upstream of the RFQ cooler and buncher (see subsection 4.3.2). It consists of a heated pellet and uses surface ionisation to ionise alkali metals. The source provides mainly $^{133}Cs^{+}$ ions, in addition also the two rubidium isotopes $^{85,87}Rb^{+}$ and smaller amounts of $^{39}K^{+}$. Also traces of other ions as $^{41}K^{+}$ are provided, but not used for the measurements performed in this work. The source produces a continuous beam of ions, which is bent by a kicker bender into the on-line beamline and transported to the RFQ cooler and buncher. Both, the reference ion source and the RFQ are placed inside a high-voltage cage, which can be ramped up to 60 kV. In this work, if not stated differently, it was ramped to a voltage of 49.985 V.

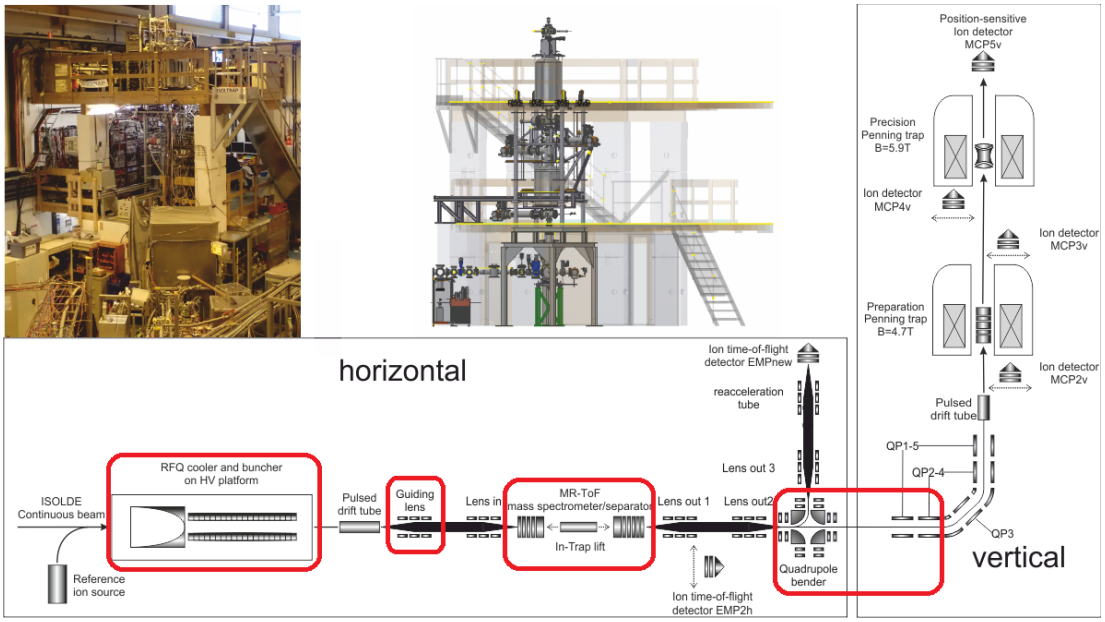

Figure 4.2: The Isoltrap experiment: Top left: Photo, top center: 3D drawing. The wooden platform and the housing were made transparent for better visibility of the experimental components. Bottom and right: Schematic of the ISOLTRAP setup. The marked components will be addressed in the following chapters. From left to right: The ISOLTRAP RFQ cooler and buncher (chapter 5), the Georg 1 einzel lens (chapter 6), the ISOLTRAP MR-ToF MS (chapter 7) and the quadrupole bender and the quadrupole lenses 1 and 2 (chapter 8).

4.3.2 The RFQ cooler and buncher

The ISOLTRAP cooler and buncher [21] is a linear radiofrequency quadrupole trap as described in chapter 2.1.2. The four linear rods are subdivided into 26 isolated segments. On each segment, a different DC potential is applied to create a linear potential distribution with a minimum inside segment 25, which is also called B-trap. A frequency generator creates a sinusoidal radio-frequency signal with a frequency of 1.45 MHz, which is transmitted and amplified by five coupling boxes containing RF resonance circuits. For extraction, the potential of the electrodes 23 and 24 is switched from 10 V to 100 V and electrode 26 from 45 V to −100 V. The ions are accelerated on the resulting potential ramp, focussed by an einzel lens and a set of horizontal and vertical steerers and fly into a pulsed drift tube, called HV pulse down, which is on a potential of typically 3.2 kV less then the cage containing the RFQ cooler and buncher. When the ions are in the centre of this tube, it is switched down to ground potential. Therefore, the ions leave the tube with a total energy of 3.2 kV and the initial energy spread is conserved. Then, the ions are transported to the ISOLTRAP multi-reflection time-of-flight mass spectrometer.

4.3.3 The Multi-Reflection Time-of-Flight mass spectrometer (MR-ToF MS)

The ISOLTRAP MR-ToF MS (theory see chapter 2.3) as drawn in Fig. 4.4 is used either for mass time-of-flight mass measurements. For a recent measurement of $^{58-63}$Cr with relative precisions of the measured masses on the order of 10^7 using one on-line and one off-line reference,

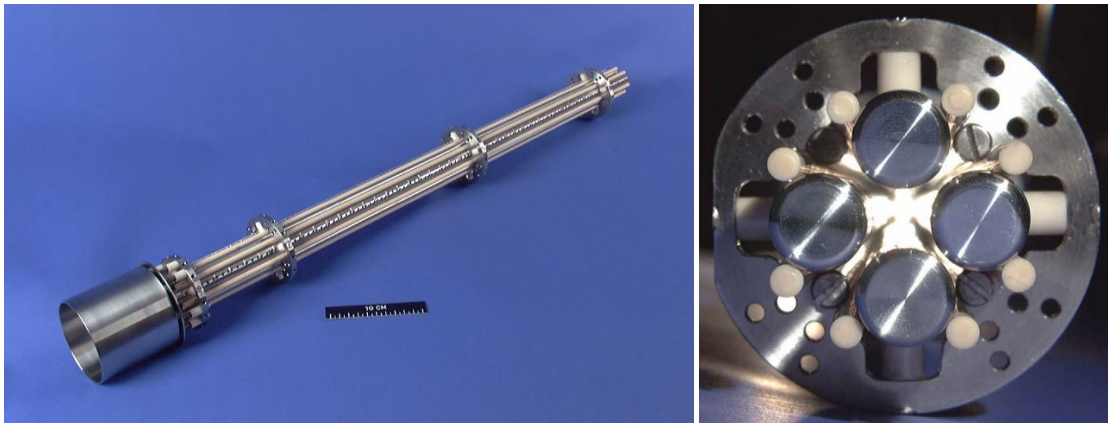

(a) The ISOLTRAP RFQ (b) Cross section

Figure 4.3: (a) the ISOLTRAP cooler and buncher. The cup-like deceleration electrode on the left focusses the incoming beam for the purpose of injection. In (b), a cross section of the rod structure is shown. The four 26-fold segmented electrode rods (diameter 18 mm, total length 881.5 mm) are supported by four outer support rods (small circles) and eight insulating ceramic rods. Everything is fixed on the mounting disks also visible in (a). The inner rod distance is given by $2r_0 = 12$ mm. For further details see [21].

Figure 4.4: Drawing of the ISOLTRAP MR-ToF MS. Modified from [37] The mirror electrodes M1 to M6 at both mirrors are on a symmetrical potential.

see [60]. The injection and tuning of the MR-ToF MS works with the in-trap-lift technique described in [40]: The kinetic energy of the ions is sufficiently high to fly over the first mirror into the central drift tube, which is on positive potential. When the ions are in the centre of the tube, it is switched to ground and therefore reduces the energy of the ions, so that they are reflected by the mirrors. For extraction, the potential of the drift tube is switched to its initial potential while the ions are inside it. The voltage of the drift tube defines the kinetic energy of the ions while trapping and therefore the turning point in the mirrors and the dispersion of the MR-ToF MS. The ideal point is found by scanning the voltage and minimizing the width of the time-of-flight peak of an arbitrary ion on the detector.

4.3.4 Einzel lenses

In the ISOLTRAP setup (see Fig. 4.2), several einzel lenses are used. The einzel lenses in the horizontal part are:

- one lens at the extraction of the RFQ cooler and buncher, to focus the diverging beam into the pulsed drift tube.
- the guiding lens and lens in to focus the diverging beam emerging from the pulsed drift tube and to refocus it into the MR-ToF MS. The guiding lens was replaced by a new one during this work. This is described in detail in chapter 6.
- lens out 1 and 2 to focus the diverging beam leaving the MR-ToF MS. With lens out 1, the beam is focus on the electron multiplier EMP2h, that can be moved in to act as a time-of-flight detector (see Fig. 4.2). Lens out 2 is used to focus the beam on the entry of the quadrupole bender.
- At each opening of the quadrupole bender one lens is used to focus the beam while bending it and to shield the fringe fields of the bending electrodes. This is discussed in more detail in chapter 8.
- Lens out 3 and the reacceleration tube are used the diverging beam emerging from the quadrupole bender on the electron multiplier EMPnew.

4.3.5 The Quadrupole Bender

The quadrupole bender (QPB) is an ion optical tool to bend ions by 90° to the left or to the right or to transmit them straight by switching bending electrodes. Therefore, it can be used to flexibly switch the destination of an ion beam without mechanical intervention. In the ISOLTRAP setup, as depicted in Fig. 4.2, it can be used to either transmit the ions emerging from the MR-ToF MS (in this case acting as mass separator) straight towards the vertical section with the Penning traps, or to bend them to the electron multiplier to use the MR-ToF MS as time-of-flight mass spectrometer. The now free opening of the quadrupole bender allows for further upgrades of the ISOLTRAP setup, for example by additional off-line ion sources. The quadrupole bender of the ISOLTRAP experiment was replaced recently. During this thesis, the ion optical properties of the new quadrupole bender were studied using simulations and first tests were done. This is described in chapter 8.

4.3.6 Ion detectors

In the ISOLTRAP experiment, several ion detectors are used, some of them for high-precision mass measurements and others for the optimization of the ion optics and the timings of switched electrodes. Most of the measurements presented in this work have been done with the removable electron multiplier EMP2h just behind the MR-ToF MS and Lens out. The electron multiplier EMPnew at the position of a formerly used laser ion source [61] was used to test the properties of the new quadrupole bender.

4.3.7 90-degree bender

The horizontal ion beam is brought into a vertical direction by two bending electrodes. To keep the beam focussed, five quadrupole lenses, denoted as QP1 to QP5 (see figure 4.2), are used with alternating polarity. The lenses QP1 and QP5 are on the same potential, as well as QP2 and QP4. During this work, a new support for the quadrupole lenses 1 and 2 was manufactured. This is described in chapter 8.3.

4.3.8 The two Penning traps

The ISOLTRAP experiment uses two Penning traps for high-precision mass measurements. The cylindrical preparation Penning trap [62] is used for beam cooling and purification via mass selective buffer gas cooling at a pressure of $p \approx 1 \times 10^{-4}$ mbar. Several ion bunches coming from the MR-ToF MS can be accumulated [63]. Then they can be transported with well defined properties to the precision Penning trap. The preparation Penning trap is located inside a 4.7 T superconducting magnet on the first floor of the ISOLTRAP trap tower. The hyperbolic precision Penning trap on the second floor of the trap tower is located inside a 5.9 T superconducting magnet. Here, mass measurements using the ToF-ICR [30, 31] and PI-ICR [32, 33] techniques are performed.

4.4 Goals and steps of this work

After many years of successful high-precision mass measurements using the ISOLTRAP MR-ToF MS using on-line references, further steps towards more exotic nuclei require experiments with an analysis based on off-line references. This brings several challenges with it that have been addressed during this work.

Contaminants in a time-of-flight spectrum used as on-line references are useful during a measurement campaign as well as in the subsequent data analysis in several ways. One major advantage is that they are affected by systematic drifts the same way as the ion of interest and are close to their mass. Consequently, they can be used for precise calibration and for the identification of other masses appearing in the spectrum. It is possible to correct for drifts afterwards by correcting the time-of-flight spectrum for the shifts simultaneously observed for the contaminant at significant count rate as described in [59]. Additionally, changes of the count rate of the contaminant are a clear hint that the ion optics suffer from an instability, which then could be corrected for. This is also possible during a measurement dedicated for the ion of interest and therefore is an important tool for on-line monitoring of the experiment. Both advantages are linked to a reliable and precise measurement of count rate and time-of-flight of the contaminant. Therefore, the count rate has to be adapted to a level, at which the time-of-flight detector is not saturated for the contaminant and at which no time-of-flight shifts due to space charge effects in the MR-ToF MS appear. This is done by changing the time, the continuous beam coming from the ISOLDE target is accumulated in the RFQ to form one bunch. This time is called beam gate. As long as the beam gate is much shorter than the lifetime of the ion of interest and as the entire measurement cycle, the ion count rate is proportional to the beam gate. Consequently, the number of accessible isotopes is in many cases not limited by the production rate, but by the abundance ratio with respect to the contaminant used as on-line reference.

To circumvent this problem, a change from on-line references to off-line references measured before and after the ion of interest has to be made. This applies directly to cases when no isobaric contaminant is available and opens the door for further beam separation, for example by a reinjection of ions, which were first separated with the MR-ToF MS and then trapped. Such a scheme is implemented already at the TRIUMF experiment [64]. Unfortunately, one has to go without the advantages of on-line references mentioned above. In this work, several needed steps to do so were addressed:

1. One systematic shift is related to the beam preparation in the RFQ cooler and buncher. Time-of-flight and count rate were observed to depend on the phase of the applied radio frequency field at the moment of extraction of the ion bunch. This effect was reproduced qualitatively in simulations and reduced experimentally by a modification of the timing pattern. Also a realistic ion sample for simulations was created and validated experimentally. These steps related to the beam preparation are described in chapter 5.

2. One known source of instabilities of the ion optical system at ISOLTRAP was the Einzel lens used to focus the decelerated ion beam coming from the pulsed drift tube between the ISOLTRAP buncher and the MR-ToF MS. A replacement was designed and manufactured and is now ready to be installed. This is described in chapter 6.

3. The MR-ToF MS was used to quantify the width of the energy distribution of a detected ion specie. This may help to identify inefficient cooling due to high numbers of contaminant ions in the buncher at the same time as the ion of interest and in the case of chemical reactions happening in the RFQ. Then, tests of the stability of mass measurements based on references before and after the ion of interest were performed. This sets a limit to the precision achievable with off-line references. These parts related to the MR-ToF MS are described in chapter 7.

4. The new electron multiplier (position see figure 4.2) has an improved time resolution and can deal with higher count rates. A new quadrupole bender was installed to allow an efficient ion transport to it. In addition, this will make it possible to switch faster between MR-ToF MS and Penning-trap mass measurements. Using simulations, working settings were found and it was demonstrated that the quadrupole bender is well inside the tolerances for a possible misalignment. This is presented in chapter 8.

5 Ion preparation in the ISOLTRAP RFQ

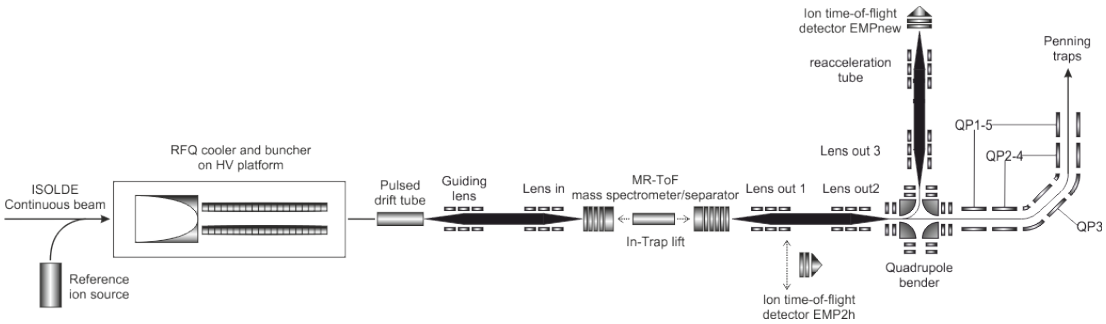

Figure 5.1: Schematic of the horizontal beamline of ISOLTRAP (detail of Fig 4.2).

The ISOLTRAP radio-frequency quadrupole cooler and buncher (RFQ) [21, 22], is used to cool the continuous ion beams coming from the ISOLDE target and ion source and from the alkali reference ion source and to emit ion bunches for time-of-flight mass measurements and beam purification in the ISOLTRAP MR-ToF MS. The clock for time-of-flight (ToF) measurements with the MR-ToF MS starts with the ejection pulse applied to the RFQ. Consequently, the RFQ can be considered an ion source, both for the actual experiment and in simulations of the beam optics downstream of it and for the simulation of ToF-spectra. The horizontal section of the ISOLTRAP experiment used for time-of-flight mass spectronomy and beam purification containing the RFQ is depicted schematically in Fig. 5.1.
A crucial condition for the reliability of simulations of ion trajectories is to have realistic initial conditions for the ion cloud when being extracted from the RFQ. A theoretical description of radiofrequency cooler and bunchers is given in chapter 2.1, a description of the design of the ISOLTRAP RFQ is given in section 4.3.2. In this chapter, it is first described, how such a realistic ion cloud was created. Then, the influence of the phase and amplitude of the applied radio-frequency field on the ion transmission and the time-of-flight measured with the MR-ToF MS are studied experimentally and modelled in simulations. Finally, an optimization protocol for the buncher preparation for time-of-flight mass measurements is outlined.

5.1 Initial ion distribution

For simulating the initial ion distribution emerging from the RFQ cooler-buncher, the last four segments of the electrode rods of the RFQ were used. As described in [22] and [21], the cooled and stored ions reach a thermal equilibrium with the surrounding buffer gas and are trapped in the minimum of the longitudinal electric field, which is located in the centre of segment 25 (also called B-trap) of the ISOLTRAP cooler and buncher. The DC voltages applied on these segments for trapping and extraction are listed in Tab. 5.1.

In this section, it is described how a realistic ion cloud is generated. Then, simulation results will be compared to theoretical expectations and experimental data.

Table 5.1: Trapping and ejection voltage of the four last segments of the ISOLTRAP RFQ

segment	trapping voltage (V)	ejection voltage (V)
23 & 24	10	100
25	0	0
26	45	-100

5.1.1 Generation of a realistic initial ion cloud

For the simulations, the electric field was assumed to be completely defined by the electrodes in Tab. 5.1 and the components downstream of the RFQ.
To simulate the initial ion distribution, first, the potential along the x-axis (pointing downstream) in trapping mode is deduced from SIMION and fitted around its minimum in segment 25 with a quadratic potential:

$$V(x) = V_0 + k_x \cdot (x - x_0)^2. \tag{5.1}$$

Here, x_0 is the axial position of the potential minimum, where the ions are trapped and V_0 is the corresponding DC potential. This can be done since the pseudopotential created by the radio frequency field vanishes on the symmetry axis. The fit returned $k_x = 0.231\,75\,\mathrm{V\,mm^{-2}}$. The radial pseudopotential is given by equation (2.18):

$$V(y,z) = \left(\frac{e \cdot V_{RF}^2}{m \cdot r_0^4 \cdot \omega^2} - \frac{k_x}{2}\right) \cdot (y^2 + z^2) =: k_{y,z} \cdot (y^2 + z^2). \tag{5.2}$$

Here, V_{RF} is the RF amplitude applied to the electrode rods of the buncher, m is the ion mass, r_0 half the distance between opposite electrode rods and $\omega = 2\pi\nu_{RF}$ the RF frequency. The effective overall potential in equation (2.19) is given by

$$V(x,y,z) = V_0 + k_x \cdot (x - x_0^2) + k_{y,z} \cdot (y^2 + z^2). \tag{5.3}$$

The second term in the brackets $\frac{k_x}{2}$, being the radial component of the static quadrupole field, is about a factor 5-10 times smaller than the first term $\frac{e \cdot V_{RF}^2}{m \cdot r_0^4 \cdot \omega^2}$ for the experimental values with maximal transmission. Therefore, it has only a small influence on the initial ion distribution, but makes considerations of scalings with mass and RF amplitude more difficult. Thus for experimental settings the approximation

$$k_{y,z} \approx \frac{e \cdot V_{RF}^2}{m \cdot r_0^4 \cdot \omega^2} \tag{5.4}$$

was used. The effective potential can be split into quadratic potentials in each dimension $a \in \{x, y, z\}$, so the motion is given by three independent harmonic oscillations. For each of them, the energy and oscillation phase is randomly generated with the Boltzmann distribution

$$P(E_a) \propto e^{-\frac{E_a}{k_B \cdot T}} \tag{5.5}$$

for a temperature of $T = 300\,\mathrm{K}$. k_B denotes the Boltzmann constant. Here and in the following, the ROOT TRandom2 pseudo random number generator [65] was used. Three random oscillation phases $\phi_{x,y,z} \in [0, 2\pi]$ of the motion in the pseudopotential were assigned to each

ion. The maximal amplitude in the $a \in \{x, y, z\}$ dimension of the ion oscillation in the potential is given by

$$a_{max} = \sqrt{\frac{E_a}{e \cdot k_a}} \tag{5.6}$$

and the maximal velocity is given by

$$v_{a,max} = \sqrt{2 \cdot E_a / m} \tag{5.7}$$

The initial position and velocity of the ion is then given by

$$a = a_{max} \cdot \cos(\phi_a) \tag{5.8}$$

$$v_a = -v_{a,max} \cdot \sin(\phi_a) \tag{5.9}$$

By this approach, a test bunch containing 1000 ions was generated. It represents an ion distribution at the RF phase $\xi = 0$. The spatial and velocity spread of such a sample of ^{39}K ions is depicted in Fig. 5.2. The distribution is similar to Fig. 2.4b, which were generated in a simulation of the buffer gas cooling with realistic scattering potentials in [21]. These ions are used as input for a simulation of the ion trajectories using SIMION [66]. Each simulation starts with a storage time $t_{store} \approx 30\,\mu s$ to account for consequences of the RF-phase and to take count for imperfections of the pseudopotential approximation. The simulation also starts with an RF-phase of $\xi = 0$, so that the storage time defines the phase during extraction.

To adapt to other ion masses m, RF frequencies $\omega = 2\pi\nu_{RF}$ and amplitudes V_{RF}, some transformations could be applied to the ion properties using equations (5.4) and (5.1):

- x is invariant since the longitudinal potential in equation (5.1) is mass independent.
- $v_x \propto m^{-1/2}$
- $y, z \propto k_r^{-1/2} \propto V_{RF}^{-1} \cdot m^{1/2} \cdot \omega$
- $v_{y,z} \propto m^{-1/2}$

5.1.2 Simulations and experimental values

To validate, that the simulations indeed return reasonable results, it was first checked, that they reproduce theoretical expectations. For this purpose the predicted ion transmission to the electron multiplier EMP2h right after the MR-ToF MS (see Fig. 4.2) was compared to experimental data.

Comparison to theoretical expectations

For different ion masses, the dependence of the transmission on the value of $q = \frac{4eV_{RF}}{mr_0^2\omega^2}$ equation (eqrefeq:defq was simulated. For this simulation, the RF signal applied to the electrode rods $V_{electrode\pm}(t)$ started with phase $\xi = 0$ at time $t = 0$ of the simulation and was kept on until the ejected ions were in the centre of the pulsed drift tube:

$$V_{electrode\pm}(t) = \pm V_{RF} \cdot \sin(\omega t). \tag{5.10}$$

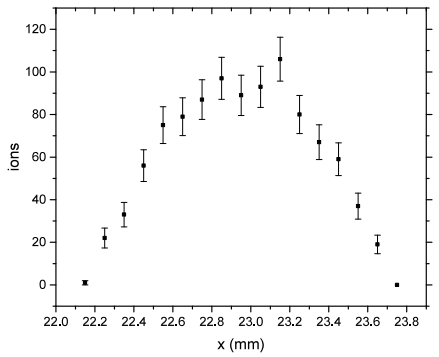

(a) Axial ion distribution

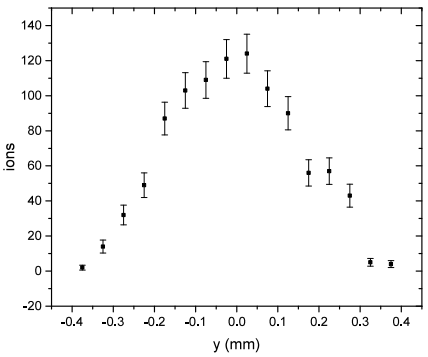

(b) Transversal ion distribution

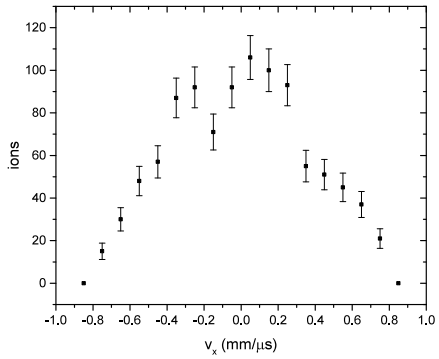

(c) Axial velocity distribution

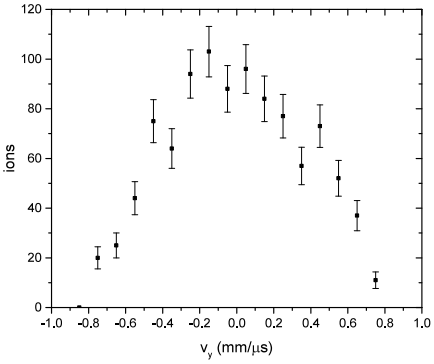

(d) Transversal velocity distribution

Figure 5.2: Initial ion distribution for ions with a mass of 39 u for an RF amplitude of 240 V and an RF frequency of $\nu_{RF} = 1.45$ MHz. This compares well to the result of a Monte Carlo simulation using realistic scattering cross sections depicted in Fig. 2.4b.

By increasing the storage time t_{store} in steps of $\delta t_{store} = \frac{2\pi}{10\omega}$ over four RF periods, the RF phase at the moment of extraction was scanned. The results are shown in Fig. 5.3a. The following conclusions can be drawn:

1. The transmission curve depending on q (from 0.2 to 1.0 in steps of 0.1) is very similar for each mass.
2. Both cut-off voltages V_{min} (Eq. (2.20))and V_{max} (Eq. (2.22)) where observed.
3. As expected from Eq. (2.21), the lower q cut-off depicted in Fig. 5.3b scales with the inverse square root of the mass. While Eq. (2.21) predicts $q_{min} = \frac{3.55}{\sqrt{m}}$, the fit returns $q_{min} = \frac{3.12 \pm 0.04}{\sqrt{m}}$, where the mass m is given in atomic mass units. Taking into account that the pseudopotential is only an approximation and that the longitudinal potential is not perfectly harmonic, the values agree very well.
4. The upper cut-off is given by the stability condition $q \leq 0.908$. This is approximately reproduced. While for $q = 0.9$, the transmission has already strongly decreased, it is zero for all simulated masses at $q = 1$ except for $m = 40\,\mathrm{u}$, where a small transmission of 0.5 % was simulated. Probably, this is due to the finite simulation time.
5. The bigger the mass, the higher is the transmission. This may be due to the mass dependent focus of the einzel lenses, optimized for ^{133}Cs(see Fig. (5.1).

The transmission was strongly dependent of them RF phase. Depending on the simulated ion mass, it was between 13 % and 40 % of the phase averaged transmission. Thus, to make a comparison between different masses and q values possible, the phase averaged transmission was plotted in Fig. 5.3. It can be summarized, that the results of simulations reproduce the theoretical expectations on the transmission described above, but the RF-phase dependence has to be studied in more detail. For beam optimizations $q = 0.7$ and a mass of $m = 129\,\mathrm{u}$ was chosen in order to have good statistics with only 1000 simulated ion trajectories.

Comparison to real data

In order to compare the settings on the real ISOLTRAP cooler and buncher with the simulations, one has to estimate the real RF amplitude. On the set-up, it is possible to set the amplitude of an RF signal coming from a frequency generator, however this signal is amplified by a resonance circuit by an unknown amplification factor F. Direct measurements of the amplitude ratio of input and output signal of the coupling boxes would have been time-consuming because one has to account for the capacitive coupling between neighbouring buncher segments. One can also estimate this factor using stored ions as probe by measuring the upper and lower cut-off voltages (V_{min} from Eq. (2.20) and V_{max} from Eq. (2.22)). This was done with a measurement for ^{39}K. The voltage set on the RF generator was scanned in the range from 0.05 V to 0.3 V in steps of 0.01 V with the RF signal continuously applied. The count rate was recorded and is compared with simulations in Fig. 5.4. To estimate the amplification factor $F = V/V_{set}$, the two edges of the transmission range were considered.
The upper cut-off is given by Eq. (2.22). It appeared at a set voltage of $V_{set} = 0.23(1)\,\mathrm{V}$. Taking into account the frequency of $\nu_{RF} = 1.45\,\mathrm{MHz}$, the true RF amplitude felt be the ions is

$$V_0 = \frac{m r_0^2 \cdot (2\pi\nu_{RF})^2}{4e} * q_{max} \approx 274\,\mathrm{V} \tag{5.11}$$

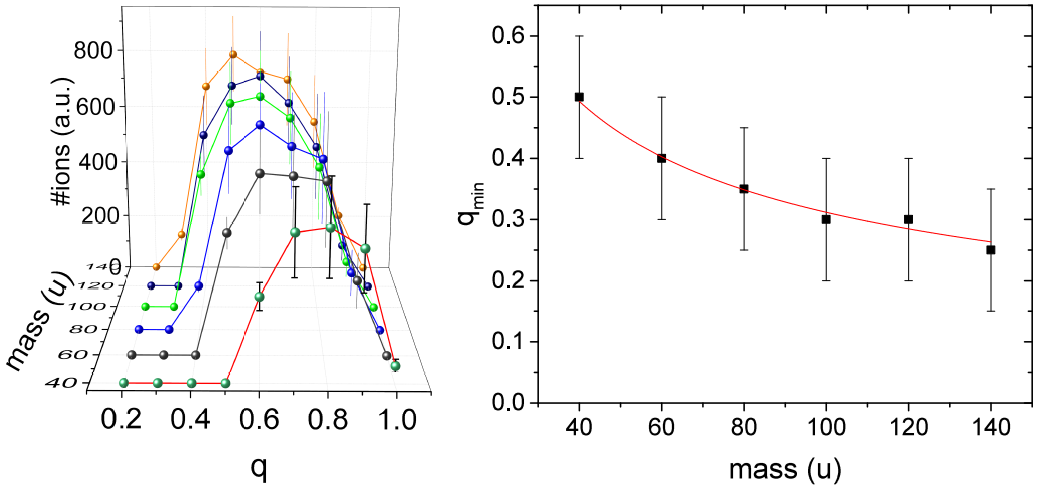

(a) Simulated transmission

(b) Simulated lower cut-off

Figure 5.3: (a) Ions transmitted from the buncher to the electron multiplier EMPnew (see Fig. 5.1) depending on the mass and the working point q. The RF phase at the moment of extraction was scanned with a step size of $\Delta\xi = 2\pi/10$ over four RF periods. For each phase, a bunch of 1000 ions generated as described in section 5.1.1 was simulated. The plotted z-value is the number of detected ions averaged over all phases. The error bars are the corresponding standard deviation. From this simulation, the lower cut-off q_{min} could be deduced with the precision of one simulation step $\Delta q = 0.1$. The result is plotted in (b) depending on the ion mass and fitted with the function $q_{min}(m) = A/\sqrt{m}$.

implying an amplification factor of the resonance system of

$$F = \frac{V_0}{V_{set}} = \frac{278\,\mathrm{V}}{0.23(1)\,\mathrm{V}} = 1192 \pm 52. \tag{5.12}$$

The lower cut-off at a set RF amplitude of 0.07(1) V and equation (2.20) imply an amplification factor of

$$F = \frac{V_{0,min}}{V_{min,set}} = \frac{71\,\mathrm{V}}{0.07(1)\,\mathrm{V}} = 1014 \pm 145 \tag{5.13}$$

Both values agree with each other. As expected from Fig. 2.2b and the disregard of the longitudinal potential for the derivation of V_{max}, the first value is the higher one. The weighted mean of both amplification factors is given by $F = 1172 \pm 49$. Maximal transmission was achieved for a voltage set to $V_{set} = 0.14(2)$ V corresponding to $q = 0.54 \pm 0.08$. The red line in Fig 5.4 is the result of a simulation with the RF amplitude scaled with $F = 1172$. The edges are in good agreement with the measured data, but the shape is more rectangular. Probably this is due to the fact, that for the simulation the capture efficiency of the RFQ was assumed to be constant for all RF amplitudes and due to ion loss by collisions with the buffer gas.

5.2 RF phase dependence

At the ISOLTRAP experiment it had been already observed that the transmission as well as the mean time-of-flight of ions from the RFQ to the electron multiplier EMP2h (see Fig. 5.1 oscillates periodically, when the phase of the RF in the buncher at the moment of extraction is varied linearly. In the past, measurements were taken with the RF continuously on with the

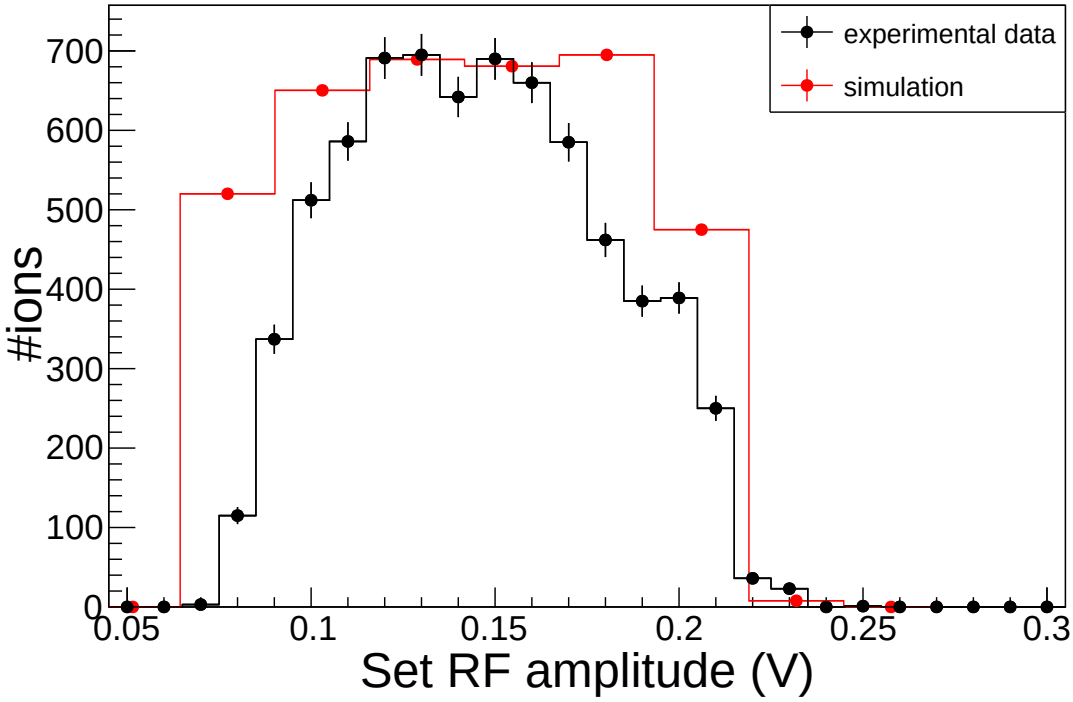

Figure 5.4: Measurement of the transmission of ^{39}K to the electrode multiplier EMP2h (see Fig. (5.1))with 100 revolutions inside the MR-ToF MS as a function of the RF amplitude set on the RF generator in the control software. The red line is the result of a simulation assuming equal capture efficiency for all RF amplitudes and an amplifaction factor of the RF coupling boxes of $F = 1172$ (see text). It was scaled with a factor 0.0283 to have the same maximum as the measured data.

purpose to average out these oscillations. The RF phase changes from ejection to ejection by

$$\Delta\xi = [t_{cycle} \cdot \omega] \mod 2\pi. \tag{5.14}$$

Here, t_{cycle} denotes the time needed for an entire measurement cycle and $\omega = 2\pi\nu_{RF}$ is the buncher RF frequency. Since $\Delta\xi$ is in general not a simple rational number times 2π, this corresponds to averaging over random phases, which are weighted by the number of detected ions for each phase.
In this section it is described how this can lead to shifts in the determination of the mean time-of-flight and asymmetric peak shapes in MR-ToF mass spectroscopy. Then, experimental studies and simulations are presented.

5.2.1 Derivation of the RF phase dependent shift

To demonstrate, that a periodic oscillation of the ion time-of-flight and ion count rate with respect to a parameter linearly scanned from ejection to ejection (here the RF phase) can lead to a shift of the measured mean time-of-flight and a distortion of the line shape of the corresponding ToF spectrum, the simple case of sinusoidal oscillations is considered. If transmission probability from the source (here the RFQ) to the detector (here the electron multiplier EMP2h) depending on the RFQ phase ξ being given by

$$P(\xi) = \frac{1}{2\pi}(1 + A \cdot \sin(\xi)) \tag{5.15}$$

and the ToF depending on ξ being given

$$ToF(\xi) = T_0 + B \cdot \sin(\xi + \delta) \tag{5.16}$$

with a phase offset $\delta \in [-\pi; \pi]$ relative to the count rate oscillation, then the measured mean time-of-flight is given by

$$< ToF > = \int_0^{2\pi} ToF(\xi) \cdot P(\xi) d\xi \tag{5.17}$$

$$= T_0 + \frac{A \cdot B}{2} \cos(\delta). \tag{5.18}$$

Therefore, the measured mean ToF $< ToF >$ is shifted away from the phase averaged mean T_0 by

$$\Delta ToF = < ToF > - T_0 = \frac{A \cdot B}{2} \cos(\delta). \tag{5.19}$$

If $\delta \neq \pm\pi/2$ the arithmetic mean of the ToF peak shifts, but the peak shape also gets asymmetric. A higher count rate for a RF-phase with a lower mean time-of-flight creates a peak with a tail towards higher times-of-flight. The distortion of a formerly Gaussian shaped peak with count rate and mean oscillating as in equations (5.15) and (5.16) is shown for a set of relative count rate oscillation A and phases δ in Fig. 5.5.This is a problem in analysing mass spectra, especially if two peaks are not well separated. In such a situation, their positions can be found by a fit, but for an accurate analysis, the peak shape has to be known a priori. Equation (5.19) only holds for the simple model with equations (5.15) and (5.16), but an analogous argumentation can be given for other periodic functions. However, this model is a good approximation for

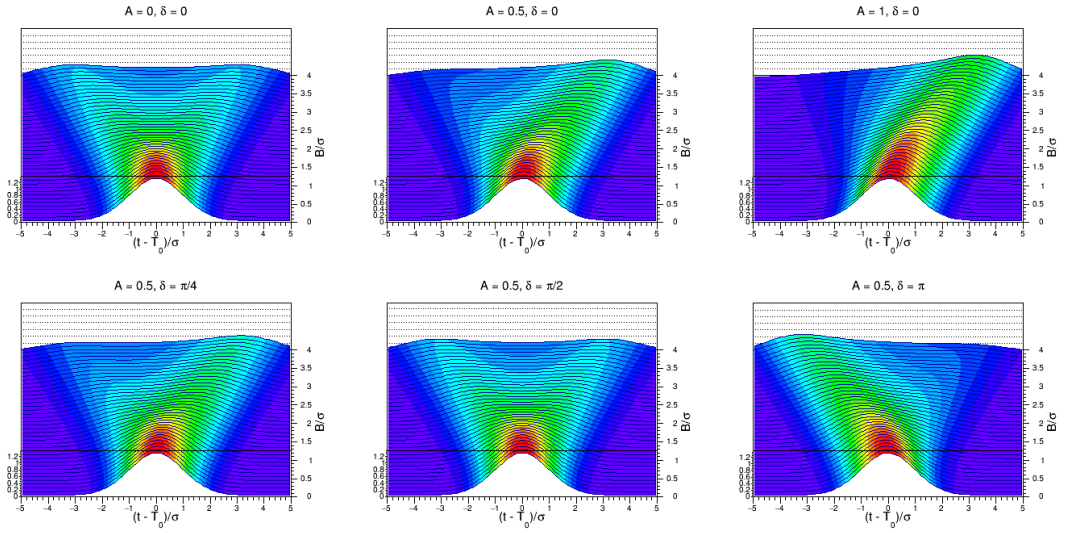

Figure 5.5: Simulated time-of-flight peaks for a set of phases δ and relative count rate oscillation amplitudes A depending on the time-of-flight oscillation amplitude given in units of the standard deviation of the peak σ. A Gaussian shaped peak is distorted by time-of-flight and count rate oscillations (see equations (5.16) and (5.15)). From front to back, the time-of-flight oscillation amplitude B in units of the standard deviation increases. For $B = 0$, all peaks are perfectly Gaussian. As B increases, the peaks get broader and are shifted. The color coding is redundant with the z-axis and displays the ion count rate normalized to the entire number of counts. Depending on δ, the shift can be either to a higher or to a lower time-of-flight. Also the formation of a double-peak is possible.

the dependence of count rate and time-of-flight on the RF phase at the moment of extraction. In the following sections 5.2.2 and sec:simulationsRFphase, this is shown with experimental data and followed by simulations. Since all three parameters A, B and δ might dependent on the ion mass m as well as on buncher settings, they aim to understand and reduce the RF phase dependence of the measured time-of-flight.

5.2.2 Experimental studies of the RF phase dependence

The dependence of the time-of-flight on the RF phase at the moment of the ejection from the buncher was also studied experimentally. In the following, it is described how scans of the RF phase where implemented and analysed. The results are presented for different numbers of revolutions inside the MR-ToF MS, for different ion masses and for different RF amplitudes.

RF gated mode

To study the RF phase dependence experimentally, the RF frequency generator was switched from continuous mode (continuous output of RF signal) to a gated burst mode. The RF output is switched on with phase $\xi = 0$ at a defined point of time during the timing pattern of the ISOLTRAP set-up by a trigger signal. Therefore, the RF phase at the moment of extraction can be defined. In the past, the RF was switched off 2 µs after the extraction. At this time, the ions have already left the ISOLTRAP cooler and buncher. Because this lead to a very strong dependence of the TOF on the phase of the RF at extraction, the RF was in the end always used

in continuous mode, in order to average all phases (although, as shown before, the averaging was still biased). The direct impact on the measured time-of-flight of going to gated mode is shown in Fig. 5.6. In RF continuous mode, oscillations of the time-of-flight are clearly visible. They disappear when going to RF gated mode, but slower drifts remain. The RF phase can be

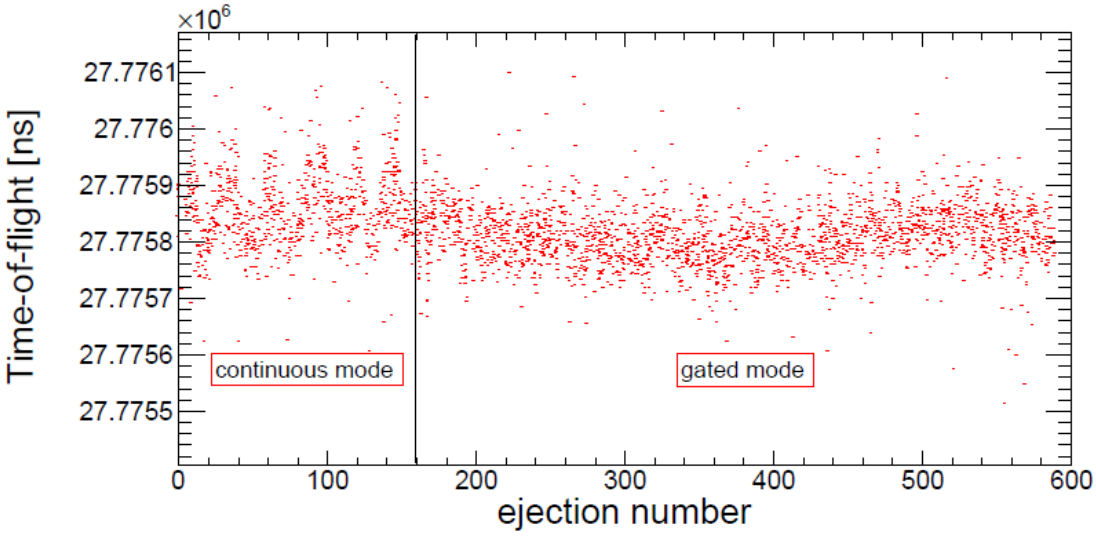

Figure 5.6: Effect of going from RF continuous mode to RF gated mode on the time-of-flight of ^{133}Cs from the RFQ to the electron multiplier EMP2h (see Fig. 5.1).

varied by varying the time the ions are cooled inside the RFQ after the end of the accumulation period (this time is called buncher cooling time). During this time, the RF is on.

Analysis code

To analyse the scans of the RF phase, a C++ analysis code was written in ROOT [65]. The input is a 2D histogram (a TH2D) in a .root file containing the number of counts with the time-of-flight in the x-dimension and an index for the value of a scanned parameter, here the RF phase, in the y-dimension. In the following, it is called the ToF-matrix. The analysis code works as follows:

1. A fit of the ToF-projection with a Gaussian line-shape. The data range for the further analysis is restricted to the range $[\mu - 4 \cdot \sigma; \mu + 4 \cdot \sigma]$ with the mean μ and the standard deviation σ from the Gaussian fit.

2. The y-projection, i.e. the number of counts as a function of the RF-phase was fitted with the function

$$P(y) = P_0 + A \cdot \sin(2\pi\nu_{RF} t_{step} \cdot y + \delta_{rate}), \tag{5.20}$$

   where $\nu_{RF} = 1.45\,\text{MHz}$ is the RF frequency and t_{step} is the step size between consecutive buncher cooling times in the scan, y is the index of the scanned buncher cooling time value and δ_{rate} is a phase off-set of the fitted oscillation. This formula corresponds to Eq. (5.15).

3. Similarly to Eq. (5.16), the mean time-of-flight depending on the scan index y is given by

$$ToF(y) = T_0 + B \cdot \sin(2\pi\nu_{RF} t_{step} \cdot y + \delta_{ToF}). \tag{5.21}$$

A maximum likelihood (MLL) fit of the ToF matrix is performed with the 2D function (TF2)

$$f(t, y) = \frac{1}{\sqrt{2\pi\sigma^2}} \cdot P(y) \cdot \exp\left(-\frac{(t - ToF(y))^2}{2\sigma^2}\right). \tag{5.22}$$

In the time-of-flight domain, this is a Gaussian with a mean which oscillates when changing the scan value y. The normalization of this peak is fixed by the fit of the count rate, performed in step 2. The standard deviation was assumed to be independent of the RF phase. This was observed to be not true, but was chosen to make the fit easier.

4. To illustrate the impact of the ToF oscillation, the entries of the ToF matrix for each scan value y are shifted by the the opposite of its ToF oscillation amplitude. Then, a ToF projection of this corrected spectrum is taken and fitted with a Gaussian. This Gaussian can be compared to a fit of the not corrected ToF spectrum.

For visualization, three histograms are plotted in one column: From top to bottom: The ToF-matrix, the count rate and the time-of-flight spectrum, together with the results of the fits described above. For more detail, see Tab. 5.2. In this configuration, the relative phase

Table 5.2: Layout of the RF phase scan analysis plots

Row 1	A transposed histogram of the ToF-matrix (scan index in x-dimension, ToF in y-dimension) together with a curve indicating the oscillating mean time-of-flight from a fit with Eq. (5.22).
Row 2	The count rate fitted with Eq. (5.20).
Row 3	The time-of-flight spectrum (the ToF projection of the ToF-matrix) together with a Gaussian fit (red) and a fit which was applied to the corrected ToF spectrum (green).

between count rate and ToF oscillation

$$\delta = \delta_{ToF} - \delta_{rate} \tag{5.23}$$

can be easily observed. A comparison of three such columns for different experimental settings is shown in the figures 5.7, 5.8, 5.9 and 5.13.

Dependence on number of revolutions in MR-ToF MS

In order to exclude, that the RF phase dependence is correlated with MR-ToF MS, the buncher cooling time and therefore the RF phase at the moment of extraction was scanned with 2, 100 and 1000 revolutions in the MR-ToF MS for ^{133}Cs. The result are presented in Fig. 5.7. The count rate was constant, but the time-of-flight is well modelled with a sinusoidal oscillation. The period of the oscillation is in perfect agreement with the number of steps during which the RF phase is scanned over one RF period. The oscillation amplitude is independent of the revolution number. This shows, that the oscillation is not created inside the MR-ToF MS, but inside the buncher or on the trajectories from the buncher to the MR-ToF MS and from the MR-ToF MS to the detector.

Mass dependence

The RF phase dependence was studied for the ion species ^{39}K, ^{85}Rb and ^{133}Cs (here and in the following, all ions are singly charged), which where delivered by the alkali ion source described

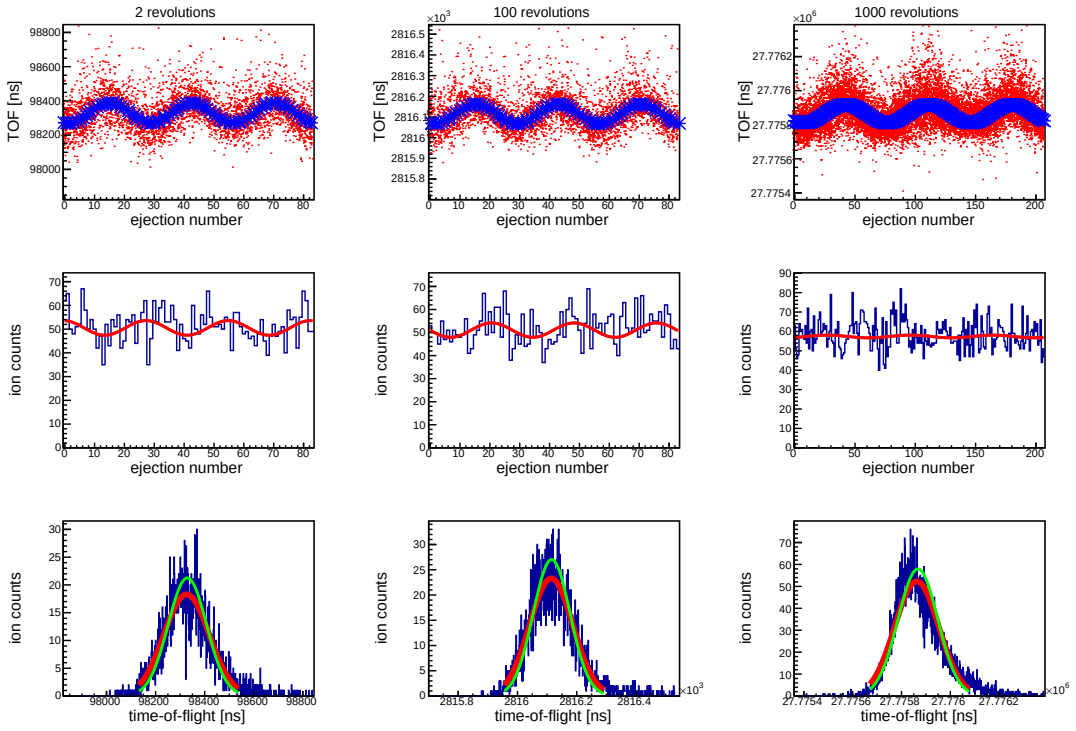

Figure 5.7: Scan of the buncher cooling time over 3 RF periods for ^{133}Cs for 2, 100 and 1000 revolutions in the MR-ToF MS. For the scan with 1000 revolutions, the scan step size of the buncher cooling time was 10 ns, for 2 and 100 revolutions, it was 25 ns. Description see Tab. 5.2.

in section 4.3.1. They are compared in Fig. 5.8. The count rate is affected quite differently for the three species. For ^{133}Cs, it is independent of the RF phase, for ^{85}Rb, there is a small dependence and for ^{39}K, there are narrow but very strong peaks of the count rate, that appear periodically with the RF period, but cannot be handled with the sinusoidal approximation in equation (5.15). Nevertheless, the most asymmetric peak is the one for ^{85}Rb. This is caused by the different phase relation δ between count rate and ToF oscillation.

RF amplitude dependence

Since the oscillation is caused by the RF amplitude, it was investigated how the oscillations are affected by the RF amplitude. Three of these measurements with ^{85}Rb are presented in Fig. 5.9. A bigger RF amplitude yields a bigger ToF oscillation amplitude. On the right, with an amplitude set to 0.3 V a clear distortion of the peak was observed. Here $B/\sigma \approx 2.4$, $A \approx 0.16$, $\delta \approx 0.84\pi$. Because of the small value of A, it compares best to the prediction for $A = 0$, $\delta = 0$ in Fig. 5.5. While for smaller RF amplitudes, a maximum of the count rate is observed close to the mean time-of-flight, the smaller relative count rate oscillation amplitude does not reduce the peak distortion. The green line shows a Gaussian fit to the spectrum corrected for the time-of-flight oscillation and is much more narrow. For ^{85}Rb and ^{133}Cs, a series of systematic measurements with different RF amplitudes was performed. The measured time-of-flight oscillation amplitudes are presented in Fig. 5.10. For both isotopes, there is an onset of the ToF oscillation at a certain amplitude and then a linear increase. Measurement with ^{39}K where not possible, since for too strong RF amplitudes, the RFQ contained too much

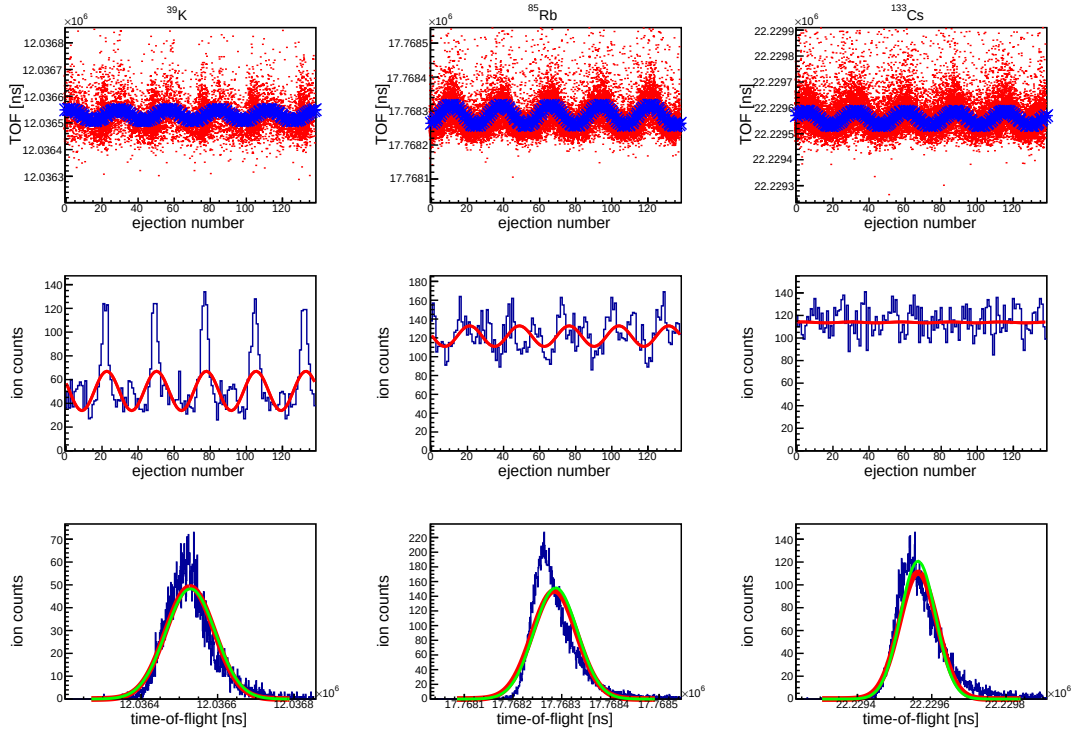

Figure 5.8: Scan of the RF phase for ^{39}K, ^{85}Rb and ^{133}Cs over five RF periods with 800 revolutions inside the MR-ToF MS. For description, see Tab. 5.2.

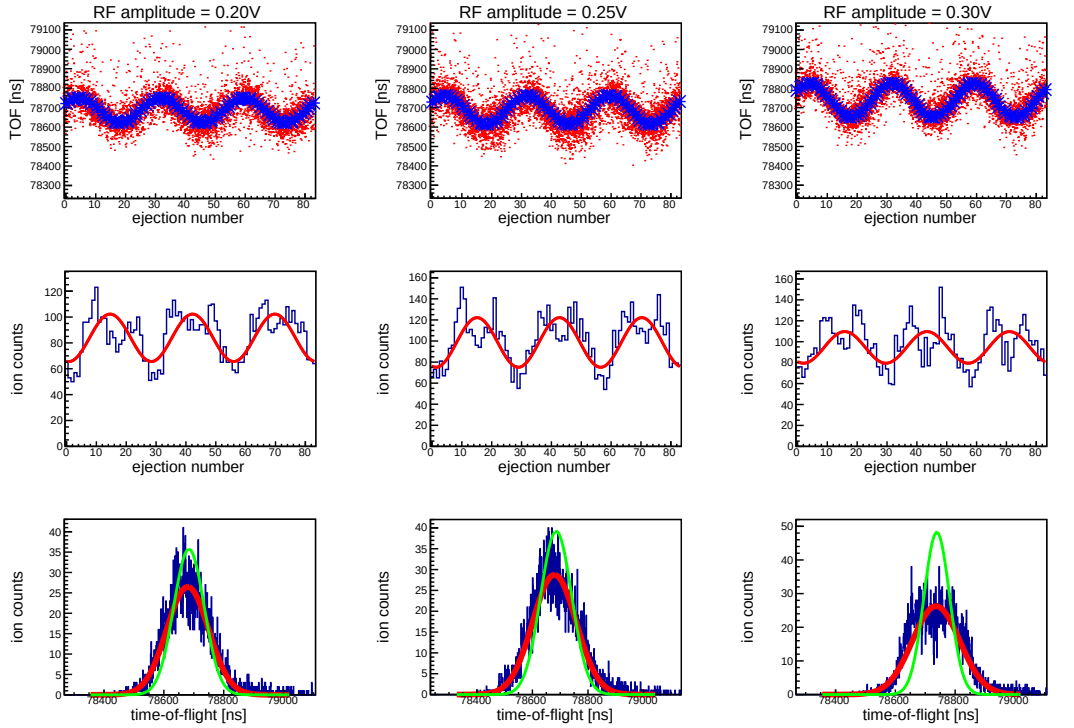

Figure 5.9: RF phase scan for ^{85}Rb with different RF amplitudes and 2 revolutions inside the MR-ToF MS as described in section 5.2.2. The quoted RF amplitude is the one set on the RF generator. Description see Tab. 5.2.

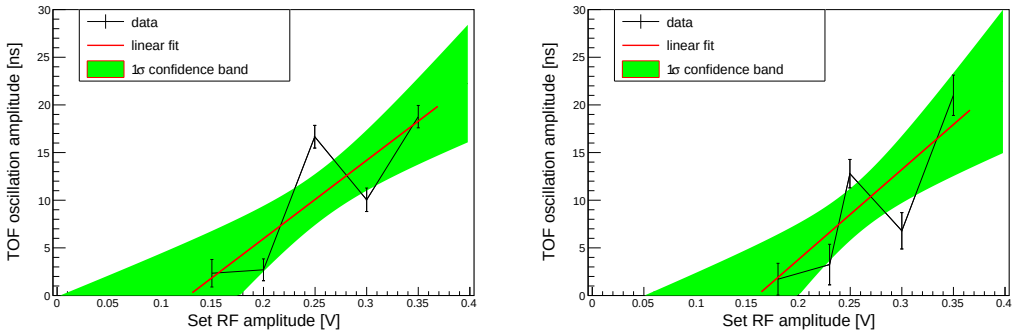

(a) ^{85}Rb (b) ^{133}Cs

Figure 5.10: Time-of-flight oscillation amplitude measured for different RF amplitudes set on the frequency generator (a) for ^{85}Rb and (b) for ^{133}Cs.

^{133}Cs. Thus, an efficient cooling of the ions was not longer possible. This is investigated in section 7.1.1.

5.3 Adjustment of RF timing

In order to reduce the time-of-flight shifts and line shape distortion described in section 5.2.1 and observed experimentally as investigated in section 5.2.2, one can reduce the RF amplitude as was shown in Fig. 5.10. But this is not the best option, because this would cause a loss of efficiency as can be seen in Fig. 5.4. But the RF amplitude at the moment of extraction can be changed by switching off the frequency generator creating the RF signal before the extraction without affecting the cooling time of the ions. The time difference between the switching off of the RF t_{RF} and the moment of extraction t_{extr} is called *RF delay* and is defined as

$$RFdelay = t_{RF} - t_{extr}. \tag{5.24}$$

As displayed in Fig. 5.11, the frequency generator can be switched off up to 8 µs before the extraction pulse with a loss in count rate of less than 20 %. In Fig. 5.12 it is shown, that the time-of-flight oscillation disappears, when switching off the RF generator earlier. In Fig. 5.13, the data for the delays −8 µs, 0 µs and 2 µs is shown for ^{85}Rb and ^{39}K. It can be seen, that the time-of-flight dependence of the RF phase disappears and that the peaks get more symmetric when going to a RF delay of −8 µs. Also the oscillation of the count rate is reduced. The line-shape of the time-of-flight spectrum (row 3) is well described by a Gaussian for an RF delay of −8 µs and both fits, to the measured spectrum (red line) and to the corrected spectrum (green line, see section 5.2.2) coincide. In contrast, for the old setting with an RF delay of 2 µs, the peaks show a significant tail towards higher times of flight.

5.4 Simulations of the RF phase dependence

The RF phase dependence was investigated with simulations by storing the initial ion distribution generated as described above with an initial RF phase of $\xi = 0$ for different times before extraction. This way, the phase at the moment of extraction was varied. The observed oscilla-

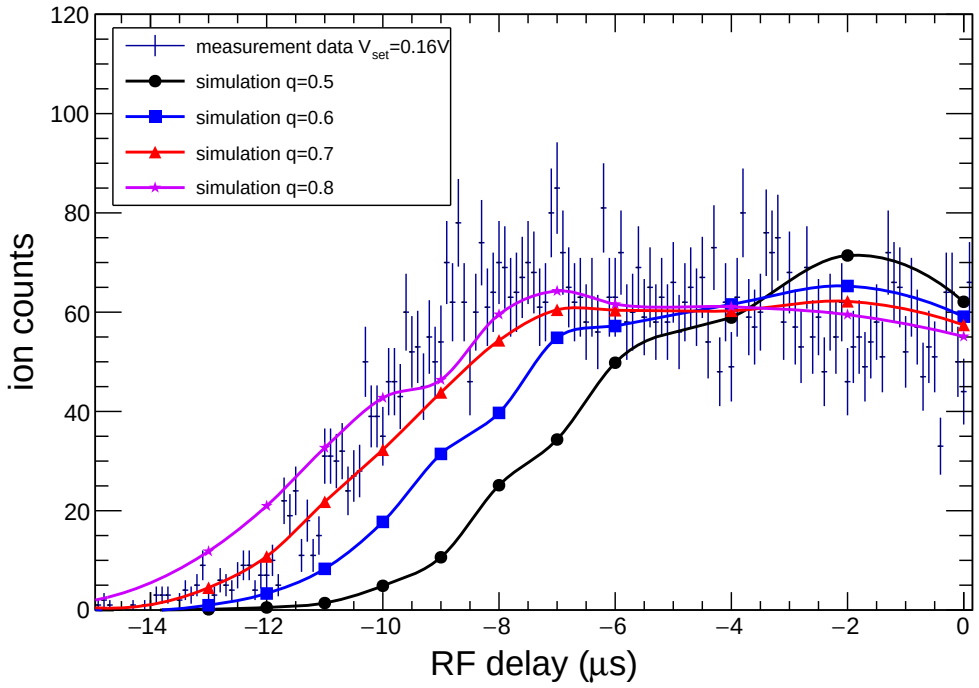

Figure 5.11: Experimental data of the scan for the transmission of ^{39}K depending on the RF delay (definition see Eq. (5.24)) and the simulated data for different q-values. In the simulation, the transmission is averaged over four RF periods and scaled to the measured data by a fit of a linear extrapolation of the simulation to the plateau region of RF delays bigger than $-8\,\mu s$. For details of the simulation, see section 5.5.

tions could be reproduced at least qualitatively and it could be shown, that the fluctuations of the transmission as well as of the time-of-flight depending on the storage time have the same period as the RF. This is shown in Fig. 5.14. Here, ^{39}K ions with $q = 0.6$ and simultaneous ejection and switching off of the RF was simulated. The time-of-flight oscillation is well reproduced with a sine function. Also for the count rate, some maxima and minima follow a sinusoidal curve with RF period (black points in Fig. 5.14b), but a second pattern seems to be cover this oscillation for other storage times (red points). Between both fits, there is a phase difference of $\delta \approx -\pi/4$. The relative shift of the mean time-of-flight was calculated for several masses and trap parameters q (see Eq. (2.11)) with 2 revolutions inside the MR-ToF MS. The results are shown in Fig. 5.15. No significant dependence on mass and q could be seen, but a constant relative shift of $\Delta ToF/T_0 \approx -1 \cdot 10^{-5}$.

5.5 Simulations of the timing of the switching-off of the RF

To understand the removal of the RF phase dependence when switching off the RF signal before the moment of extraction, the RF signal was recorded with two antennas next to the RFQ segment 25, where the ions are stored. The signal was recorded with an oscilloscope triggered on the switching off of the RF. The recorded signal is depicted in Fig. 5.16. When switching off the RF, the frequency generator completes the current RF period and then emits no RF

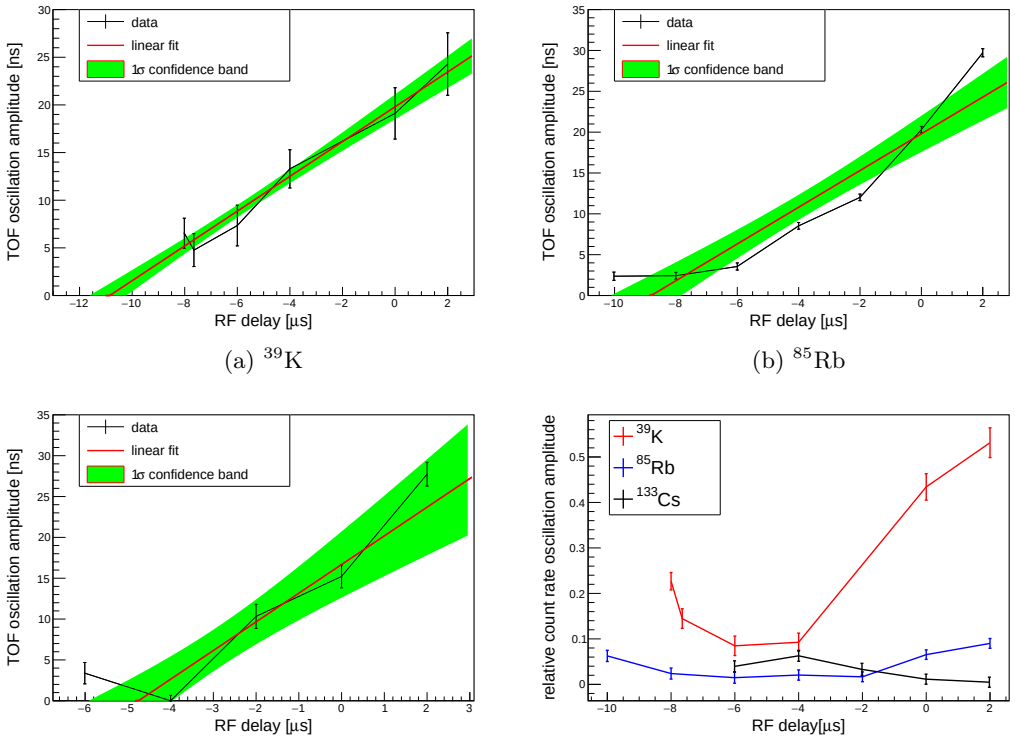

(a) ^{39}K (b) ^{85}Rb

(c) ^{133}Cs (d) Relative count rate oscillation amplitude

Figure 5.12: Measured time-of-flight oscillation amplitudes for different timings of the switching off of the RF frequency generator. (a) for ^{39}K (b) for ^{85}Rb and (c) for ^{133}Cs. For ^{39}K, the RF amplitude was set to 0.16 V, for ^{85}Rb and ^{133}Cs it was set to 0.25 V. In (d), the relative count rate oscillation amplitude is displayed.

signal any more, but the resonance circuit continues to oscillate while the amplitude decreases exponentially: $A(t) \propto \exp(-t/\tau)$. A decay time of $\tau = 8.7\,\mu s$ was measured. This exponential decay was included into simulations in which the RF was switched off before the extraction for different RF amplitudes. The simulated transmission is compared to data measured on the electron multiplier EMP2h with ^{39}K and an RF amplitude set to 0.16 V. This is shown in Fig. 5.11. Since the experimental detection efficiency and the number of trapped ions inside the RFQ is not known precisely, the simulated transmission probability is scaled by a constant factor. This is obtained by fitting a linear interpolation between the simulated points to the data in the plateau region from $-8\,\mu s$ to $0\,\mu s$. While the on-set of the transmission at an RF delay of about $-12\,\mu s$ is well described with the simulations for $q = 0.7$, the arrival of the plateau at an RF delay of about $-8\,\mu s$ is in good agreement with the simulations with $q = 0.8$. The amplification factor F estimated in section 5.1.2 corresponds to $q = 0.62 \pm 0.03$ for the given RF amplitude set to 0.16 V on the RF generator. The simulations were performed with a drawing of the new guiding lens (see Fig. 5.1 and chapter 6) because no drawing of the old one was available. This may be a hint, that the new lens might have a higher acceptance than the old one. Nevertheless, it can be concluded, that the dependence of the transmission on the RF amplitude and delay are well matched by the simulations. This implies, that the initial ion cloud used for it is a good set for future simulations of changes in the beam optics. A decrease of the RF phase dependence was observed. Like in the experiment, the phase dependence of the

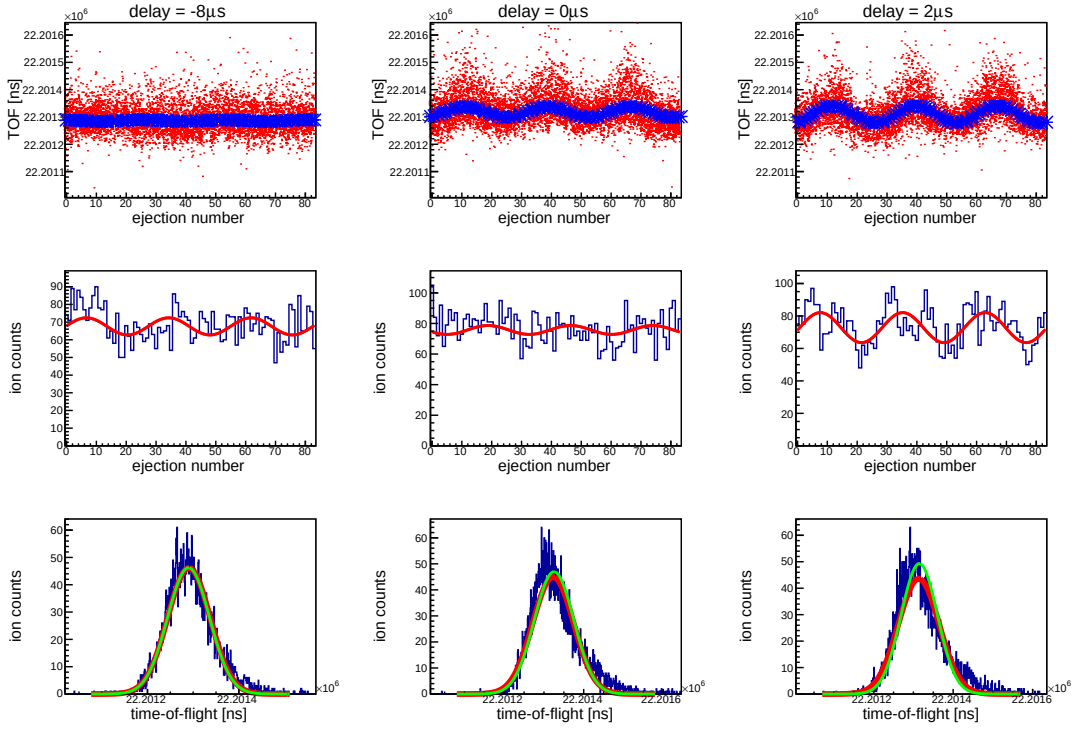

(a) ^{85}Rb

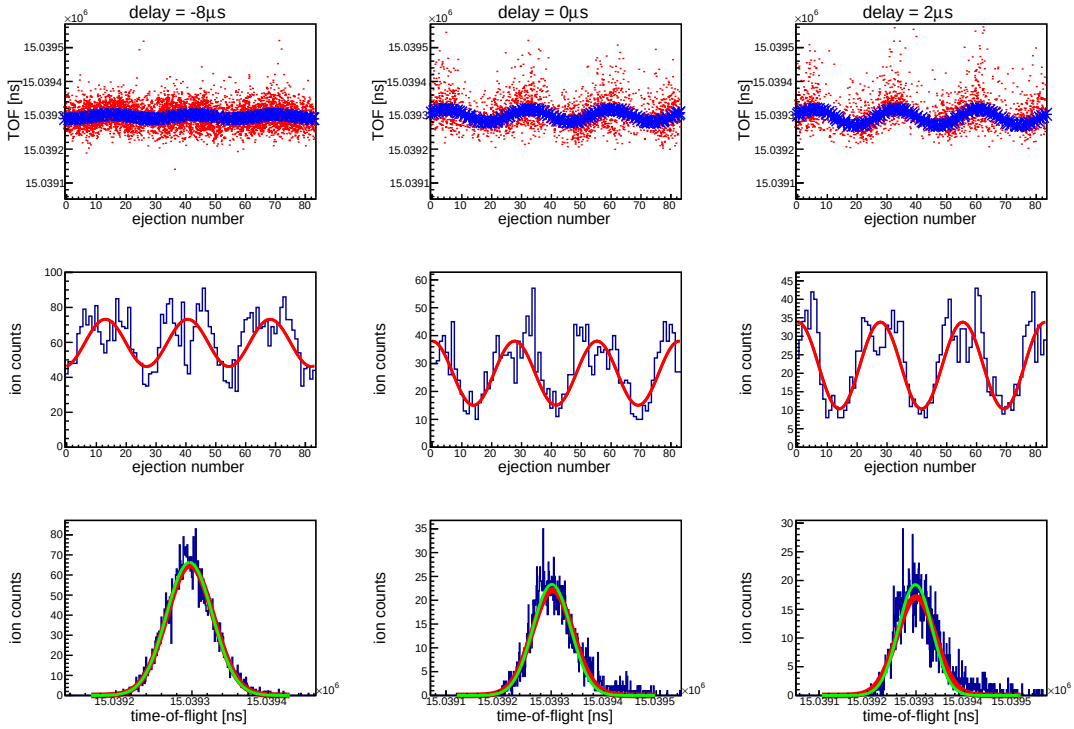

(b) ^{39}K

Figure 5.13: RF phase dependence of the ToF and transmission (a) for ^{85}Rb and (b) for ^{39}K depending on the delay of the switching off of the RF with respect to the extraction pulse (from left to right $-8\,\mu s$, $0\,\mu s$, $2\,\mu s$). Description see Tab. 5.2.

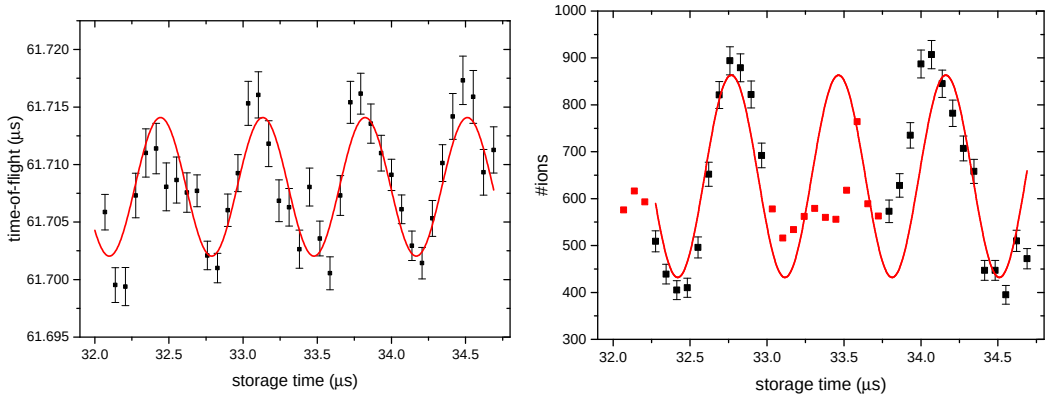

(a) Simulated ToF oscillation

(b) Simulated count rate oscillation

Figure 5.14: (a) Simulated mean time-of-flight and (b) transmission to the new electron multiplier depending on the storage time in the RFQ buncher and therefore of the RF phase. The simulation (number of ions out of the 1000 generated as described in section 5.1) was performed for ^{39}K with $q = 0.6$ and the RF being switched off at the moment of extraction. A sine function was fitted to the entire time-of-flight and to the black data points for the rate. In both cases, the frequency is in perfect agreement with the RF frequency. For the rate, this oscillation is superimposed by pattern investigated in section 5.5 and probably caused by the macromotion.

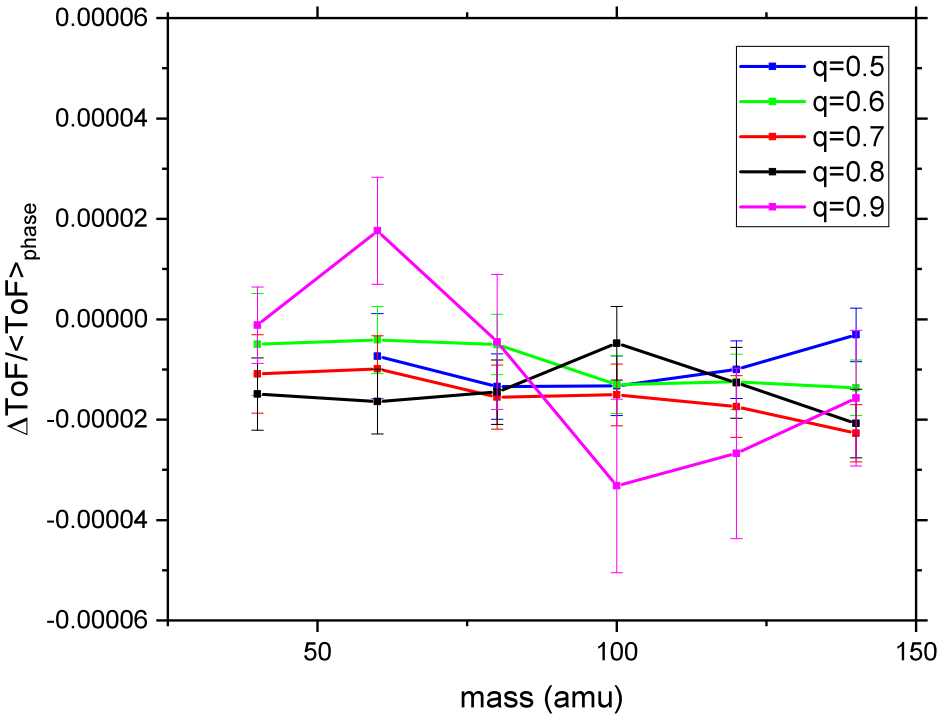

Figure 5.15: Simulated relative time shift depending on the mass and the RF working point q for $N = 2$ revolutions in the MR-TOF MS.

count rate on the RF phases decreases for ^{39}K while the time-of-flight dependence is strongly reduced for switching-off the RF before extraction. In Fig. 5.17 the time-of-flight of ^{39}K from the

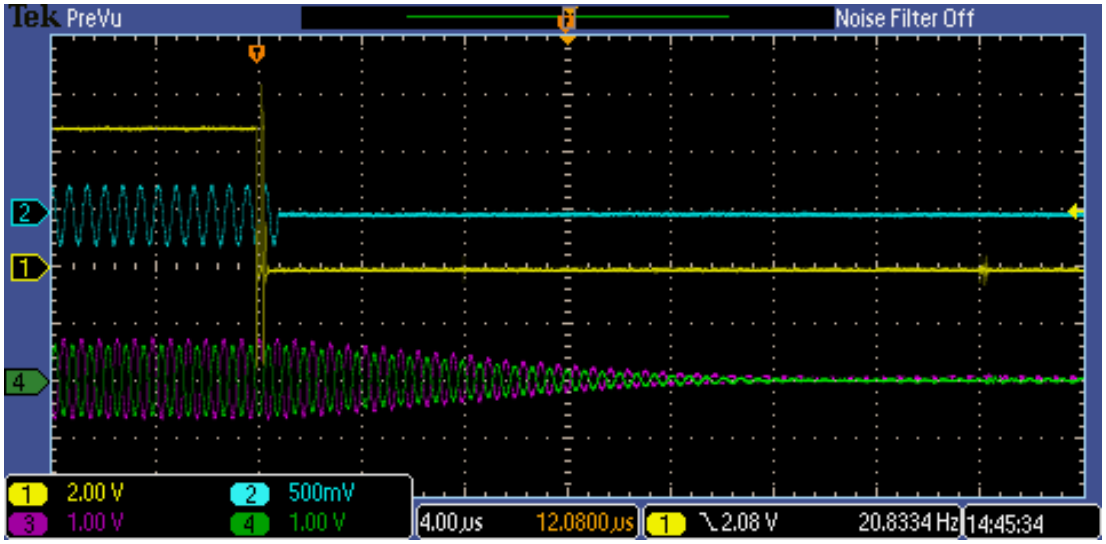

Figure 5.16: Drop of the RF amplitude at the resonance circuit after switching off the RF generator. Channel 1 shows the TTL signal triggering the RF generator, channel 2 the output of the RF generator, and the channels 3 and 4 show the signal measured on two coils inside the RFQ buncher close to the trapping region.

buncher to the electron multiplier is displayed for the RF delays 2 µs, 0 µs, −8 µs and −10 µs. For this simulation, an identical RF amplitude for all four simulated buncher segments was assumed. For the delays 2 µs and 0 µs, periodic peaks with the distance of one RF period are visible. For the earlier extraction with delays of −8 µs and −10 µs, a periodic structure with a period that is about twice as long appears. This can be explained with the macromotion of the ions inside the RFQ. This hypothesis was checked by changing the RF amplitude and therefore the frequency of the macromotion which is given by equation (2.16) and (2.14) as

$$\nu_m = \frac{\beta \cdot \nu_{RF}}{2} \tag{5.25}$$

$$\overset{eq.(2.16), a \ll 1}{\approx} \left[\frac{q^2}{2 - q^2} - \frac{7q^4}{128} + \frac{29q^6}{2304} \right]^{1/2} \cdot \frac{\nu_{RF}}{2}. \tag{5.26}$$

Since the ion optics until the quadrupole bender and therefore the acceptance are symmetric with respect to their axis, equivalent positions are reached after half a period. Therefore, the period of the measured patterns is given by the frequency

$$\nu_{rep} = \beta \cdot \nu_{RF}. \tag{5.27}$$

The simulation was repeated for $q = 0.4,\ 0.6$ and 0.8 for an RF delay of −8 µs. The results are presented in Fig. 5.18. The periodic behaviour agrees with β calculated from q using equation (5.26). This effect was not observed experimentally. This might be due to the buffer gas or the continuous ion capture during the beam gate not included in this simulation. In the MR-ToF MS experiment in Gießen [67], the problem of the ringing of the RF signal and therefore different electric fields for different ion species was circumvented by using a rectangular voltage signal and switching off the RF before the extraction. This means that there is no RF field while the ions are extracted. Using simulations, it was checked if such a fast switching-off of the RF would improve the situation at ISOLTAP. The simulated transmission probability depending on the

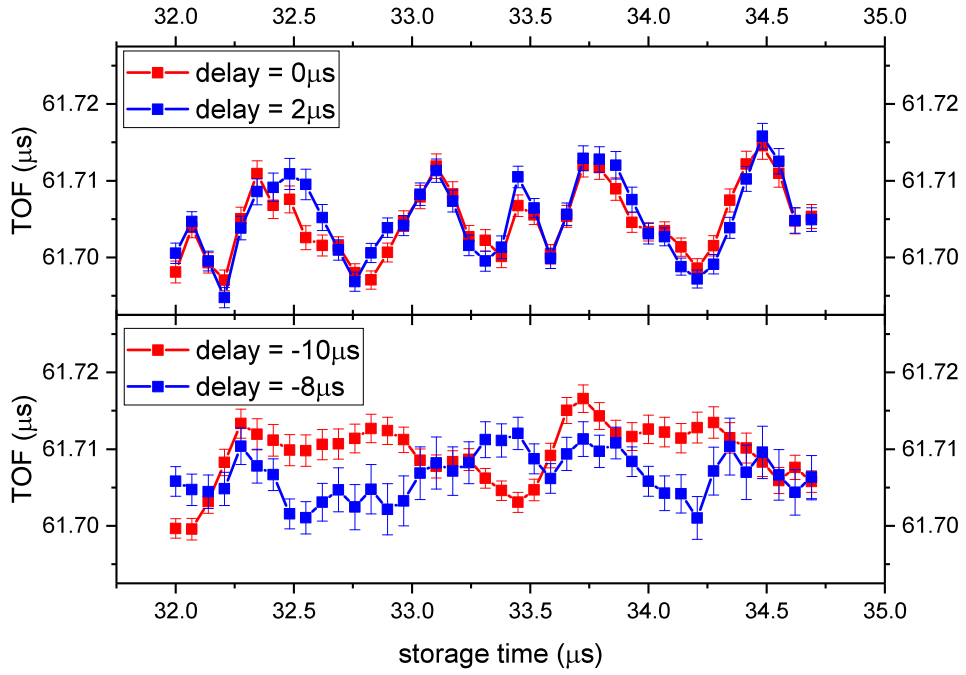

Figure 5.17: The dependence of the time of flight on the RF phase at the moment of extraction for switching off the RF at different times (positive delay means after extraction). This simulation was performed for ^{39}K with two revolutions inside the MR-ToF MS.

RF decay time for a synchronous extraction and switching-off of the RF for ^{39}K and $q = 0.7$ is depicted in Fig. 5.19. It was shown that an RF decay time smaller than the time-of-flight of the ions through the buncher of about 2 µs lead to a significant loss in count rate. This is due to the fact that the buncher acts as an ion guide during the extraction. If the RF field decreases too fast the ion cloud diverges too strongly and is lost. So no such improvement can be made for the geometry used at ISOLTAP.

5.6 Optimization protocol for buncher preparation

The measured dependence of the RF depends on the current settings of the ISOLTRAP cooler and buncher and of the subsequent ion optics. Especially the amplification factor F of the coupling boxes transferring the RF signal from the RF generator to the RF electrodes (see chapter 5.1.2) can be changed. Nevertheless, an optimization protocol for the preparation of a measurement campaign can be given. As pointed out in Fig. 5.4 and 5.11, the ion count rate depends on both, the timing of the radio frequency, as well as on the RF amplitude. For the preparation of the buncher for a measurement, the following protocol is proposed to be performed with an isobaric contaminant or, if the count rate is high enough, with the ion of interest itself, as well as with the off-line reference ions:

1. Find an appropriate RF amplitude with maximal count rate. As shown by the simulations in Fig. 5.3a, this can be done by scaling from the maxima of off-line references or by doing a scan of the RF amplitude as in Fig. 5.4.

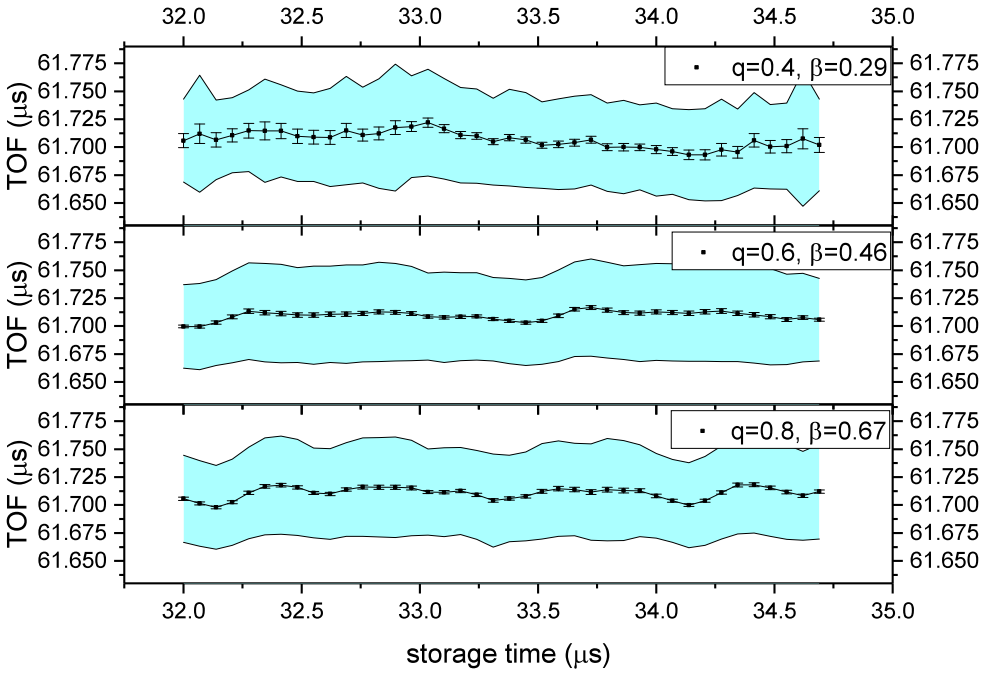

Figure 5.18: Time of flight dependence on the RF phase for an RF delay of $-8\,\mu s$ at different working points q for ^{39}K. The band shows the standard deviation of the ToF-spectrum, the small error bars the statistical uncertainty of the mean. The means show a small periodic structure with a frequency $\nu_{rep} = \beta \cdot \nu_{RF}$. The storage time range shows four RF periods. The solid lines are used to illustrate the periodicity of the pattern.

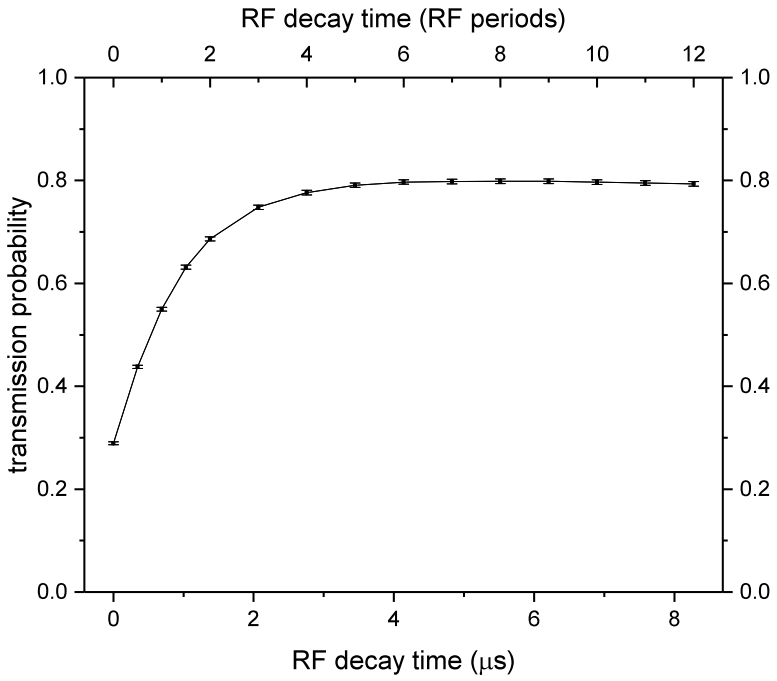

Figure 5.19: Simulated transmission probability depending on the RF decay time for a synchronous extraction and switching-off of the RF for ^{39}K and $q = 0.7$.

2. Scan the RF delay and record the count rate as in Fig. 5.11. Identify the kink at which the ion count rate starts to decrease and set the RF delay to it.

3. Scan the RF phase and check, if any RF phase dependence of the time-of-flight is still visible. If yes, increase the RF delay in small steps until the RF phase dependence disappears or the loss in count rate is unacceptable.

4. When measuring the time-of-flight for mass measurements, scan the RF phase over an integer multiple of the RF period to average out any remaining RF phase dependence.

6 Design of a new guiding lens for refocusing decelerated ions

This chapter addresses the work performed for redesigning and replacing an einzel lens located between the pulsed drift tube behind the RFQ and the MR-ToF MS and denoted as guiding lens (see figure 6.1). Its role is to focus the diverging beam from the pulsed drift tube and prepare it so that it can be properly injected into the MR-ToF MS by the subsequent Einzel lens named "Lens in" with a small divergence angle. Therefore, it is crucial for the transmission of the set-up. Formerly it also had the role of focusing the ions onto the first detector of the ISOLTRAP set-up (either an MCP or a Faraday cup), however in the meantime the MCP has been removed. Since the potential of its electrodes have a direct impact on the ion velocity and therefore their time-of-flight, they should remain constant over time. As will be illustrated below, the former version of the lens produced a series of problems which motivated its redesign.

6.1 The old guiding lens

A picture of the old lens was taken during an intervention in 2011 and is depicted in figure 6.2. It consists of an isolating foil with a thin conducting layer (visible in figure 6.2b) for the charged central electrode on it. The grounded pulsed drift tube, together with the grounded mounting behind it, created the Einzel-lens potential arrangement (for working principle see chapter 2.4). The old lens caused issues in the past and also during the time of this work. It changed its optimal settings (voltage applied for maximal transmission) significantly and sometimes suddenly over time. Ramping it up to a high voltage and then ramping it down again was sufficient to regain the old transmission, which implies that the isolating foil of this einzel lens might charge up. Since this causes a significant loss of count rate and since it also determines drifts of the time-of-flight of the ions to the MR-ToF MS, it was decided to replace the old guiding lens by a new, fully metallic one.

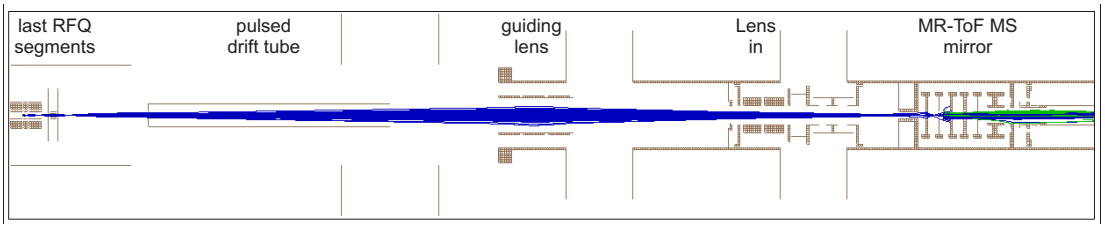

Figure 6.1: Simulation of ion trajectories from the last four RFQ segments through the new guiding lens (see text) and Lens in into the MR-ToF MS. Blue trajectories go to the right, green trajectories to the left.

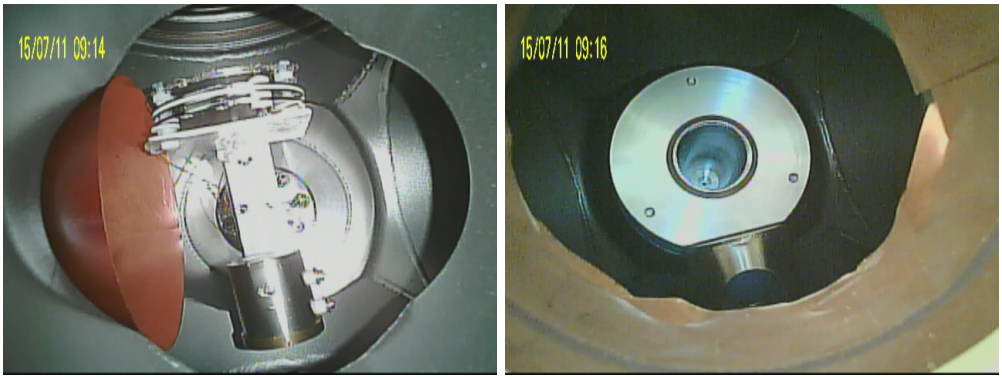

(a) Transversal view (b) Longitudinal view

Figure 6.2: Photos of the old lens (red) taken during an intervention in 2011, (a) horizontal view (beam direction from left to right), together with a Faraday cup and an MCP detector on a rotatable feedthrough. The can be rotated into the beamline. (b) longitudinal view against the beam direction.

6.2 Design of a new guiding lens

The diameter of the lens is limited by the CF100 6-way-cross, in which it is placed and by the distance to the Faraday cup. It also must be possible to install it ideally without having to move the crosses in front and behind it (see Fig. 6.2. Therefore, it should be completely contained inside the CF160 to CF100 zerolength adapter flange and the following cross. It can be built into the flange and into the cross. In such a design, it would be possible to slide the whole cross into position. This yields a maximal length of 120 mm and a maximal outer diameter of 100 mm. To find an appropriate geometry, a simulation of the ion trajectories from the buncher through the MR-ToF MS to the electron multiplier EMP2h with two revolutions inside the MR-ToF MS was performed with one fixed phase of the RF at the moment of extraction (see chapter 5). First, electrodes with equal length were assumed, then the voltages applied to all electrodes were optimized for maximal transmission using a simplex algorithm. Then, the total length of the lens was fixed to $l_{tot} = 120\,\text{mm}$ and the distance between the electrodes to $d = 5\,\text{mm}$. The two grounded electrodes were assumed to be symmetric and the radii of all electrodes to be identical. The length of the two symmetric electrodes which are on ground potential was linked to the length of the central electrode l_c by

$$l_g = \frac{l_{tot} - 2d - l_c}{2}. \tag{6.1}$$

Then, the electrode radius, l_c and the positive voltage applied to the central electrode were varied. A geometry was chosen, that allows for a high transmission with a small dependence on the voltage. Since the other electrodes such as the ones belonging to "Lens in" were not varied, the results were not completely independent of assumptions, but it was visible, that the beam width at the position of the guiding lens is about 30 mm. The radius of the lens should be significantly larger to achieve good lensing properties. Therefore, the maximal inner electrode diameter of 50 mm allowed by the spatial restrictions for the design was chosen. The length of the central electrode was chosen to be 55 mm giving good results. After optimization with a simplex algorithm, the simulation predicted a transmission through the MR-ToF MS MS with two revolutions of around 92 % for the chosen ion sample of 1000 ions (see chapter 5.1). For a

bigger electrode diameter of 55 mm, even 94 % could be achieved for the same sample, implying that the diameter should be as big as possible.
The lens including its mount was drawn with Autodesk Inventor [68]. A half section view of the installed lens is shown in figure 6.3, a photo of the assembled lens in 6.4. The general concept is the following:

1. the zero-length adapter is modified by reducing the inner diameter by a layer with four tapped holes.
2. a ring support is fixed with threads mounted in these holes.
3. four threaded rods are additionally fixed at the ring. They represent the support structure of the lens itself.
4. on these rods, the three electrodes are fixed by nuts and washers.
5. between the threaded rods and the centre electrode, isolators are added. The outer two electrodes are connected to ground by the rods.

The modified adapter flange, the mounting ring and the three electrodes were ordered for manufacture at VACOM Vakuum Komponenten & Messtechnik GmbH. In cooperation with them, the 3D drawings were converted into 2D drawings ready to be handed in for the production. The ceramic isolators to isolate the central electrode where ordered at MISUMI Europa GmbH and the threaded rods in the CERN store. When all components were delivered, a test assembly of the lens was done. The assembled lens is depicted in figure 6.4. The lens is now ready to be built-in.

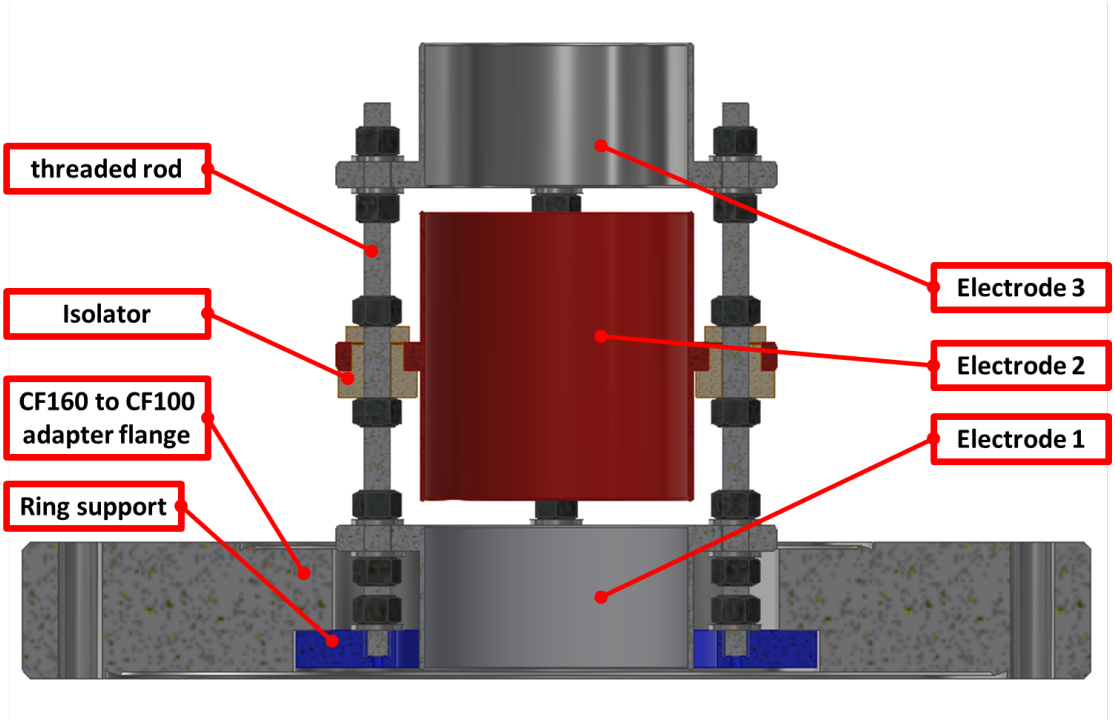

Figure 6.3: Half section view of the design of the new guiding lens, including the modified CF160 to CF100 zero-length adapter flange. The colors are chosen for better visibility.

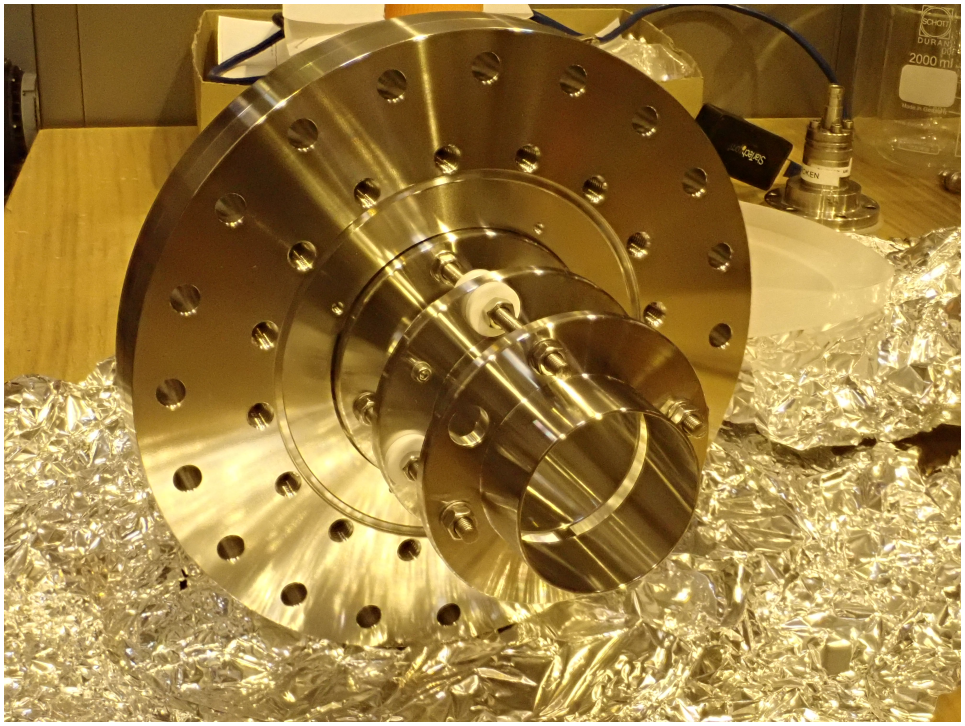

Figure 6.4: Assembled guiding lens including adapter flange.

7 Energy spread and mass measurement with ISOLTRAP's MR-ToF MS

The ISOLTRAP Multi-Reflection Time-of-Flight Mass Spectrometer/Separator [59] was the first device of this kind to be used for high-precision time-of-flight mass measurements and beam preparation for Penning-trap measurements. It was installed at the ISOLTRAP setup in 2012 [41] and was followed by similar devices in RIKEN [69, 70], at TITAN/TRIUMF [64, 71] based on an MR-ToF MS developed at the University of Gießen [67], and one at CARIBU [72]. All of these devices have a typical mass separation power of $R \approx 10^5$ and allow mass measurements with a typical precision of $\frac{\delta m}{m} = 10^{-7}$. Currently, a series of new MR-ToF MS devices is planned or in commissioning, for example at the low energy branch of FAIR [73], at SPIRAL 2 at GANIL [74]. For theoretical explanations, see chapter 2.3. In a first section, it is explained, how the in-trap lift technique described in chapter 4.3.3 is used to obtain a time-of-flight focus on the detector and to obtain maximal mass resolving power. It is explained, how this technique can be used to estimate the width of the energy distribution of the measured ion cloud emerging from the RFQ cooler and buncher. In a second section, the topic of MR-ToF on-line mass measurements using entirely off-line references is addressed. This is an important change with respect to previous measurements, in which at least one of the used references was an isobar of the ion of interest and was measured in the same time-of-flight spectrum. For this extension, the stability of the ISOLTRAP MR-ToF MS was investigated using off-line reference ions.

7.1 Time-of-flight focus

At the ISOLTRAP experiment, ions are trapped in and ejected from the MR-ToF MS with a so called in-trap lift[40]. This is a drift tube between the mirrors which is switched down from a potential V to ground when the ions are inside. Then, the ions have not enough energy any more to pass over the potential of the mirrors and are electrostatically trapped. For ejection, the in-trap lift is switched back to V. By changing V, the energy of the ions inside the MR-ToF MS and consequently their turning point is changed and the dispersion $\frac{\partial T_0}{\partial E}$ is adapted, until

$$\Delta t_E = 0. \tag{7.1}$$

This minimizes the time-of-flight width in Eq. (2.48) and the mass-resolving power in Eq. (2.50)

$$R = \frac{t}{2\Delta t} = \frac{t_s + n \cdot T_0}{2\sqrt{\Delta t_{therm}^2 + (n \cdot T_0 \cdot \delta_{abb})^2}} \tag{7.2}$$

is achieved. In Fig. 7.1, such a scan of the in-trap lift voltage is shown.

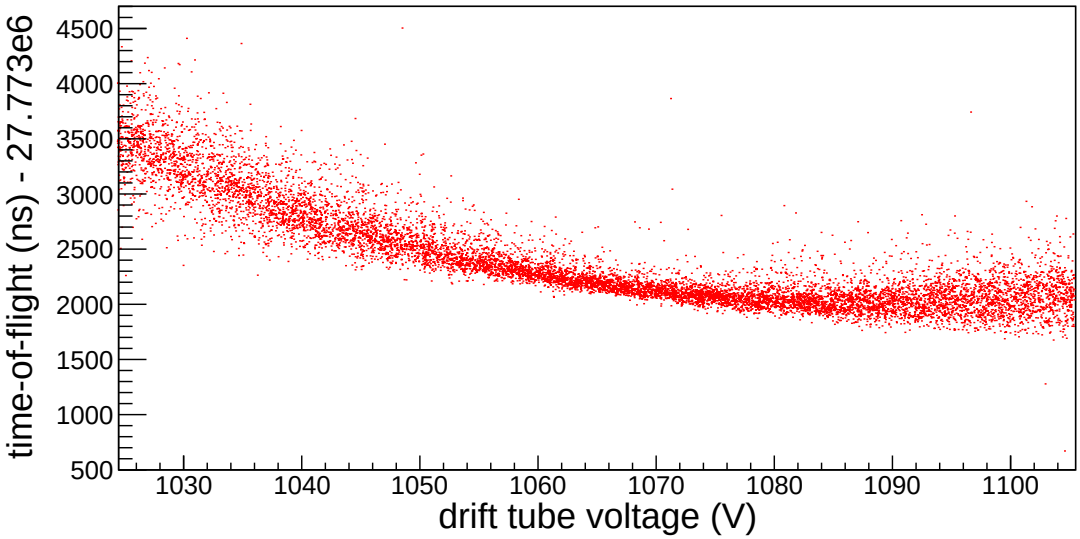

Figure 7.1: Scan of the voltage of the central drift tube of the MR-ToF MS for ^{133}Cs with 1000 revolutions.

7.1.1 Estimation of the energy spread

As stated in equation (2.48), the width of the time-of-flight distribution behind the MR-ToF MS has a width given by the formula

$$\Delta t = \sqrt{\Delta t_{th}^2 + (n \cdot T_0 \cdot \delta_{abb})^2 + (\Delta t_s - n \cdot \frac{\partial T_0}{\partial E} \cdot \Delta E)^2} \tag{7.3}$$

(see [40]and [59]) with the thermal turn-around time Δt_{th}, the-time-of flight width caused by the different time-of-flight outside the MR-ToF MS including the spacial spread in the source Δt_s, the number of revolutions n, the mean time for one revolution T_0, a relative broadening because of aberrations, quick voltage fluctuations, etc. δ_{abb}, the kinetic energy of the ions inside the MR-ToF MS E and its spread ΔE. The ions start with the total energy $E_0 \approx 3200\,\mathrm{eV}$ after the HV pulse down tube, fly into the MR-ToF MS. Then, the in-trap lift is switched from potential V to ground, such that

$$E = E_0 - V \tag{7.4}$$

and therefore

$$\frac{\partial T_0}{\partial E} = -\frac{\partial T_0}{\partial V}. \tag{7.5}$$

In the time focus with optimal voltage V_{opt}

$$\Delta t_s - n \cdot \frac{\partial T_0}{\partial E} \cdot \Delta E = 0. \tag{7.6}$$

Around this setting, the linear approximation

$$n \cdot \frac{\partial T_0}{\partial E} = c_0 + c_1 \cdot V \tag{7.7}$$

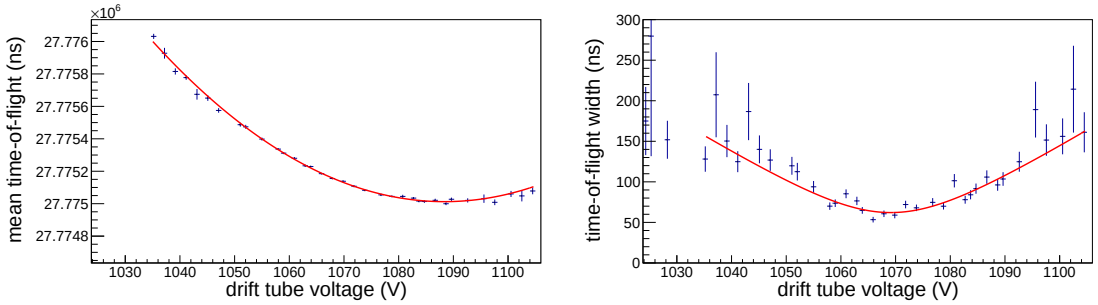

(a) mean time of flight

(b) time-of-flight RMS

Figure 7.2: Estimation of the beam energy spread (see text).

holds. If one inserts this into Eq. (7.3), one gets

$$\Delta t = \sqrt{\Delta t_{th}^2 + (n \cdot T_0 \cdot \delta_{abb})^2 + (\Delta t_s - (c_0 + c_1 \cdot V) \cdot \Delta E)^2} \tag{7.8}$$

$$= \sqrt{\Delta t_{th}^2 + (n \cdot T_0 \cdot \delta_{abb})^2 + (c_1 \cdot \Delta E)^2 \cdot [\frac{\Delta t_s - c_0 \cdot \Delta E}{c_1 \cdot \Delta E} - V]^2} \tag{7.9}$$

$$=: \sqrt{a^2 + b^2 \cdot [V_{opt} - V]^2} \tag{7.10}$$

with the newly defined parameters

$$a^2 = \Delta t_{th}^2 + (n \cdot T_0 \cdot \delta_{abb})^2, \tag{7.11}$$

$$b^2 = (c_1 \cdot \Delta E)^2 \tag{7.12}$$

and

$$V_{opt}(n) = \frac{\Delta t_s - c_0 \cdot \Delta E}{c_1 \cdot \Delta E}. \tag{7.13}$$

Here, $V_{opt}(n)$ is the voltage with the time focus on the detector. When scanning the cavity voltage around the focus, one receives for the mean values a histogram $t(n, V)$ and for the peak width $\Delta t(n, V)$. Fitting the latter histogram with equation (7.10) returns the parameters a, b and V_{opt}. The histogram with the means is fitted with the integral of equation (7.7)

$$t(V) = T_{offset} - c_0 \cdot V - \frac{c_1}{2} \cdot V^2. \tag{7.14}$$

The energy spread ΔE is then given by

$$\Delta E = \left| \frac{b}{c_1} \right|. \tag{7.15}$$

Such a fit is depicted in Fig. 7.2 with the same data as depicted in Fig. 7.1. For ^{85}Rb several values in the range $\Delta E \approx 4\,\text{eV} - 7\,\text{eV}$ were determined, for ^{133}Cs, measured values were in the range $\Delta E \approx 7.5\,\text{eV} - 10\,\text{eV}$. During the extraction, the ions are on a potential ramp with a gradient of $\frac{\partial \Phi}{\partial x} = -9.6\,\text{V}\,\text{mm}^{-1}$. Therefore, the measured value corresponds to an ion cloud with a longitudinal spread of $\Delta x \approx 0.4\,\text{mm} - 1\,\text{mm}$, compared to $\Delta x \approx 0.4\,\text{mm}$ in Fig. 5.2a. Simulated ions had an energy spread of $\Delta E \approx 5\,\text{eV}$. These simulations take into account the raise time of the switches, but do not take into account voltage fluctuations and a broadening of

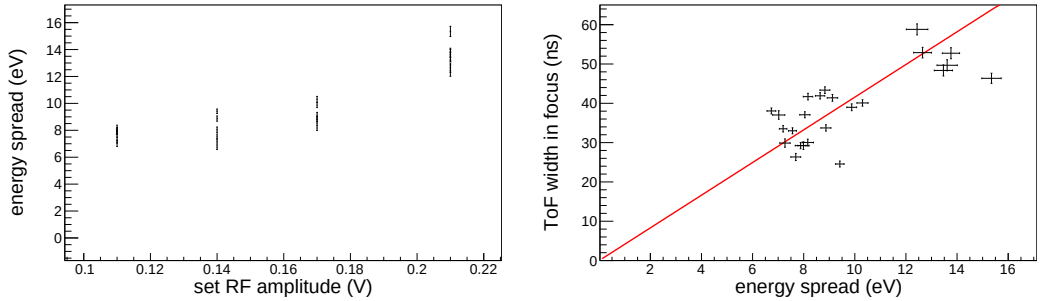

(a) energy spread

(b) Correlation of time-of-flight focus width in the and energy spread

Figure 7.3: Measurement of the standard deviation (a) of the energy. For each set RF amplitude, 6 points were measured. (b) correlation of the time-of-flight focus width end the measured energy spread for different set RF amplitudes with 800 revolutions in the MR-ToF MS. For details to the fit (red line), see text.

the energy spectrum by ion-ion and ion-rest gas interaction after thermalization and therefore systematically underestimate the energy spread.

Ion-ion interaction in the RFQ

In one measurement series, the time-of-flight spectrum for ^{39}K was broadened and asymmetric. This was found after the yearly shutdown of the setup, when the efficiency of injecting ^{133}Cs in the RFQ cooler-buncher might have been larger than before. Wrong timings of the switches were excluded as possible reason. The broadening was observed for RF amplitudes bigger or equal than 0.16 V (set-point of the frequency generator), which is the lower limit for successful trapping of ^{133}Cs in the RFQ. Because of a low production rate of ^{39}K, a beamgate of 10 ms was used, compared to 5 µs for ^{133}Cs. Consequently big amounts of ^{133}Cs are trapped, too. With higher RF amplitude, the trapping efficiency for of ^{133}Cs increases further. Measurements of the energy spread and time-of-flight width in the focus with different RF amplitudes were repeated with the method described in 7.1.1. The results are shown in Fig. 7.3. It is clearly visible that the energy spread of the ions, determined by their spatial spread inside the RFQ, increases if the RF amplitude is set to 0.16 V or more. Fig. 7.3a also illustrates the precision of the method of about ±1 eV. The increase in energy spread correlates with a broadening of the peak in the focus as can be seen from Fig. 7.3b. In the focus, the beam width given in Eq. (7.3) reduces to the quadratic sum of thermal turn-around time t_{therm} and a broadening due to aberrations and voltage instabilities Δt_{abb}:

$$\Delta t = \sqrt{\Delta t_{therm}^2 + \Delta t_{abb}^2}. \tag{7.16}$$

The spatial spread of the ions inside the RFQ Δx can be estimated from their charge e, the energy spread ΔE and the electric field E_x during the extraction as

$$\Delta x = \frac{\Delta E}{e \cdot E_x}. \tag{7.17}$$

While the ions are trapped in the RFQ, the energy in the x-dimension is equally partitioned between kinetic and potential energy. The kinetic energy is given by

$$< E_{kin,x} >= \frac{\Delta p_x^2}{2m} \tag{7.18}$$

with the axial momentum spread Δp_x and the ion mass m. Using the quadratic potential Φ_l given by equations (2.2) and (5.3), the potential energy is given by

$$< E_{pot,x} >= e \cdot k_x \cdot \Delta x^2. \tag{7.19}$$

Here, the longitudinal potential coefficient $k_x = 0.231\,75\,\mathrm{V\,mm^{-2}}$ obtained in chapter 5.1 was used. The thermal turn-around time Δt_{therm} is linked though Eq. (2.41) to the axial momentum spread of the ions stored inside the RFQ. Inserting equations (7.17)-(7.19) into (2.41) yields

$$\Delta t_{therm} = \frac{\Delta p_x}{e \cdot E_x} = \frac{\sqrt{2mk_x}}{e^{3/2} \cdot E_x^2} \cdot \Delta E. \tag{7.20}$$

Neglecting the contribution of the aberrations Δt_{abb}, the peak in Eq. (7.16) reduces to

$$\Delta t = \frac{\sqrt{2mk_x}}{e^{3/2} \cdot E_x^2} \cdot \Delta E \tag{7.21}$$

$$:= c_E \cdot \Delta E. \tag{7.22}$$

In Fig. 7.3b, the measured time-of-flight width in the focus is plotted with respect to the measured energy spread and fitted with Eq. (7.22). The parameter

$$c_E = \frac{\sqrt{2mk_x}}{e^{3/2} \cdot E_x^2} \tag{7.23}$$

was measured to be $c_E = 4.16(3)\,\mathrm{ns\,eV^{-1}}$, the error stated here is only based the statistical uncertainty of the fit. Taking into account, that the switching of the electrodes from trapping mode to ejection mode takes a finite time and that the initial ion distribution is modified by space charge effects, as was shown by this analysis, this is in reasonable agreement with the calculated value of $c_E = 4.7\,\mathrm{ns\,eV^{-1}}$.
No heating of the ions was observed in a similar scan measurement series for ^{85}Rb with a beamgate of 80 µs for RF amplitudes in a range from 0.15 V to 0.35 V. It can be concluded, that big numbers of stored $^{133}Cs^+$ ions prevent an efficient cooling of the $^{39}K^+$ ions. Possible reasons are space charge effects leading to an increase of the size of the ion cloud. Another explication is the so called RF heating [21]. Collisions with a heavier ion can lead to a phase jump of the ion motion with respect to the RF field, which increases the energy (compare Fig. 2.4b).

7.2 Stability of MR-ToF mass measurements

In order to realize MR-ToF on-line mass measurements mainly based on off-line references (see chapter 2.3.2), it is necessary to estimate and improve the accessible precision and accuracy. Several measurements of the well known masses of stable ions from the alkali off-line ion source

where performed with different settings. In the following, they are denoted as "cross-checks". Such a measurement consists of a cycle of three time-of-flight measurements: Two reference ions with mass taken from the AME 2016 [75] and one ion-of-interest in between. The time-of-flight is assumed to follow Eq. (2.51) and is deduced with a Gaussian maximum likelihood fit to the time-of-flight spectrum. This shape reflects the distribution of the thermal turn-around time Δt_{therm} and random aberrations. One source of systematic peak distortion is discussed in chapter 5. The measured mass m is then compared to the AME 2016 value. Because all reference ions from the alkali source are stable, their masses are known with high precision.
Several cross-check runs were performed for different settings. The isotopes ^{85}Rb and ^{133}Cs were used as reference to measure the mass of ^{87}Rb. The results of a set of these measurements is presented in the following. The settings and measured results for these runs are summarized in table 7.1. The given mean μ is the weighted mean of the single measurements, for the computation of the error, the Birge ratio [76] was included. It was examined, how strong the measured masses scatter and if the result is biased with respect to the AME 2016 value [75]. For all cross-checks, the RF is switched off 8 µs before the extraction, to reduce the time-of-flight dependence on the RF phase (see chapter 5.2).

Table 7.1: Setting and results of the MR-ToF MS cross-checks

run	low pass filter	RF phase scanned	scanned RF periods	revolutions	cycles	$\mu - AME$ (keV)	Birge ratio	σ (keV)
2017-1	no	no	–	500-1000	60	2.7±14.4	6.17	110.4
2017-3	no	yes	5	500-1000	177	-1.9±9.3	4.83	123.3
2018-1+2+3	yes	yes	5	500-1000	893	-7.0±3.9	5.58	117.5
2018-6	yes	yes	1	800	296	-17.3± 3.7	1.30	62.7
2018-7	yes	yes	15	800	97	-10.4±9.5	7.68	93.3
2018-8	yes	yes	5	800	297	-10.0±5.3	4.62	91.1
2018-ScRun-1	yes	yes	5	1000	260	-14.35±5.6	4.72	90.1

Run 2017-1

For run 2017-1, the buncher cooling time and consequently the RF phase at the moment of extraction was fixed and the number of revolution inside the MR-ToF MS varied from 500 to 1000. The results are depicted in Fig. 7.4. The measured mass of ^{87}Rb scatters with a standard deviation of $\sigma = 110.4$ keV around the mean, which is in perfect agreement with the AME value. The error bars of single points come from the statistical uncertainty of Gaussian fits to the measured time-of-flight spectra for the two reference ions and the ion of interest. The Birge ratio of 6.17 indicates that the scattering is dominated by a systematic error. With increasing revolution number, the resolution power increases and therefore the error bars shrink, but the scattering remains the same. A similar scattering was observed at RIKEN and recently reported by Schury[77].

7.2.1 Run 2017-3

In this run, the cooling time in the buncher was scanned over five RF periods in steps of 25 ns. The goal of this is to average out any remaining time-of-flight dependence on the RF phase. In Fig. 7.5, the measured time-of-flight is compared to the mean time-of-flight of all measurements with the same ion specie and revolution number in the MR-ToF MS. It can be seen, that for

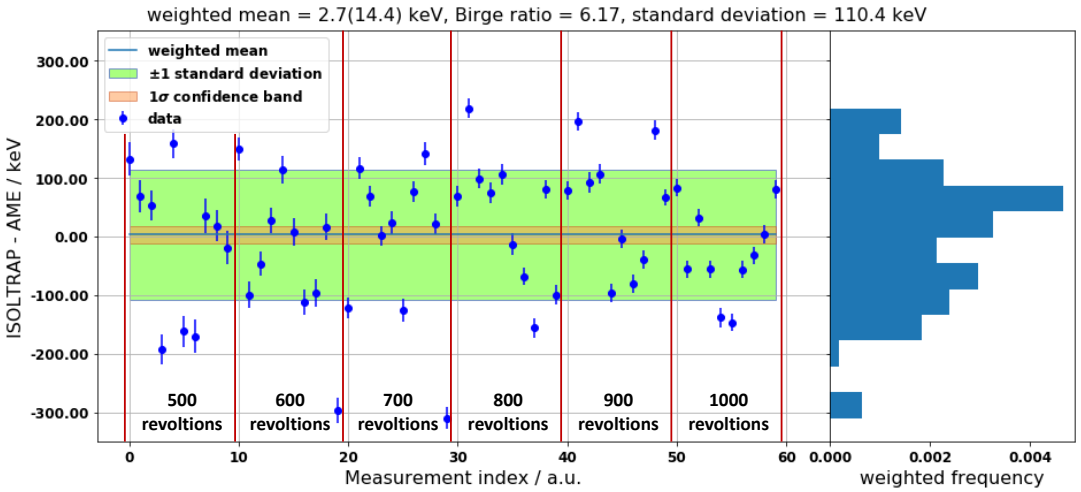

Figure 7.4: Measurement of the mass of ^{87}Rb with ^{85}Rb and ^{133}Cs as reference in run 2017-1. The histogram is the projection of the measured masses weighted by their statistical weight.

three measurements, the time-of-flight is affected by a relative shift on the order of $1 \cdot 10^{-5}$. This is about ten times more than the fluctuations for other points. They have in common, that the corresponding measurement files contain significantly less detected ions. These measurements were removed from the sample of measured mass values of ^{87}Rb depicted in Fig. 7.6. The same scattering around the AME value as in run 2017-1 was observed.

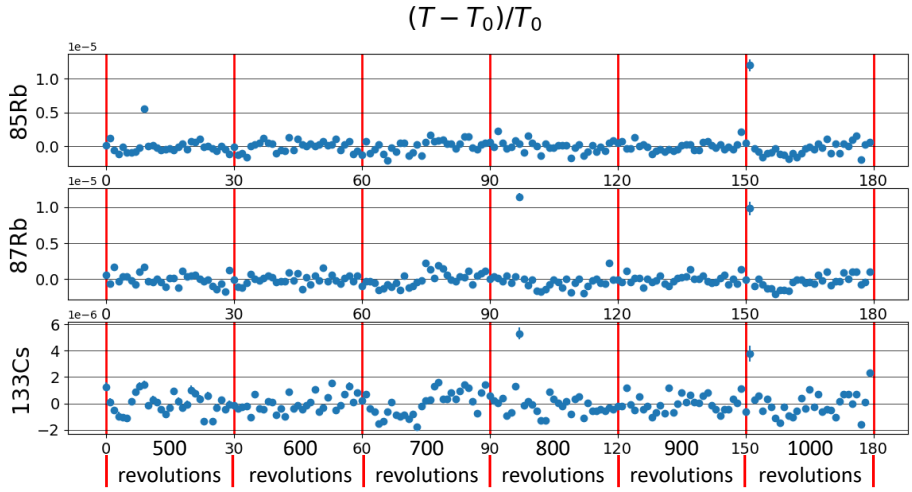

Figure 7.5: Relative deviation of the time-of-flight in a single measurement T from the mean time-of-flight of ions with the same number of revolutions T_0 in run 2017-3. The x labels give a list index for the ^{85}Rb-^{87}Rb-^{133}Cs cycle of a single mass measurement. The error bars are on the order of 10^{-7}.

7.2.2 Run 2018-1+2+3

The scattering of the time-of-flight and consequently the measured mass of ^{87}Rb around the AME value with a standard deviation much bigger than the statistical error from a single measurement indicated that there must be a systematic, but statistically scattering error source.

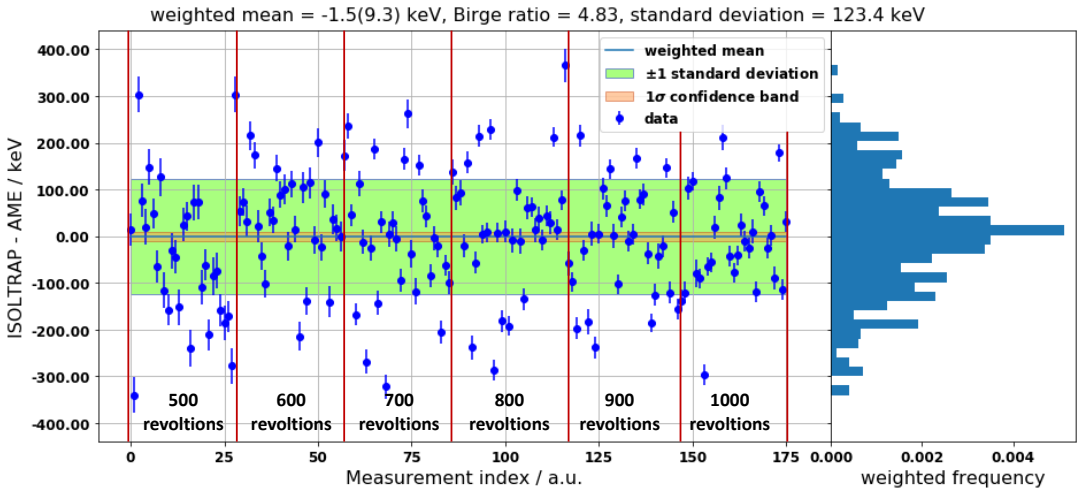

Figure 7.6: Measured ^{87}Rb mass values with the references ^{87}Rb and ^{133}Cs in run 2017-3.

The scattering must happen on the scale of minutes to affect entire files, but then changes for the next measured isotope. Therefore, thermal drifts could be excluded. As documented in [40], the time-of-flight strongly depends on the voltage applied to mirror 5 (see Fig. 4.4), which is the mirror electrode closest to the turning point of ions trapped inside the MR-ToF MS [41]. The power supply currently in use has a ripple given in the manual of less than 10 mV for frequencies lower than 10 Hz. For the voltage applied to mirror 5 of 2310.5 V, this corresponds to a relative stability of $\Delta V/V \approx \cdot 10^{-6}$. The relative change in time-of-flight $\delta t/t$ due to voltage changes at mirror 5 is given by $(\delta t/t)/(\Delta V/V_{M5}) = 0.5$ [41] and therefore on the order of $2 \cdot 10^{-6}$, which is in good agreement with the small time-of-flight fluctuations observed in run 2017-3 (see Fig. 7.5. Therefore, a low-pass filter with a resistance of $R = 1\,\mathrm{M\Omega}$ and a capacitance of $C_{filter} = 40\,\mu\mathrm{F}$ was installed between mirror 5 and its power supply to filter out high frequency fluctuations. The cut-off frequency is given by

$$f_c = \frac{1}{2\pi R \cdot C_{filter}} \approx 4\,\mathrm{mHz} \tag{7.24}$$

and the filter can be charged with the time constant

$$\tau = RC_{tot} = R \cdot (C_{filter} + C_{mirror}) \approx R \cdot C_{filter} = 40\,\mathrm{s}. \tag{7.25}$$

With this filter, three runs were performed with the same settings as in run 2017-3. The summed data is depicted in Fig. 7.7. No significant improvement was achieved. The measured mass still scatters around the mean with a standard deviation of $\sigma = 117.5\,\mathrm{keV}$, but this time, the mean is $1.8\,\sigma_\mu$ below the AME mass value.

7.2.3 Run 2018-6

To measure, if the scattering depends on the length of the measurement, run 2018-6 was performed with an RF phase scanned over only one RF period. This allows to measure an entire ^{85}Rb-^{87}Rb-^{133}Cs within one minute with the consequence of less statistic in each file and a therefore bigger statistical uncertainty. The results are shown in Fig. 7.8. Indeed the standard deviation was reduced to $\sigma = 62.7\,\mathrm{keV}$. The Birge ratio of 1.3 indicates, that the measured

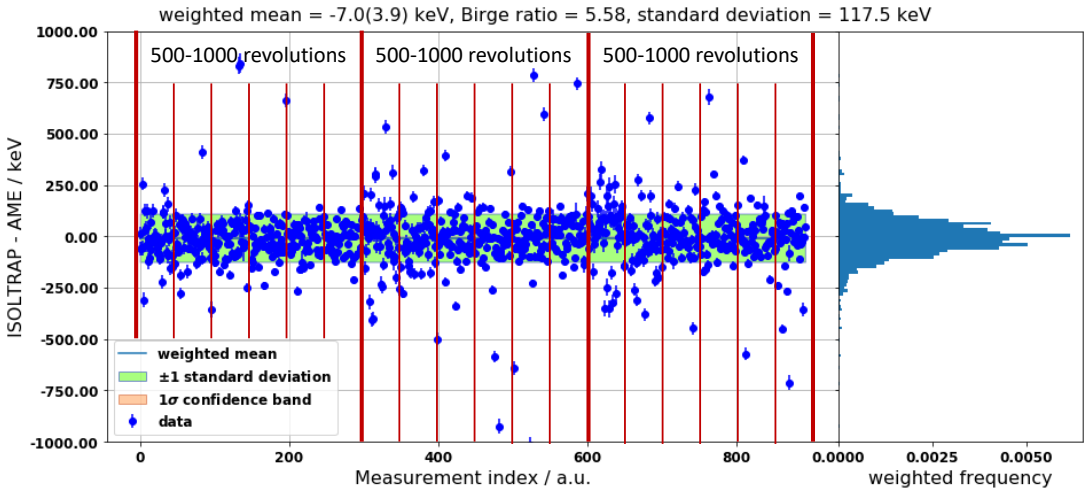

Figure 7.7: Measured mass of ^{85}Rb in the runs 2018-1+2+3 and weighted and normalized histogram. At each thin red line, the number of revolutions increases by 100.

values scatter randomly around the mean value of 17.3(3.7) keV below the AME value. This significant systematic shift has to be considered as an additional systematic error and gives therefore a lower limit to the achievable precision.

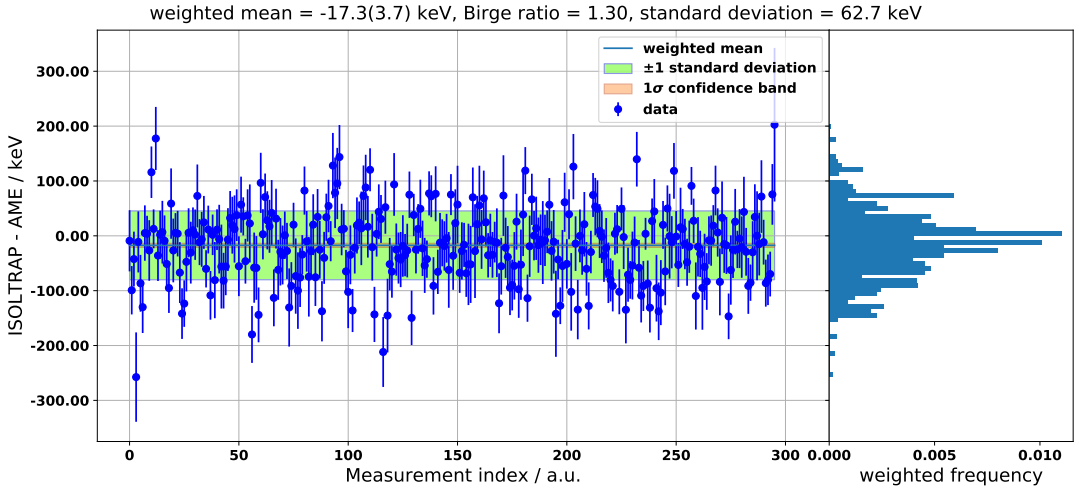

Figure 7.8: Measured mass values of ^{87}Rb in run 2018-6 in a scan over 1 RF periods and weighted and normalized histogram of the mass values.

7.2.4 Run 2018-7

Run 2018-6 was repeated, but this time with the buncher cooling time scanned over 15 RF periods, so that there is 15 times more statistic in each data file. The results are shown in Fig. 7.9. As expected, the error bars are much smaller than in run 2018-6 (see Fig. 7.8). On the other hand, the standard deviation of the scattering around the mean increased to 93.3 keV, the mean is 10.4(95) keV below the AME value. The Birge ratio of 7.86 indicates, that the longer measurement time compared to run 2018-6 did not increase in precision of single measurement points.

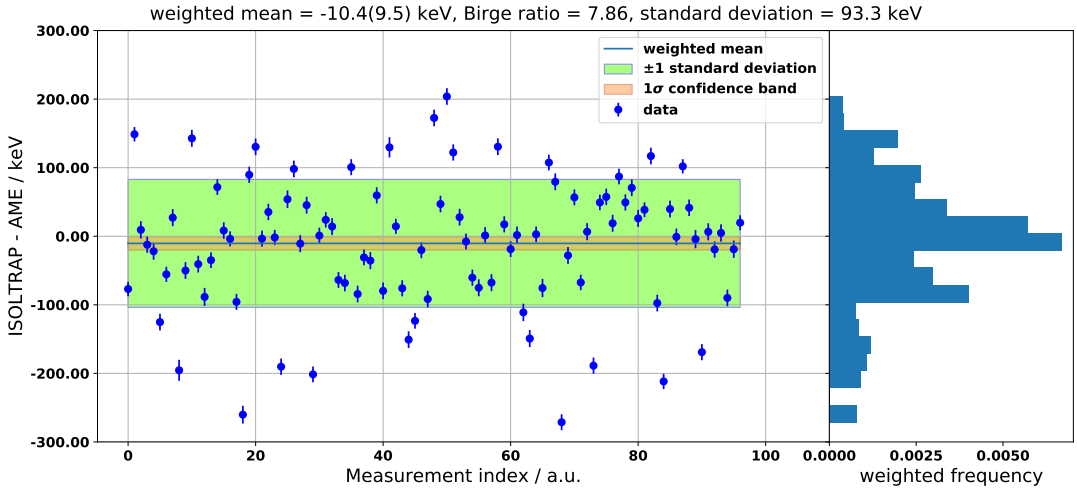

Figure 7.9: Measured mass values of ^{87}Rb in run 2018-7 in a scan over 15 RF periods with weighted and normalized histogram of the mass values.

7.2.5 Run 2018-8

This run was performed like the runs 2018-6 and 2018-7, but with the buncher cooling time scanned over five RF periods. The results are shown in Fig. 7.10. As in the runs before, the

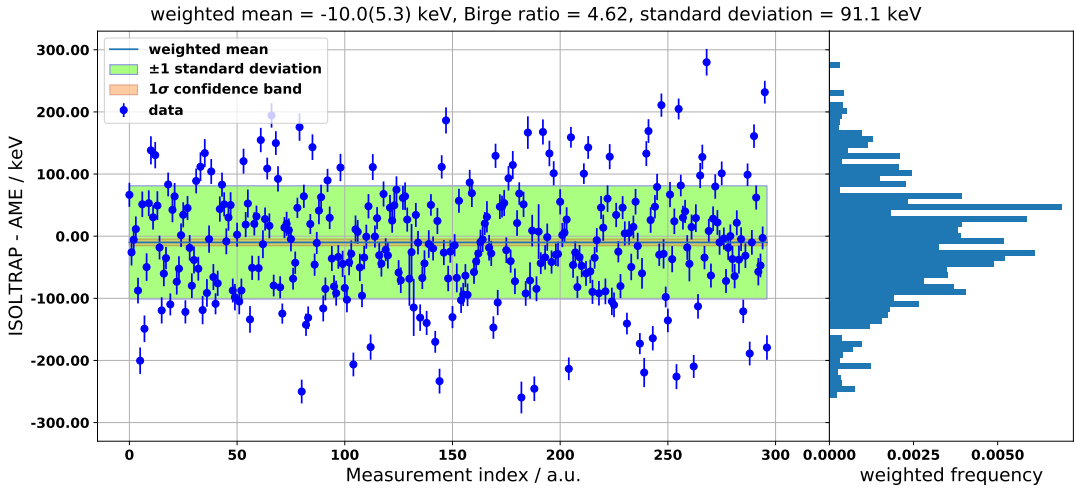

Figure 7.10: Measured mass values of ^{87}Rb in run 2018-8 in a scan over 5 RF periods with weighted and normalized histogram of the mass values.

measured ^{87}Rb mass scatters around a mean, which is $-10.0(53)$ keV below the AME value. The standard deviation of $\sigma = 91.1$ keV is approximately the same as in run 2018-7.

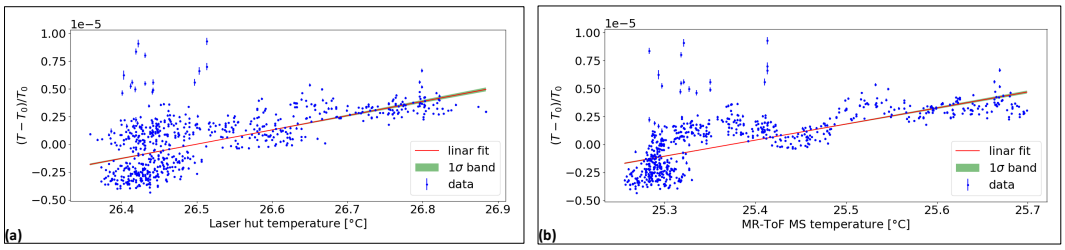

Figure 7.11: Relative deviation of the time-of-flight T from the mean time-of-flight of the same ion species T_0 (a) depending on the air temperature in the room housing the horizontal section and (b) depending on the temperature of the MR-ToF MS.

7.2.6 2018-ScRun-1

This run was performed in preparation of a measurement campaign to measure the mass of neutron rich scandium isotopes. For this run, the masses of the isotopes ^{39}K and ^{87}Rb were used as reference to measure the mass of ^{85}Rb. At the same time, the temperature was recorded with a sensor directly mounted on the metal pipe housing the MR-ToF MS and with another one in the room around the horizontal section of the ISOLTRAP experiment, here denoted as "Laser hut". In Fig. 7.11a, the relative deviation of the time-of-flight of a measurement from the mean of all measurements with the same ion species is plotted versus the temperature of the "Laser hut", where also the power supplies of the MR-ToF MS mirrors are located, which have a temperature dependent output voltage. In Fig. 7.11b, the same time-of-flight values are plotted versus the temperature measured on the metal pipe housing the MR-ToF MS. Clearly, the time-of-flight correlates positively with both temperatures. To both scatter plots, a linear function was fitted, returning the temperature coefficients

$$\frac{\partial t}{t \cdot \partial T_{Laser\ hut}} = 1.22(6) \times 10^{-5}\,\mathrm{K}^{-1} \tag{7.26}$$

with the temperature in the laser hut and

$$\frac{\partial t}{t \cdot \partial T_{MR-ToF\ MS}} = 1.39(5) \times 10^{-5}\,\mathrm{K}^{-1} \tag{7.27}$$

with the temperature of the MR-ToF MS. As the linear fits do not describe the curves well, the coefficients are only a rough guess. The temperature dependence of the time-of-flight can be explained with temperature dependent output voltages of the power supplies as well as with a thermal expansion of the MR-ToF MS as it was down in [78] for another MR-ToF MS setup at RIKEN. Since the temperature of the power supplies as well as the one of the MR-ToF MS changed at the same time, it was not possible to identify the two contributions individually. Also, it was not the temperature of the power supplies themselves, that was measured, but the temperature of the air in the room.

7.2.7 Conclusions

The time-of-flight of ions in the MR-ToF MS is affected by changes with a typical time-scale of about one minute. The source of this changes is a statistical process, which is demonstrated by the Gaussian spread of the measured mass values around a common mean. The distance

between the measured mean and the AME mass value is of the order of 10 keV, which therefore is a lower limit for the error of a MR-ToF mass measurement using off-line references. In addition to this, the standard deviation of the spread gives rise to a systematic error, which decreases with the number of measurements, but not with the measurement time per file, as was demonstrated by the runs 2018-6+7+8, where run 2018-6 had by far the smallest spread (see table 7.1). For this run, also the distribution of the measured masses corresponded to a random distribution around a mean within the statistical errors. This yields, that the source of the spread can be circumvented by measuring with a cycle of one minute or less. The number of revolutions inside the MR-ToF MS and consequently the over all time-of-flight has an impact on the statistical error of a single mass measurement cycle, but does not affect the overall spread of the measured values and therefore not the precision, as was shown with the runs 2017-1+2+3. The studies performed here show that in case of an on-line mass measurement based on off-line references, mass values based on files containing the data recorded over a span of a few minutes, an additional systematic error on the order of 100 keV has to be added to the final result since not all time-of-flight oscillations are covered. This error can be estimated using ff-line cross-checks during the beam-time preparation period. In addition, the temperature based fluctuations will soon be tackled by a temperature-controlled rack for the sensitive power supplies.

8 An improved quadrupole bender for the distribution of ions purified in the MR-TOF MS

A quadrupole bender (QPB) is an instrument used to change the direction of an ion beam by 90°, while allowing still, if needed, to send the beam on a straight path. In this chapter, the working principle, the design of a new QPB at ISOLTRAP, simulations of its ion-optical properties and its commissioning are described in this chapter.
The working principle is illustrated with a cross section through the QPB newly installed at ISOLTRAP in Fig. 8.1. The ion beam enters from the left. With positive potential on the three electrode rods marked with a "+", the beam can be bent by 90°. When all electrodes are grounded, the ions can simply fly straight to the opposite output. The new quadrupole bender replaces an old one which used to be placed inside a 6-way-cross between the MR-ToF MS and the 90-degree-bender (for the position see Fig. 4.2). It makes it possible, to guide ions extracted from the MR-ToF MS to a new electron multiplier with a high time resolution installed in the LIS section. With the old quadrupole bender, distorted peak shapes were observed, that were probably caused by fringe fields. Therefore, a new quadrupole bender with a shielding casing was manufactured at the University of Greifswald. A picture of the assembled new quadrupole bender is shown in Fig. 8.2. The old bender consisted of only four rods. The new one has two major improvements:

1. a casing shields the electric field created by the rods.

2. each entry is equipped with an Einzel lens consisting of a ground plate, a floated plate and the casing of the bender.

The new bender is mounted with four rods on a rotatable CF160 flange, containing nine electrical feedthroughs: Four for the rods, four for the Einzel lenses and one spare.
The new QPB was assembled and installed at the ISOLTRAP set-up inside a new 6-way-cross. The mounting flange is fixed on the top opening of the cross, to allow easy access during the alignment of the rotatable flange.

8.1 Simulation of the quadrupole bender

Based on already existing drawings, the new quadrupole bender and the so-called LIS section (from a Laser Ion Source formerly installed there), was integrated into the SIMION geometry file already used for simulations of the new guiding lens (see chapter 6) and the time-of-flight towards the electron multiplier EMP2h (see chapter 5). Voltages on the ion optical elements were first adapted by hand and then further improved using a simplex. A screenshot of such a simulation is displayed in Fig. 8.3. The voltages were optimized for the transmission to the electronmultiplier EMPnew. After applying the voltages at the real set-up, ions could immediately be transmitted to this detector. Several voltages were scanned to further improve

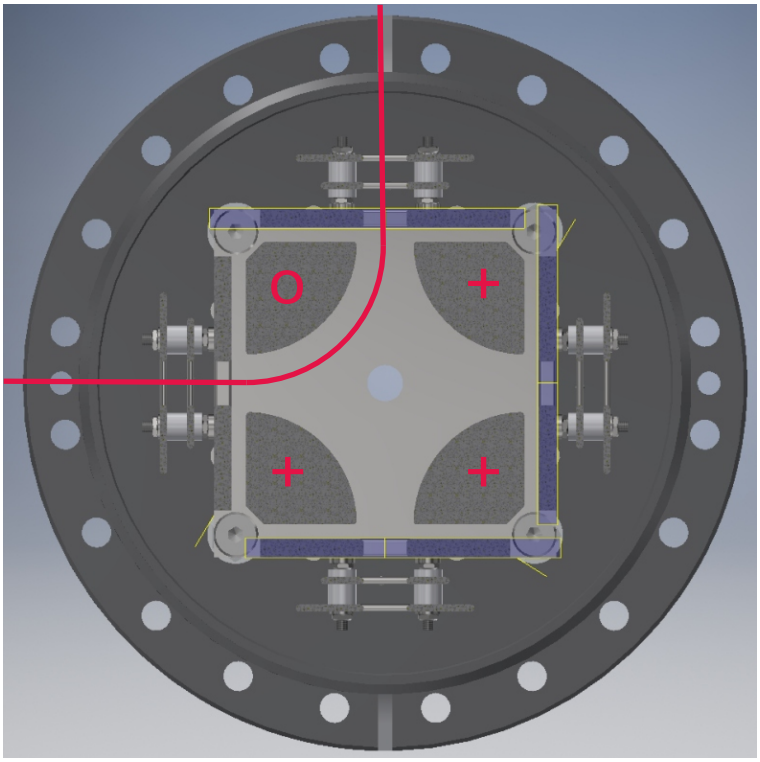

Figure 8.1: Cross section of the new quadrupole bender. Ions follow the red line, when three rods (marked with a + sign) are on an appropriate positive potential and another one (marked with a 0) is on ground or less positive potential.

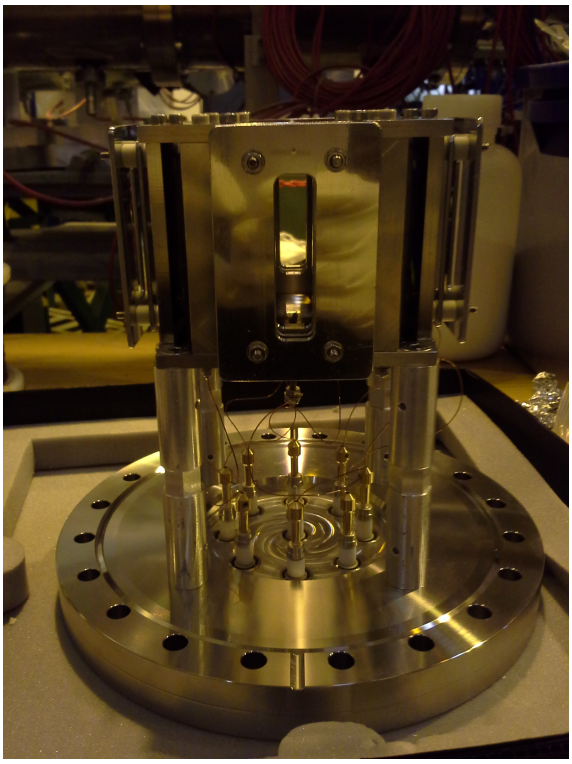

Figure 8.2: Assembled new quadrupole bender. For details see text.

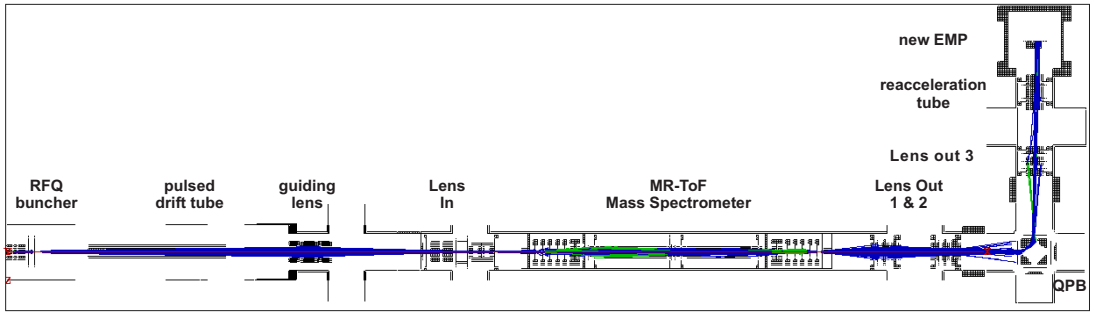

Figure 8.3: Simulated ion trajectories from the last segments of the RFQ to the new EMP with two revolutions inside the MR-ToF MS (Top view). Blue trajectories go to the right, green trajectories go to the left. The new quadrupole bender (QPB) is in the corner on the bottom left.

the transmission. The best values from the simulation and from the optimization on the set-up are compared in table 8.1.

Table 8.1: Voltages of ion-optical elements taken from simulations and optimized at the set-up. All voltages are given in volts.

electrode	simulation	experiment	comment to the transmission dependence
"Lens out 1"	-4988	-2500	started at value from campaign before
"Lens out 2"	-2375	-4200	started at value from campaign before
"QPB lens MR-TOF side"	-5659	-3250	flat between −2500 V and −5000 V
"QPB lens LIS side"	-889	0	flat between 0 V and 1000 V
"QPB rod 1"	834	834	flat
"QPB rod 2"	3404	3550	broad peak
"QPB rod 3"	3558	3140	flat
"QPB rod 4"	3070	3130	flat between 3000 V and 3270 V
"Lens out 2"	1500	750	flat
"reacceleration tube"	1500	1400	flat

For the voltages of the lenses "Lens out 1" and "Lens out 2" the start values of the optimization on the set-up were the voltages used for measurements with the electron multiplier EMP2h directly behind the MR-ToF MS in the beamtime before (see Fig. 4.2). Therefore they deviate strongly from the optimal settings found with the simulation. The voltages of the four quadrupole rods did not change a lot and the transmission showed no strong dependences. Also the lenses behind the bender, "Lens out 3" and the "reacceleration tube" barely had any impact implying that the beam is already well focussed when leaving the QPB. The two lenses of the QPB on the MR-TOF side and on the LIS side (towards the new EMP) also had no big impact. This means, that the beam is already well focussed before the QPB and does not diverge strongly. The measured count rate with the new EMP for ^{133}Cs with a beam gate of 3 µs was about 4.1 s^{-1} compared to 7.1 s^{-1} on the EMP2h just before the QPB implying a transmission of 58 % through the bender. Further optimization would probably increase the transmission.

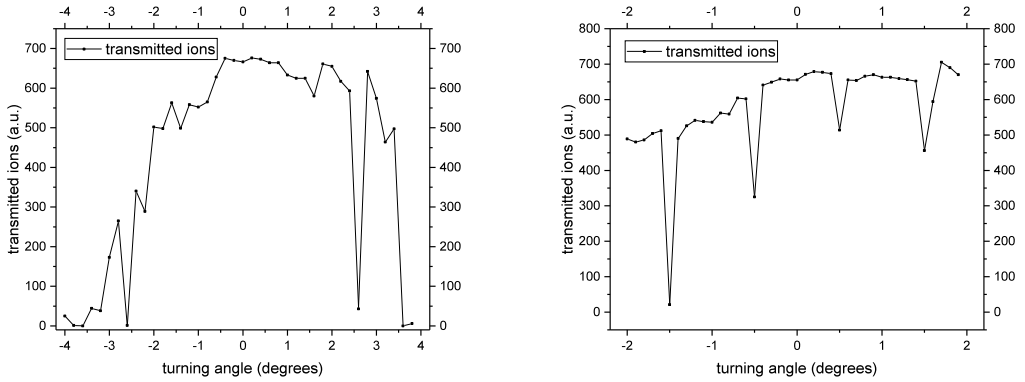

(a) To the new EMP

(b) To MCP2v

Figure 8.4: Simulated transmission (a) to the new electron multiplier and (b) to MCP2v detector (see Fig. 4.2) and the Penning traps in arbitrary units depending on a rotation of the quadrupole bender around its vertical symmetry axis.

8.2 Estimated tolerance for the misalignment of the quadrupole bender

Since the mounting flange is rotatable, the QPB was aligned by hand and the tolerances for a possible misalignment were studied with simulations, such for the linear transmission to the MCP detector just below the Preparation Penning Trap, called (MCP2v), such to the new electron multiplier. This was done by simulating the transmission to both detectors with the quadrupole bender being turned around its rotation axis in different angles using the optimized electrode voltages from the simulation with perfect alignment. The simulation shows no significant loss for a turning angle of less than 0.4° and a loss of about 20 % of the ions to an angle of 1.4 % for the transport to the new EMP (see Fig. 8.4a) and even less sensitivity to MCP2v (see Fi. 8.4b). For single turning angles, a much lower transmission than for neighbouring data points was obtained. If there are indeed resonances, that are sensitive to small deviations in the geometry, they can probably be compensated by an adoption of the ion-optical settings.

During the installation, the distances between the edges of the outer lens plates and the flanges imply a turning angle of less or equal 0.3°, which is well inside the simulated tolerances.

8.3 New support for quadrupole lenses 1 and 2

The exchange of the old cross made another modification necessary: The mount for the quadrupole lenses 1 and 2 of the 90-degree-bender towards the vertical section of the ISOLTRAP set-up (see Fig. 4.2) was welded into the old 6-way-cross. Consequently, a new mount had to be manufactured. The old mount was also difficult to access, i. e. the quadrupole bender had to be removed first. Therefore, the new mount should be on the other end inside the cube of the 90°-bender. A bar with treads was already available to fix the mount. The mount has to fulfil the following requirements:

1. it has to fix the quadrupole lenses in the right position.

2. adjustments in both dimensions transversal to the beam should be possible.

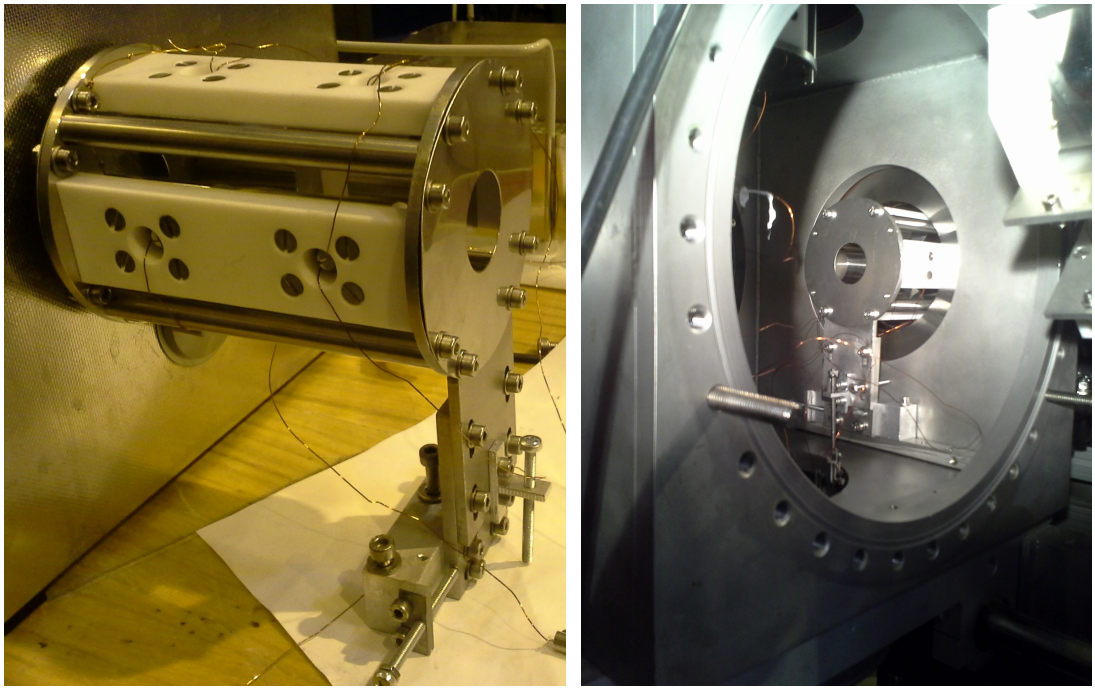

(a) (b)

Figure 8.5: Quadrupole lenses 1 and 2 of the 90°-bender (a) with its new support and (b) built-in. The picture is taken looking through the opening for the removable flange of the cube containing the 90°-bender in inverse beam direction.

3. it should fit into the limited space.

4. it should be cheap and easy to machine.

A picture of the quadrupole lenses with their new support is shown in Fig. 8.5a and how it is built-in in Fig. 8.5b. The mount consists of five main parts:

1. the foot: An aluminium block which is screwed to the existing threaded bar.

2. the plate: It is a plate of stainless steal. It is screwed to the foot using four long holes allowing horizontal alignment.

3. the holder: Due to space requirements, this piece made of stainless steel replaces an existing ring, on which the quadrupole electrodes and alignment rods were mounted. Therefore, it contains a circular section with 20 holes, 8 threaded ones to mount the collimator plate, 4 for the alignment rods and 8 for the isolator plates holding the quadrupole electrodes. It is connected to a rectangular section containing four long-holes. With these, it is mounted to the plate, allowing vertical alignment.

4. the horizontal alignment plate: It is a small plate of stainless steel fixed on the side of the foot. On it, a long screw is fixed, that can be used to push the plate precisely into the correct horizontal position.

5. the vertical alignment T: It is an aluminium T piece fixed on the plate. It fulfils the same task as the horizontal alignment plate, except for that it allows for pushing the holder in the correct vertical position with a long scew to the bottom plate of the cube.

All parts were produced by the CERN workshop, except for the drilling of holes in the aluminium pieces and cutting threads, what we performed ourself in the ISOLDE workshop. For the plate and the holder, water jet cutting was used.

9 Conclusions and outlook

In this thesis, work was carried out at two precision experiments and described in detail herein. For the ALPHATRAP experiment, a system for contact free transmission of microwaves from the room temperature environment first to the 77 K heat shield and in a second step to the cryogenic trap tower using microwave horns was designed. COMSOL simulations predicted an adequate transmission with resonances sufficiently broader than a typical Larmor resonance. The three custom made horns are currently in use for the first g-factor measurement for electrons bound to boron-like $^{40}Ar^{13+}$ ions. Further ground-breaking experiments with lithium-like and hydrogen-like for $Z > 20$ will follow. For these measurements, the mode cleaner to filter out unwanted modes and the laser injection for the alignment of laser beams with the microwaves are ready to be installed.

At the ISOLTRAP experiment, precision, efficiency and stability in MR-ToF mass measurements were investigated. In chapter 5, first the generation of a realistic set of ions as a starting point for simulations was described. With it, theoretical expectation as well as experimental observations could be reproduced. Then, it was pointed out, that a dependence of time-of-flight and count rate on the phase of the buncher RF at the moment of extraction can shift and distort the observed time-of-flight peaks measured with the MR-ToF MS. It was demonstrated experimentally how this RF phase dependence can be reduced for the count rate and eliminated for the time-of-flight. This leads to more symmetric peak shapes, that make it easier to identify the mean time-of-flight of an ion species and consequently allows more precise mass measurements. The quantitative behaviour depends on many parameters, especially on the tune of the RF coupling boxes, and the measured peak shape on the detector also depends on the performance of the ion optics. Therefore, quantitative results presented in this thesis will be difficult to confirm. Nevertheless, a setting independent optimization protocol for the preparation of the buncher for measurements could be given. Simulations could reproduce the RF phase dependence at least qualitatively. The count rate dependence on the RF amplitude and delay was understood theoretically and is in good agreement with simulations. This suggests, that the assumed initial conditions are reasonable and can be used as a starting point for further simulations downstream the RFQ, as they were done in the chapters 6 and 8. Further simulations also modelling collisions with the buffer gas might be a further step towards a better understanding of the ion beam ejected from the buncher. In order to increase the transport efficiency and stability, an ion-optical Einzel lens was designed. It is now ready to be installed and tested. Simulations of a quadrupole bender were successfully performed as a starting point for optimization at the set-up. It was validated, that the installation was done in the given tolerances. In the future, the new quadrupole bender will make it possible to switch faster and without mechanical intervention between MR-ToF and Penning-trap measurements. Doing so, the MR-ToF MS can be used more efficiently as a tool to monitor the composition of the ion beam delivered to the Penning traps. With the MR-ToF MS, a new approach to measure the energy spread of an incoming ion beam was presented. Taking into account simplifying assumptions, the results were compatible with estimations using the thermal turn-around time

of the ions in the buncher. Then, the stability of measurement relying on off-line references only was investigated. It was shown, that the time-of-flight varies on the order of 10^{-6} on a minute time-scale. The measured masses fluctuate around the AME value, with a standard deviation of 100 keV for ^{87}Rb with the off-line references ^{85}Rb and ^{133}Cs. By reducing the time needed for a complete ^{85}Rb-^{87}Rb-^{133}Cs cycle to about one minute, the standard deviation of this scattering could be reduced to about 60 keV which then was equal to the statistical error of a single measurement. In an on-line mass measurement using off-line references only, the standard deviation of the spread is an additional systematic error which has to be added to the statistical error coming from the fit of a single measurement point. During the beamtime preparation the error can be estimated with cross-check runs as the ones described in this thesis. Systematic shifts on the order of 10 keV were observed, giving a lower limit for the achievable precision. This result is a step towards measurements with exotic ions, for which no isobaric reference is available and towards new measurement schemes using further beam cleaning to avoid space charge effects in the MR-ToF MS. It is also interesting for other experiments in the fast growing field of MR-ToF mass spectrometry as it gives an estimate of the achievable precision in this kind of measurement. The modified timing patter and the new quadrupole bender were already used, the new guiding lens will follow soon. Upcoming experiments with neutron-deficient argon and neutron-rich krypton will profit from these improvements.

Danksagung

Mein herzlicher Dank gilt:

- Prof. Klaus Blaum für die vielfältige Unterstützung, die mir diese Arbeit an zwei Standorten erst ermöglicht hat.
- Vladimir Manea für die intensive Betreuung an ISOLTRAP. Deine Kenntnis über die vielen Tipps und Tricks haben mir vielfach die Messdaten gerettet.
- Sven Sturm für Betreuung an ALPHATRAP. In diesen drei Monaten habe ich unheimlich viel gelernt.
- Dem weiteren ISOLTRAP Team, namentlich Jonas, Maxime, Dinko und Frank für die tatkräftige Unterstützung, aber auch dafür, dem großen CERN eine familiäre Atmosphäre zu geben.
- Bei meinen Eltern, die mir das Studium erst ermöglicht haben.
- Bei Inga für die große moralische Unterstützung über die Distanz und die regelmäßigen Besuche.

10 Bibliography

[1] Wikipedia contributors. *Standard Model — Wikipedia, The Free Encyclopedia.* Apr. 3, 2017.

[2] E. Epelbaum, H.-W. Hammer, and Ulf-G. Meißner. „Modern theory of nuclear forces". In: *Rev. Mod. Phys.* 81 (4 Dec. 2009), pp. 1773–1825.

[3] Jens Dilling et al. „Penning-Trap Mass Measurements in Atomic and Nuclear Physics". In: *Annual Review of Nuclear and Particle Science* 68.1 (2018), null.

[4] Thomas Beier et al. „g_j factor of an electron bound in a hydrogenlike ion". In: *Phys. Rev. A* 62 (3 Aug. 2000), p. 032510.

[5] Florian Köhler et al. „Isotope dependence of the Zeeman effect in lithium-like calcium". In: *Nature communications* 7 (2016), p. 10246.

[6] S Sturm et al. „On g -factor experiments with individual ions". In: *Journal of Physics B: Atomic, Molecular and Optical Physics* 43.7 (2010), p. 074016.

[7] M. Rosenbusch et al. „Probing the $N = 32$ Shell Closure below the Magic Proton Number $Z = 20$: Mass Measurements of the Exotic Isotopes ^{52,53}K". In: *Phys. Rev. Lett.* 114 (20 May 2015), p. 202501.

[8] F Wienholtz et al. „Masses of exotic calcium isotopes pin down nuclear forces". In: *Nature* 498.7454 (2013), p. 346.

[9] R. N. Wolf et al. „Plumbing Neutron Stars to New Depths with the Binding Energy of the Exotic Nuclide ^{82}Zn". In: *Phys. Rev. Lett.* 110 (4 Jan. 2013), p. 041101.

[10] Z. Meisel et al. „Time-of-flight mass measurements of neutron-rich chromium isotopes up to $N = 40$ and implications for the accreted neutron star crust". In: *Phys. Rev. C* 93 (3 Mar. 2016), p. 035805.

[11] A. Kellerbauer et al. „Direct Mass Measurements on the Superallowed Emitter ^{74}Rb and Its Daughter ^{74}Kr: Isospin-Symmetry-Breaking Correction for Standard-Model Tests". In: *Phys. Rev. Lett.* 93 (7 Aug. 2004), p. 072502.

[12] Klaus Blaum. „High-accuracy mass spectrometry with stored ions". In: *Physics Reports* 425.1 (2006), pp. 1–78.

[13] A. Ostendorf et al. *Preparation and Storage of Ultracold Complex Molecules. The linear Paul trap.* Universität Düsseldorf. URL: `http://www.exphy.uni-duesseldorf.de/ResearchInst/ultracold_complex_molecules.htm` (visited on 06/11/2018).

[14] R. F. Wuerker, H. Shelton, and R. V. Langmuir. „Electrodynamic Containment of Charged Particles". In: *Journal of Applied Physics* 30.3 (1959), pp. 342–349.

[15] M. Drewsen and A. Brøner. „Harmonic linear Paul trap: Stability diagram and effective potentials". In: *Phys. Rev. A* 62 (4 Sept. 2000), p. 045401.

[16] Wolfgang Paul. „Electromagnetic traps for charged and neutral particles“. In: *Rev. Mod. Phys.* 62 (3 July 1990), pp. 531–540.

[17] Lawrence Ruby. „Applications of the Mathieu equation“. In: *American Journal of Physics* 64.1 (1996), pp. 39–44.

[18] Donald J Douglas, Aaron J Frank, and Dunmin Mao. „Linear ion traps in mass spectrometry.“ In: *Mass spectrometry reviews* 24 1 (2005), pp. 1–29.

[19] Glomin Thomas Abraham and Anindya Chatterjee. „Approximate Asymptotics for a Nonlinear Mathieu Equation Using Harmonic Balance Based Averaging“. In: *Nonlinear Dynamics* 31.4 (Mar. 2003), pp. 347–365.

[20] R.E. March and R.J. Hughes. *Quadrupole Storage Mass Spectrometry*. Chemical Analysis: A Series of Monographs on Analytical Chemistry and Its Applications. John Wiley & Sons, 1989.

[21] F Herfurth et al. „A linear radiofrequency ion trap for accumulation, bunching, and emittance improvement of radioactive ion beams“. In: *Nuclear Instruments and Methods in Physics Research Section A: Accelerators, Spectrometers, Detectors and Associated Equipment* 469.2 (2001), pp. 254–275.

[22] Stefan Schwarz. „Manipulation radioaktiver Ionenstrahlenmit Hilfe einer Paulfalle und direkte Massenmessungen an neutronenarmen Quecksilberisotopen mit dem ISOLTRAP-Experiment“. Mainz, Diss., 1998. Dr. Mainz, 1999, 131 S.

[23] Max Planck Institute for Nuclear Physics. *THe TRAP Project. Physical basics*. Mar. 26, 2014. URL: `https://www.mpi-hd.mpg.de/blaum/high-precision-ms/ptms/basics.en.html` (visited on 05/25/2018).

[24] Adam West. „Lepton Dipole Moments“. In: *arXiv preprint arXiv:1607.00925* (2016).

[25] Lowell S. Brown and Gerald Gabrielse. „Geonium theory: Physics of a single electron or ion in a Penning trap“. In: *Rev. Mod. Phys.* 58 (1 Jan. 1986), pp. 233–311.

[26] G. Gabrielse. „Why Is Sideband Mass Spectrometry Possible with Ions in a Penning Trap?“ In: *Phys. Rev. Lett.* 102 (17 Apr. 2009), p. 172501.

[27] Martin Kretzschmar. „The Ramsey method in high-precision mass spectrometry with Penning traps: Theoretical foundations“. In: *International Journal of Mass Spectrometry* 264.2 (2007), pp. 122–145.

[28] Comisarow Melvin B. and Marshall Alan G. „The Early Development of Fourier Transform Ion Cyclotron Resonance (FT-ICR) Spectroscopy“. In: *Journal of Mass Spectrometry* 31.6 (), pp. 581–585.

[29] F Köhler et al. „The electron mass from g -factor measurements on hydrogen-like carbon 12 C 5+“. In: *Journal of Physics B: Atomic, Molecular and Optical Physics* 48.14 (2015), p. 144032.

[30] G. Gräff, H. Kalinowsky, and J. Traut. „A direct determination of the proton electron mass ratio“. In: *Zeitschrift für Physik A Atoms and Nuclei* 297.1 (Mar. 1980), pp. 35–39.

[31] D Lunney and (on behalf of the ISOLTRAP Collaboration). „Extending and refining the nuclear mass surface with ISOLTRAP“. In: *Journal of Physics G: Nuclear and Particle Physics* 44.6 (2017), p. 064008.

[32] K. Eliseev S.and Blaum et al. „A phase-imaging technique for cyclotron-frequency measurements“. In: *Applied Physics B* 114.1 (Jan. 2014), pp. 107–128.

[33] M. Block. „Recent developments in Penning-trap mass spectrometry“. In: *Nuclear Instruments and Methods in Physics Research Section B: Beam Interactions with Materials and Atoms* 376 (2016). Proceedings of the XVIIth International Conference on Electromagnetic Isotope Separators and Related Topics (EMIS2015), Grand Rapids, MI, U.S.A., 11-15 May 2015, pp. 265–269.

[34] Michael Edward Peskin and Daniel V. Schroeder. *An introduction to quantum field theory.* eng. [Nachdr.] The advanced book program. Boulder, Colo. [u.a.]: Westview Pr., 2006, XXII, 842 S.

[35] N. Hermanspahn et al. „Observation of the Continuous Stern-Gerlach Effect on an Electron Bound in an Atomic Ion“. In: *Phys. Rev. Lett.* 84 (3 Jan. 2000), pp. 427–430.

[36] H. Dehmelt. „New continuous Stern-Gerlach effect and a hint of “the” elementary particle“. In: *Zeitschrift für Physik D Atoms, Molecules and Clusters* 10.2 (June 1988), pp. 127–134.

[37] Jonas Karthein. „Precision mass measurements using the Phase-Imaging Ion-Cyclotron-Resonance detection technique“. PhD thesis. Ruprecht-Karls-Universität Heidelberg, 2017.

[38] F. Wienholtz et al. „Mass-selective ion ejection from multi-reflection time-of-flight devices via a pulsed in-trap lift“. In: *International Journal of Mass Spectrometry* 421 (2017), pp. 285–293.

[39] A. N. Verentchikov et al. „Multireflection planar time-of-flight mass analyzer. I: An analyzer for a parallel tandem spectrometer“. In: *Technical Physics* 50.1 (Jan. 2005), pp. 73–81.

[40] Robert N. Wolf et al. „Static-mirror ion capture and time focusing for electrostatic ion-beam traps and multi-reflection time-of-flight mass analyzers by use of an in-trap potential lift“. In: *International Journal of Mass Spectrometry* 313 (2012), pp. 8–14.

[41] R.N. Wolf et al. „On-line separation of short-lived nuclei by a multi-reflection time-of-flight device“. In: *Nuclear Instruments and Methods in Physics Research Section A: Accelerators, Spectrometers, Detectors and Associated Equipment* 686 (2012), pp. 82–90.

[42] Masud Chaichian et al. *Electrodynamics. An Intensive Course.* eng. SpringerLink : Bücher. Berlin, Heidelberg: Springer, 2016. Chap. Propagation of Electromagnetic Waves in Waveguides, pp. 226–239.

[43] Takahiro Ito et al. „Flexible terahertz fiber optics with low bend-induced losses“. In: *J. Opt. Soc. Am. B* 24.5 (May 2007), pp. 1230–1235.

[44] J R Crespo López-Urrutia et al. „Progress at the Heidelberg EBIT“. In: *Journal of Physics: Conference Series* 2.1 (2004), p. 42.

[45] S. Kraemer. „Towards Laser Cooling of Beryllium Ions at the Alphatrap Experiment“. Master Thesis. Ruprecht-Karls-Universität, Heidelberg, 2017.

[46] B. D'Urso, B. Odom, and G. Gabrielse. „Feedback Cooling of a One-Electron Oscillator“. In: *Phys. Rev. Lett.* 90 (4 Jan. 2003), p. 043001.

[47] Tim Sailer. „A Laser Ion Source for the Alphatrap Experiment“. PhD thesis. Ruprecht-Karls-Universität Heidelberg, 2017.

[48] *S10MS Datasheet: Rev. D. S10MS Series WR10 Frequency Extension Modules 75 to 110 GHz*. Aug. 2016. URL: https://www.omlinc.com/images/pdf/SxxMS/OML-S10MS_Datasheet.pdf (visited on 05/16/2018).

[49] *RF Module User's Guide*. Version 5.2. COMSOL, Inc.

[50] H. Häffner et al. „High-Accuracy Measurement of the Magnetic Moment Anomaly of the Electron Bound in Hydrogenlike Carbon". In: *Phys. Rev. Lett.* 85 (25 Dec. 2000), pp. 5308–5311.

[51] Mahmoud Moghavvemi, Hossein Ameri Mahabadi, and Farhang Alijani. *Multi-Hole Waveguide Directional Couplers*. Nov. 2012.

[52] A A Shchepetnov et al. „Nuclear recoil correction to the g factor of boron-like argon". In: *Journal of Physics: Conference Series* 583.1 (2015), p. 012001.

[53] MI-WAVE Millimeter Wave Products Inc. *Product Catalog 2017*. 2017. Chap. 261 Series-Standard Gain Horns, p. 17.

[54] Erich Kugler. „The ISOLDE facility". In: *Hyperfine Interactions* 129.1 (Dec. 2000), pp. 23–42.

[55] MJ Garcia Borge. „Highlights of the ISOLDE facility and the HIE-ISOLDE project". In: *Nuclear Instruments and Methods in Physics Research Section B: Beam Interactions with Materials and Atoms* 376 (2016), pp. 408–412.

[56] R Catherall et al. „The ISOLDE facility". In: *Journal of Physics G: Nuclear and Particle Physics* 44.9 (2017), p. 094002.

[57] V.N. Fedosseev et al. „ISOLDE RILIS: New beams, new facilities". In: *Nuclear Instruments and Methods in Physics Research Section B: Beam Interactions with Materials and Atoms* 266.19 (2008). Proceedings of the XVth International Conference on Electromagnetic Isotope Separators and Techniques Related to their Applications, pp. 4378–4382.

[58] V.I. Mishin et al. „Chemically selective laser ion-source for the CERN-ISOLDE on-line mass separator facility". In: *Nuclear Instruments and Methods in Physics Research Section B: Beam Interactions with Materials and Atoms* 73.4 (1993), pp. 550–560.

[59] R.N. Wolf et al. „ISOLTRAP's multi-reflection time-of-flight mass separator/spectrometer". In: *International Journal of Mass Spectrometry* 349-350 (2013). 100 years of Mass Spectrometry, pp. 123–133.

[60] M. Mougeot et al. „Precision Mass Measurements of $^{58--63}$Cr: Nuclear Collectivity Towards the $N = 40$ Island of Inversion". In: *Phys. Rev. Lett.* 120 (23 June 2018), p. 232501.

[61] K. Blaum et al. „Carbon clusters for absolute mass measurements at ISOLTRAP". In: *The European Physical Journal A - Hadrons and Nuclei* 15.1 (Sept. 2002), pp. 245–248.

[62] H. Raimbault-Hartmann et al. „A cylindrical Penning trap for capture, mass selective cooling, and bunching of radioactive ion beams". In: *Nuclear Instruments and Methods in Physics Research Section B: Beam Interactions with Materials and Atoms* 126.1 (1997). International Conference on Electromagnetic Isotope Separators and Techniques Related to Their Applications, pp. 378–382.

[63] M. Rosenbusch et al. „Ion bunch stacking in a Penning trap after purification in an electrostatic mirror trap". In: *Applied Physics B* 114.1 (Jan. 2014), pp. 147–155.

[64] E. Leistenschneider et al. „Dawning of the $N = 32$ Shell Closure Seen through Precision Mass Measurements of Neutron-Rich Titanium Isotopes“. In: *Phys. Rev. Lett.* 120 (6 Feb. 2018), p. 062503.

[65] Rene Brun and Fons Rademakers. „ROOT — An object oriented data analysis framework“. In: *Nuclear Instruments and Methods in Physics Research Section A: Accelerators, Spectrometers, Detectors and Associated Equipment* 389.1 (1997). New Computing Techniques in Physics Research V, pp. 81–86.

[66] David A Dahl. „simion for the personal computer in reflection“. In: *International Journal of Mass Spectrometry* 200.1 (2000). Volume 200: The state of the field as we move into a new millenium, pp. 3–25.

[67] T. Dickel et al. „A high-performance multiple-reflection time-of-flight mass spectrometer and isobar separator for the research with exotic nuclei“. In: *Nuclear Instruments and Methods in Physics Research Section A: Accelerators, Spectrometers, Detectors and Associated Equipment* 777 (2015), pp. 172–188.

[68] Autodesk. *Autodesk Inventor*. Version 2017. San Rafeal, CA, 2017.

[69] P. Schury et al. „Multi-reflection time-of-flight mass spectrograph for short-lived radioactive ions“. In: *The European Physical Journal A* 42.3 (Oct. 2009), p. 343.

[70] P. Schury et al. „A high-resolution multi-reflection time-of-flight mass spectrograph for precision mass measurements at RIKEN/SLOWRI“. In: *Nuclear Instruments and Methods in Physics Research Section B: Beam Interactions with Materials and Atoms* 335 (2014), pp. 39–53.

[71] Christian Jesch et al. „The MR-TOF-MS isobar separator for the TITAN facility at TRIUMF“. In: *Hyperfine Interactions* 235.1 (Nov. 2015), pp. 97–106.

[72] Tsviki Y. Hirsh et al. „First operation and mass separation with the CARIBU MR-TOF“. In: *Nuclear Instruments and Methods in Physics Research Section B: Beam Interactions with Materials and Atoms* 376 (2016). Proceedings of the XVIIth International Conference on Electromagnetic Isotope Separators and Related Topics (EMIS2015), Grand Rapids, MI, U.S.A., 11-15 May 2015, pp. 229–232.

[73] J.S. Winfield et al. „A versatile high-resolution magnetic spectrometer for energy compression, reaction studies and nuclear spectroscopy“. In: *Nuclear Instruments and Methods in Physics Research Section A: Accelerators, Spectrometers, Detectors and Associated Equipment* 704 (2013), pp. 76–83.

[74] P. Chauveau et al. „PILGRIM, a Multi-Reflection Time-of-Flight Mass Spectrometer for Spiral2-S3 at GANIL“. In: *Nuclear Instruments and Methods in Physics Research Section B: Beam Interactions with Materials and Atoms* 376 (2016). Proceedings of the XVIIth International Conference on Electromagnetic Isotope Separators and Related Topics (EMIS2015), Grand Rapids, MI, U.S.A., 11-15 May 2015, pp. 211–215.

[75] W.J. Huang et al. „The AME2016 atomic mass evaluation (I). Evaluation of input data; and adjustment procedures“. In: *Chinese Physics C* 41.3 (2017), p. 030002.

[76] Raymond T. Birge. „The Calculation of Errors by the Method of Least Squares“. In: *Phys. Rev.* 40 (2 Apr. 1932), pp. 207–227.

[77] P. Schury et al. „Improving wide-band mass measurements in a multi-reflection time-of-flight mass spectrograph by usage of a concomitant measurement scheme“. In: (2018).

[78] P. Schury et al. „A multi-reflection time-of-flight mass spectrograph for short-lived and super-heavy nuclei“. In: *Nuclear Instruments and Methods in Physics Research Section B: Beam Interactions with Materials and Atoms* 317 (2013). XVIth International Conference on ElectroMagnetic Isotope Separators and Techniques Related to their Applications, December 2–7, 2012 at Matsue, Japan, pp. 537–543.

Erklärung:

Ich versichere, dass ich diese Arbeit selbstständig verfasst habe und keine anderen als die angegebenen Quellen und Hilfsmittel benutzt habe.

Heidelberg, den 18.06.2018 .....